Imagerie de population et IRM de diffusion pour caractériser la sclérose en plaques pour la moélle épinière humaine

Haykel Snoussi

UNIVERSITE BRETAGNE LOIRE / MATHSTIC

UNIVERSITÉ DE RENNES 1

THESE DE DOCTORAT DE

L'UNIVERSITE DE RENNES 1
COMUE UNIVERSITE BRETAGNE LOIRE

ECOLE DOCTORALE N° 601
Mathématiques et Sciences et Technologies de l'Information et de la Communication
Spécialité : Signal, Image, Vision

Par
Haykel Snoussi

Population imaging and diffusion MRI for characterizing multiple sclerosis in the human spinal cord

Thèse présentée et soutenue à Rennes, le 02 Mai 2019
Unité de recherche : Empenn U1228, INRIA/INSERM, IRISA, UMR CNRS 6074
Thèse N° :

Rapporteurs avant soutenance :

Virginie Callot Directrice de recherche, CNRS, Marseille, France
Isabelle Berry Professeure, Université Toulouse III, Toulouse, France

Composition du Jury :

Examinateurs	: Giulio Gambarota	Professeur, Université Rennes 1, France
	Virginie Callot	Directrice de recherche, CNRS, Marseille, France
	Isabelle Berry	Professeure, Université Toulouse III, France
	Julien Cohen-Adad	Associate Professor, Polytechnique Montreal, Quebec, Canada
Dir. de thèse	: Christian Barillot	Directeur de recherche, CNRS, Rennes, France
Co-dir. de thèse	: Gilles Edan	PU-PH, Neurologue, CHU Pontchaillou, Rennes, France

Invité
Co-encadrant de thèse : Emmanuel Caruyer Chargé de recherche, CNRS, Rennes, France

Acknowledgments

Al-hamdouli'Allah, I praise my God, the almighty for providing me this opportunity. This PhD thesis appears in its current form due to the assistance and guidance of many talented scientists and several people. So, it is with great humility and gratitude that I acknowledge all of them and give particular mention here. I would especially like to thank and say *chokran jazilan*:

Emmanuel Caruyer, my supervisor. Thank you for giving me the opportunity to be your first PhD student and for your trust and excellent guidance from start to finish. I am also very grateful for your continuous support, for valuable guidance, your experience sharing, your sympathy and your enthusiasm. I greatly appreciate your behavior during my PhD thesis which makes me feel that you are my elder brother. I am thankful to you for your patient and endless efforts in carving out a semblance of a researcher in me. Thank you Emmanuel from the bottom of my heart !

Christian Barillot, my co-supervisor and the team leader. Thank you for giving me the opportunity to pursue a PhD degree at Empenn research unit. A very big thank you also for your sharing experience, for various meeting about my advancement during my work, your many fresh perspectives, your comprehension and motivation at difficult moments. Your help and contribution to this PhD thesis are paramount. I will always be thankful for your encouragement and support for doing the research trip to Polytechnique Montréal, Canada. Other important thing, your calm and balanced leadership skills have always inspired me and they will be very useful for my future career. My deepest thanks for you Christian !

I would also like to thank all my colleagues from the *Empenn* research unit for providing a nice working climate and for their scientific input. I would especially like to mention Benoit combes, Olivier Commowick and René-paul Debroize, who I disturb repeatedly with technical and scientific questions. They were always ready to help me instantly, regardless of the topic. This dissertation would not have been possible without the MRI data sets that were kindly provided to me by Elise Bannier, Anne Kerbrat and Giles Edan from the hospital of Rennes, France. A big thank you for them. I would also like to mention Antoine Legouhy and Xavier Rolland, with whom I shared my actual office. I would like to thank them for daily discussions, several questions and their effort to guarantee calm working environment. I have to thank very much: Pierre, Isabelle, Camille with her attractive smile, Cédric, Maia, Sudhanya, Florent, Raphaël Truffet, Raphaël Chouteau, Inés, Francesca, Mostafa, Corentin, Mathis, Pierre-Yves, Claire, Quentin, Giulia, Michael, Julien, Yao, Julie, Sylvain, Laureline, Arnaud, Patrique and all members of Empenn research unit. Three other people, Armelle Mozziconacci, Sophie Viaud and Angelique Jarnoux, who have constantly facilitate the complex administrative part of the PhD, have also my gratitude. I would like to also acknowledge my institute Inria Rennes - Bretagne Atlantique, France, for hosting me in an environment with excellent work facilities and a charming campus. My PhD work was partially funded by EMISEP PHRC, and by the Britanny region.

I want also to thank Julien Cohen-Adad for numerous discussions and scientific guidance. I

will always appreciate the significant experiences from the research trip at his Neuropoly team in Polytechnique Montréal as a part of my PhD work. During this trip, I was lucky to have the help in *Spinal cord Toolbox* of Benjamin De Leener and Charley Gros, I also enjoyed our discussions and coffee breaks with Harris Nami, Aldo Zaimi and Atef Badji. I would like to thank all members of NeuroPoly team.

I am grateful also for my personnel friends: Taher A.H, Med EH.A and Med Mk for their special and unforgettable support... I have also to thank A. ben Said, Y. Bettaieb, S. Souissi, M. Dhuib, A. Bayoudhi, M. Hedi Fourati, M. Ktata and M. ksentini for their phone calls and thinking on me. With no doubt, I thank M. I. Nass and L. Rahmani with which I enjoyed many lunch and dinner. A big thank you also for Mr Mohamed Adel Alimi, my professor in ENIS engineering school.

Last but very important, I would like to thank my family: my mother Sajiaa, my father Abdelhamid, my brother Haithem, his wife Hela, my sister Haifa and her husband Ibrahim. Thank you for your unfailing love, patience, and understanding. I owe an infinite debt to you.

I would finally like to express my sincere gratitude to my grandfather, late *Muhammad Pbuh.*, who has always been a great source of hope and inspiration for me. I will not forget his 'acceptation' of my visit to him in 13 August 2017 morning and how it was the reception ! It was unforgettable days and moments, it was as my 'wedding party' and more... I would like to dedicate the effort and the manuscript of my PhD thesis to him.

Haykel Snoussi,

Contents

Abstract

Multiple sclerosis is an inflammatory disorder of the central nervous system. Quantitative MRI has huge potential to provide intrinsic and normative value to tissue properties useful for diagnosis, prognosis and ultimately clinical trials of this disease. However, there is a large discrepancy between the clinical observations and how the pathology is exhibited on brain scans. Complementary to brain imaging, the study of MS lesions in the spinal cord has recently gained interest as a potential marker for the early physical impairment. Therefore, investigating how the spinal cord is damaged using quantitative imaging, and in particular diffusion MRI, becomes an acute challenge. Acquiring and processing Diffusion MRI in spinal cord present inherent challenges. Local differences in magnetic susceptibility between soft tissues, air and bone make the magnetic field within the spinal cord non-uniform and inhomogeneous. Also, given the small cross-sectional area of the spinal cord and the lack of visible anatomical landmarks (similar to cortical sulci and gyri in the brain) to help identification of tracts or spinal cord levels, the characterization of MRI metrics is difficult.

In our work, we propose several contributions for the processing and statistical analysis of diffusion MRI data acquired in the spinal cord. First, we do a comparative study of distortion correction methods for the spine. Second, using a cohort of MS patients and healthy controls, we study the link between diffusion measures and the presence or absence in a given vertebral level of lesion, and we show that we can predict the latter with good accuracy with a multivariate linear learning on the diffusion measures. Last, we show the feasibility of performing longitudinal study of the evolution of diffusion MRI metrics by performing a reproducibility study using a test-retest dataset, and apply it to the 2 first timepoints (M0 and M12) of our cohort of patients.

Evaluation of distortion correction methods Various procedures were proposed for correcting susceptibility distortion in brain data. We focus on the comparative evaluation of these distortion correction methods for spine imaging using reversed gradient polarity technique on spinal cord. We propose a novel geometric metrics to measure the alignment of the reconstructed diffusion model with the apparent centerline of the spine. In the spinal cord white matter, the local displacement of water molecules is mainly aligned with longitudinal fibers, which themselves follow a path parallel to the centerline of the spinal cord. Therefore, we can expect that the principal eigenvector of the diffusion tensor is locally aligned tangentially with the centerline of the spine. However, the susceptibility distortion affects the apparent shape of the spine without altering the direction of the tensor. This results in a poorer alignment of the diffusion tensor with the spine, locally. We describe a method to measure how the diffusion tensors and the centerline of spinal cord align with each other.

Prediction of lesion using diffusion measures Once diffusion MRI data is preprocessed, we calculate several diffusion-based metrics depending on the reconstruction method and then extract average values of these metrics for each vertebral level using an atlas-based approach. From this data, we study the possibility to predict the presence of multiple sclerosis abnormalities. Diffusion MRI is sensitive to demyelination and structural changes and provides potentially non-invasive biomarkers of pathology and lesions in white matter. Statistical analyses were performed to test the sensitivity of computed metrics to pathology in multiple sclerosis.

Longitudinal evolution of diffusion measures Last, we investigate how diffusion MRI metrics vary in the different cervical regions with the progression of the disease. We first study the reproducibility of diffusion MRI on healthy volunteers with a test-retest procedure using both standard diffusion tensor imaging (DTI) and multi-compartment Ball-and-Stick models. Based on the test re-test quantitative calibration, we provide quantitative figures of pathology evolution between M0 and M12 in the cervical spine, exhibiting how the pathology damage spans in the cervical spinal cord.

Chapter 1

Introduction

Contents

1.1 General context

Magnetic resonance imaging (MRI) is a non-invasive medical imaging technology used for creating multi-dimensional anatomical and physiological images of the body. MRI offers a powerful and sensitive technique for characterizing Multiple sclerosis (MS) disease and often provides an important para-clinical tool for lesion detection, diagnosis and treatment monitoring. MS is an inflammatory disorder of the central nervous system. Quantitative MRI has huge potential to provide intrinsic and normative value to tissue properties useful for diagnosis, prognosis and ultimately clinical trials of this disease.

1.2 EMISEP project

EMISEP, *Early Spinal Cord Lesions and Late Disability in Relapsing Remitting Multiple Sclerosis Patients*, is a project promoted by the Rennes University Hospital and founded by the French Ministry of Health (*Programme hospitalier de recherche clinique – PHRC*). EMISEP project is investigated principally by the Professor Gilles Edan, PU-PH, Neurologue, CHU Pontchaillou, Rennes, France. The project is also associated by several investigators: CHU of Bordeaux, Dijon, Lyon, Marseille, Nancy, Paris, Reims, Strasbourg, Toulouse, as part of the *Observatoire Français de la Sclérose En Plaques* (OFSEP). The context of this project is the MS disease which is the most frequent acquired neurological disease affecting young adults, around 1/1000 people in France, and leading to impairment. EMISEP focuses on physical impairment and especially on the ability to walk. Early and well adapted treatment is essential in patients presenting aggressive forms of MS.

Some studies demonstrated that several factors were likely to announce aggressive development of the disease, such as age, number of focal lesions on baseline MRI, and clinical activity. However, these factors explain partially the physical impairment progression which prevents their use at the individual level. Spinal cord is often affected in MS. Yet, early radiological depiction of spinal cord lesions is not always correlated with clinical symptoms. The investigation of a preliminary cervical spinal cord data of reduced number of patients, diffusion MRI or magnetization transfer, have shown that diffuse spinal cord injury would be correlated with physical impairment as evaluated by the EDSS score. Besides, the role of early spinal cord affection (first two years) in the evolution of physical impairment remains unknown. The spinal cord is a clinically common and eloquent site frequently involved in MS (Wheeler-Kingshott et al., 2014). The EMISEP project proposes to address these different issues and perform a longitudinal study on Relapsing-remitting MS (RRMS) patients, recruited in the first year of the disease. The realization of this project is facilitated by the OFSEP cohort study started in 2011.

The main objective of EMISEP project is to evaluate the potential of focal and diffuse lesions observed using MRI early in the disease course to predict the physical impairment at 5 years in RRMS patients. Then as secondary objectives, doing the previous objective on diffuse lesions only in several centers and comparing focal and diffuse lesions.

1.3 Diffusion MRI of the spine: challenges and application to patients follow-up in MS

In the context of EMISEP project, the main objective of this PhD thesis is to focus on the diffusion MRI part of EMISEP. Despite advancement is being made, only few research laboratory in the World are actively studying and investigating human spinal cord imaging (Stroman et al.,

2014). This can be explained by the specific anatomical arrangement of the spinal cord and the surrounding structures which limit its accessibility for research (Stroman et al., 2014).

First, acquiring diffusion MRI scan in spinal cord site is especially challenging due to the presence of various surrounding tissue types: bone, CSF, gray and white matter, muscle, fat and air. This non-uniform magnetic field environment causes loss of signal intensity and susceptibility distortion. Secondly, the elongated shape of the spinal cord anatomy requires a large field of view (FOV) in the superior-inferior direction and its small cross-sectional size requires high spatial resolution. The third challenge for spinal cord imaging arises from the physiological motion within the spinal canal (Stroman et al., 2014). Last, diffusion MRI models provide complex data related to the microstructure, which require adapted statistical analysis.

In our work, we propose several contributions for the processing and statistical analysis of diffusion MRI data acquired in the spinal cord. First, we do a comparative study of distortion correction methods for the spine. Second, using a cohort of MS patients and healthy controls, we study the link between diffusion measures and the presence or absence of lesion in a given vertebral level and we show that we can predict the latter with good accuracy with a multivariate linear learning on the diffusion measures. Last, we show the feasibility of performing longitudinal study of the evolution of diffusion MRI metrics by performing a reproducibility study using a test-retest dataset, and apply it to the 2 first timepoints (M0 and M12) of our cohort of patients.

1.4 Manuscript organization

In Chapter. 3, we start this manuscript by a state-of-the-art, we first describe MS disease followed by an overview of human spinal cord anatomy. Then, we introduce the MRI modality from the spin of hydrogen nuclei to signal recovery and diffusion image reconstruction. We also present the potential impact of MRI for diagnosis and treatment monitoring in MS as shown in several studies. Last, we introduce different models of water diffusion estimated from diffusion MRI sequence which will be useful for the remaining of the manuscript. In particular, we highlight the strengths and weaknesses of the models selected in the context of our work.

In Chapter. 4, we begin by presenting different methods which were proposed for correcting susceptibility-induced distortion in brain data. Few attempts and studies in neuroimaging applications have tailored and incorporated the use of these techniques in spinal cord imaging. We focus on the comparative evaluation of these distortion correction methods using reversed gradient polarity technique on spinal cord. We propose and describe novel geometric metrics to measure the alignment of the reconstructed diffusion model with the apparent centerline of the spine. We use these geometric metrics along with comparison with a reference anatomical scan to compare and evaluate the impact of distortion correction. All steps of work-flow of this study are explained with details then various tables show Tukey's test comparison are presented.

In Chapter. 5, we give a critical overview about existing approaches for quantifying diffusion metrics. Then we present available MRI data, number of healthy volunteers and MS patients, MRI protocols and quantitative data about MS lesions in these patients. We present the processing pipeline for computing maps of diffusion indices and extracting level- and subject-specific averages of these indices using atlas-based approach. Last, we show how this data can be used to predict the presence of multiple sclerosis abnormalities. The sensitivity and specificity of the proposed lesion detection are evaluated.

In Chapter. 6, we investigate how diffusion MRI metrics vary in the different cervical regions with the progression of the disease. We first study the reproducibility of diffusion MRI on healthy volunteers with a test-retest procedure using both standard diffusion tensor imaging (DTI) and multi-compartment Ball-and-Stick models. Based on the test re-test quantitative calibration, we

provide quantitative figures of pathology evolution between M0 and M12 in the cervical spine, exhibiting how the pathology damage spans in the cervical spinal cord. We relate these changes to clinical and radiological data of the same subjects.

In Chapter. 7, we give the general conclusion of this manuscript, and put the contributions of our work related to distortion correction and the characterization of MS abnormalities within cervical spinal cord. We also propose some perspectives.

Chapter 2

Résumé en Français

Contents

2.1 Contexte

2.1.1 Sclérose en plaques

L'imagerie par résonance magnétique (IRM) est une technologie d'imagerie médicale non invasive utilisée pour créer des images multidimensionnelles anatomiques et physiologiques du corps. L'IRM offre une technique puissante et sensible pour caractériser la maladie de sclérose en plaques (SEP) et constitue souvent un outil para-clinique important pour la détection, le diagnostic et le suivi du traitement des lésions. La SEP est une maladie démyélinisante et inflammatoire perturbant le flux d'informations au sein du système nerveux central (SNC) et entre le SNC et le corps (Hachinski et al., 2006). Le système immunitaire attaque et endommage par erreur la couche qui recouvre les nerfs, appelée gaine de myéline. Cela perturbe les messages voyageant le long des nerfs, provoquant divers symptômes. Figure.2.1 illustre un exemple de cellules nerveuses saines et touchées présentant le statut de gaine de myéline.

Les lésions spécifiques sont déterminées par l'emplacement des lésions dans le SNC et peuvent englober une altération de la sensation ou une perte de sensibilité, y compris une difficulté à marcher, de la fatigue, une sensation de fatigue, une douleur chronique, des problèmes émotionnels, une vision floue, des difficultés de pensée, entre autres (Compston and Coles, 2008).

L'IRM quantitative a un potentiel énorme pour conférer une valeur intrinsèque et normative aux propriétés des tissus utiles au diagnostic, au pronostic et finalement aux essais cliniques de

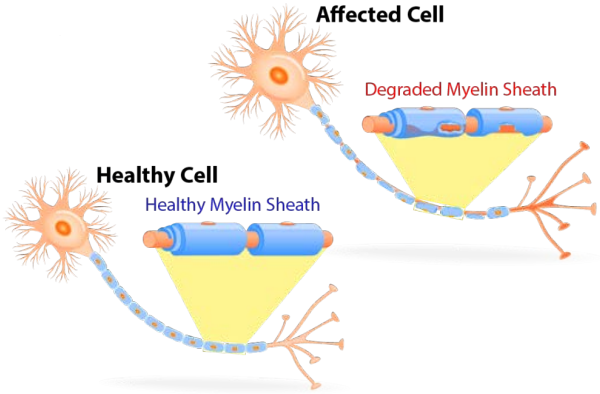

Figure 2.1: Exemples illustratifs de cellules nerveuses saines et affectées dans la SEP.

cette maladie. Cependant, il existe un écart important entre les observations cliniques et la manière dont la pathologie est présentée sur les scanners du cerveau.

Complémentaire à l'imagerie cérébrale, l'étude des lésions de SEP dans la moelle épinière a récemment suscité l'intérêt comme marqueur potentiel de la déficience physique précoce. Par conséquent, rechercher la façon dont la moelle épinière est endommagée à l'aide d'une imagerie quantitative, et en particulier d'une IRM par diffusion, devient un véritable défi. L'acquisition et le traitement de l'IRM par diffusion dans la moelle épinière présentent des défis inhérents. Les différences locales de susceptibilité magnétique entre les tissus mous, l'air et les os rendent le champ magnétique dans la moelle épinière non uniforme et inhomogène. De plus, étant donné la petite section transversale de la moelle épinière et l'absence de repères anatomiques visibles (similaires aux sulci corticaux et au gyri dans le cerveau) facilitant l'identification des voies ou des niveaux de la moelle épinière, il est difficile de caractériser les paramètres d'IRM.

2.1.2 Projet EMISEP

EMISEP est un projet promu par le CHU de Rennes et fondé par le ministère français de la Santé (PHRC). Le projet est également associé par plusieurs enquêteurs: CHU de Rennes, Bordeaux, Dijon, Lyon, Marseille, Nancy, Paris, Reims, Strasbourg, Toulouse, dans le cadre de l'Observatoire Français de la Clause (OFSEP). Le contexte de ce projet est la maladie SEP, qui est la maladie neurologique acquise la plus fréquente chez les jeunes adultes, environ 1/1 000 personnes en France, et conduisant à une déficience. EMISEP se concentre sur les déficiences physiques et en particulier sur la capacité de marcher. Un traitement précoce et bien adapté est essentiel chez les patients présentant des formes agressives de SEP. L'objectif principal du projet EMISEP est d'évaluer le potentiel des lésions focales et diffuses observées en utilisant l'IRM au début de l'évolution de la maladie pour prédire la déficience physique à 5 ans chez les patients atteints de SEP-RR. Puis comme objectifs secondaires, faire l'objectif précédent sur les lésions diffuses uniquement dans plusieurs centres et comparer les lésions focales et diffuses.

Dans le cadre du projet EMISEP, l'objectif principal de cette thèse de doctorat est de se concentrer sur la partie IRM de diffusion d'EMISEP. Malgré les progrès réalisés, seuls quelques laboratoires de recherche dans le monde étudient et étudient activement l'imagerie de la moelle épinière humaine (Stroman et al., 2014). Cela peut s'expliquer par la disposition anatomique spécifique de la moelle épinière et des structures environnantes, qui limite son accessibilité à la recherche (Stroman et al., 2014).

Premièrement, l'acquisition de l'IRM par diffusion dans le site de la moelle épinière est parti-

culièrement difficile en raison de la présence de différents types de tissus environnants: os, LCR, substance grise et blanche, muscle, graisse et air. Cet environnement de champ magnétique non uniforme provoque une perte d'intensité du signal et une distorsion de susceptibilité. Deuxièmement, la forme allongée de l'anatomie de la moelle épinière nécessite un grand champ de vision dans la direction supérieure-inférieure et sa petite taille en coupe transversale nécessite une résolution spatiale élevée. Le troisième défi pour l'imagerie de la moelle épinière provient du mouvement physiologique dans le canal rachidien (Stroman et al., 2014). Enfin, les modèles d'IRM par diffusion fournissent des données complexes relatives à la microstructure, qui nécessitent une analyse statistique adaptée.

2.2 Méthodes

Dans notre travail, nous proposons plusieurs contributions pour le traitement et l'analyse statistique des données de diffusion IRM acquises dans la moelle épinière. Premièrement, nous effectuons une étude comparative des méthodes de correction de distorsion pour la colonne vertébrale. Deuxièmement, en utilisant une cohorte de patients atteints de sclérose en plaques et de témoins sains, nous étudions le lien entre les mesures de diffusion et la présence ou l'absence d'un niveau de lésion vertébral donné, et nous montrons que nous pouvons prédire cette dernière avec une bonne précision avec un apprentissage linéaire multivarié sur les mesures de diffusion. Enfin, nous montrons la faisabilité d'une étude longitudinale de l'évolution des métriques IRM de diffusion en réalisant une étude de reproductibilité à l'aide d'un jeu de données test-retest, et l'appliquons aux 2 premiers moments (M0 et M12) de notre cohorte de patients.

2.2.1 Evaluation des méthodes de correction de la distorsion

Différentes procédures ont été proposées pour corriger la distorsion de la susceptibilité dans les données cérébrales. Nous nous concentrons sur l'évaluation comparative de ces méthodes de correction de distorsion pour l'imagerie de la colonne vertébrale en utilisant une technique de polarité à gradient inversé sur la moelle épinière. Nous proposons une nouvelle métrique géométrique pour mesurer l'alignement du modèle de diffusion reconstruit avec la ligne centrale apparente de la colonne vertébrale. Dans la substance blanche de la moelle épinière, le déplacement local des molécules d'eau est principalement aligné avec les fibres longitudinales, qui suivent elles-mêmes un chemin parallèle à la ligne médiane de la moelle épinière. Par conséquent, on peut s'attendre à ce que le vecteur propre principal du tenseur de diffusion soit localement aligné tangentiellement à l'axe de la colonne vertébrale. Cependant, la distorsion de susceptibilité affecte la forme apparente de la colonne vertébrale sans modifier la direction du tenseur. Cela se traduit par un alignement plus faible du tenseur de diffusion avec la colonne vertébrale, localement.

Nous nous concentrons sur l'évaluation comparative de 4 méthodes de correction de distorsion: Matching (BM) (Hedouin et al., 2017), correction d'artefact de sensibilité hyper-élastique (HySCO) (Ruthotto et al., 2012), TOPUP (Andersson et al., 2003) et Voss (Voss et al., 2006) . Dans cette section, nous donnons un aperçu de chacune de ces méthodes.

2.2.2 Prévision de lésion à l'aide de mesures de diffusion

Une fois les données d'IRM de diffusion pré-traitées, nous calculons plusieurs métriques basées sur la diffusion en fonction de la méthode de reconstruction, puis extrayons les valeurs moyennes de ces métriques pour chaque niveau vertébral en utilisant une approche basée sur un atlas. À partir de ces données, nous étudions la possibilité de prédire la présence d'anomalies de la sclérose

en plaques. L'IRM de diffusion est sensible à la démyélinisation et aux changements structurels et fournit des biomarqueurs potentiellement non invasifs de pathologies et de lésions de la substance blanche. Des analyses statistiques ont été effectuées pour tester la sensibilité des paramètres calculés à la pathologie de la sclérose en plaques.

2.2.3 Evolution longitudinale des mesures de diffusion

Enfin, nous étudions comment les métriques IRM de diffusion varient dans les différentes régions cervicales en fonction de l'évolution de la maladie. Nous étudions d'abord la reproductibilité de l'IRM par diffusion sur des volontaires sains à l'aide d'une procédure test-retest utilisant à la fois des méthodes classiques d'imagerie par tenseur par diffusion (DTI) et des modèles Ball-and-Stick à plusieurs compartiments. Sur la base du nouvel étalonnage quantitatif des tests, nous fournissons des chiffres quantitatifs de l'évolution de la pathologie entre M0 et M12 dans la colonne cervicale, montrant la portée des dommages causés par la pathologie dans la moelle épinière cervicale.

2.3 Conclusion

Nous avons proposé deux nouvelles métriques géométrie pour étudier et evaluer l'impact de la correction de distorsion dans l'IRM de diffusion de la moelle épinière. Partant de l'hypothèse que la distorsion n'affecte que la forme apparente de l'épine dorsale et non la direction du tenseur, nous avons proposé deux nouvelles statistiques qui tiennent en compte de l'alignement du tenseur de diffusion sur l'axe central apparent de la moelle épinière. Cette évaluation géométrique a été réalisée sur 95 acquisitions pour comparer quatre méthodes de correction de distorsion: Block-Matching (BM) (Hedouin et al., 2017), HySCO (Ruthotto et al., 2012), TOPUP (Andersson et al., 2003) et Voss (Voss et al., 2006). La fragmentation par niveaux de la colonne montre l'impact différent de la distorsion entre les bords (C1, C2, T1, T2) et le centre (C3, C4) de la fenêtre d'acquisition. Cette évaluation locale fournit une mesure de performance complémentaire à la comparaison classique avec une image anatomique de référence.

Nous avons aussi proposé un pipeline pour extraire les mesures dMRI moyennes par niveau vertébral dans la moelle épinière et nous avons effectué une analyse statistique pour montrer leur sensibilité associée à la présence et à l'évolution des lésions de SEP dans le même niveau vertébral. Les mesures de diffusion impliquées sont extraites des modèles du tenseur de diffusion et des modèles à boule. Nous montrons que FWW, Stick-AD, FA, MD et DR présentent une différence significative entre les volontaires en bonne santé et les patients atteints de SEP dans la région [C2-C4] de la moelle épinière cervicale. En ce qui concerne FA, MD et RD, d'autres études portant sur la moelle épinière ont déjà été montrées (Valsasina et al., 2005; **?**; **?**; **?**). Notre travail comporte de nombreux ajouts à d'autres études portant sur la moelle épinière; des données relativement volumineuses, neuf évaluateurs, radiologues et lecteurs expérimentés, décrivant les lésions segmentaires sous MS, quantification des mesures de diffusion à l'aide d'une approche atlas exempte de biais de délinéation manuelle et lors de l'extraction métrique, un effet volume partiel est pris en compte, ainsi qu'un contrôle de qualité pipeline afin de garantir une bonne qualité de l'analyse et l'exactitude des résultats. Nous montrons que le modèle à plusieurs compartiments B & S peut fournir de nouvelles informations sur l'évolution de la microstructure tissulaire chez les patients atteints de SEP et doit être inclus dans le processus de traitement et le protocole clinique.

En outre, une autre contribution importante est la manière dont nous avons proposé, l'apprentissage multivarié, d'utiliser les données de diffusion IRM pour détecter automatiquement la présence d'une lésion MS. Sur la base d'une sélection de métriques extraites de la diffusion, nous avons appris un classifieur linéaire à l'aide d'une analyse discriminante linéaire (LDA) et nous avons réduit

la dimension du vecteur de caractéristiques à l'aide de deux stratégies différentes. (1) sélectionner manuellement un ensemble de mesures avec une corrélation croisée limitée, (2) effectuer une analyse en composantes principales (APC), puis apprendre un classifieur linéaire sur l'ensemble réduit d'APC, les deux premiers composants expliquant plus de 65% du la variance. Tout au long de ces stratégies, nous avons évalué les résultats de la classification en utilisant l'aire sous la courbe (AUC) de la courbe de fonctionnement du récepteur (ROC). Nous avons constaté que la combinaison de certaines métriques permet d'atteindre le score de prédiction d'une telle lésion MS et est plus performante que l'utilisation indépendante de chaque métrique. Nous avons montré qu'une combinaison de 3 mesures [FA, MD, DR] et d'une combinaison de 4 mesures [FWW, MD, Stick-AD, RD] donne le meilleur score AUC ROC entre les volontaires en bonne santé et les patients MS atteints de lésion. Ainsi, le choix d'un sous-ensemble de métriques qui apportent des informations complémentaires a considérablement augmenté le score de prédiction de la présence de cette maladie.

Chapter 3

State of the art

b

Contents

3.1 General context

3.1.1 Multiple Sclerosis

Multiple sclerosis (MS) is a demyelinating and inflammatory disease disrupting the flow of information within the central nervous system (CNS) and between CNS and the body (Hachinski et al., 2006). The immune system attacks and damages mistakenly the layer that covers the nerves, called the myelin sheath. This disrupts messages traveling along the nerves causing various symptoms. The specific ones are determined by the locations of the lesions within CNS, and may enclose alteration in sensation or loss of sensitivity including difficulty walking, fatigue, feeling tired, chronic pain, emotional problems, blurred vision, difficulties thinking, among others (Compston and Coles, 2008). For the spinal cord specifically, symptoms are weakness, bladder dysfunction, erectile impotence, constipation, stiffness and painful spasms (Compston and Coles, 2008). The main method for quantifying disability and severity in MS is the Kurtzke Expanded Disability Status Scale (EDSS). EDSS is based on a neurological examination by a clinician assessed by assigning a score to 8 functional systems such as sensory and visual (Kurtzke, 1983).

MS disease is characterized by 3 main features which interact in a complex way; formation of MS lesions in CNS, inflammation, and the destruction of myelin sheaths of neurons. MS lesions in CNS may affect white matter (WM) in the brain stem, the optic nerve and the spinal cord. The peripheral nervous system is also infrequently involved. The role of WM is to carry signals between cortical areas, deep gray matter and the rest of the body. Specifically, MS involves the loss of oligodendrocytes which provides insulation and support to axons in CNS by creating the myelin sheath. Depending on the disease progress, the neuron becomes unable to conduct electrical signals as a result of a partially or completely loss of myelin (Compston and Coles, 2008). Figure.3.1 illustrates an example of healthy and affected nerve cells with the status of myelin sheath.

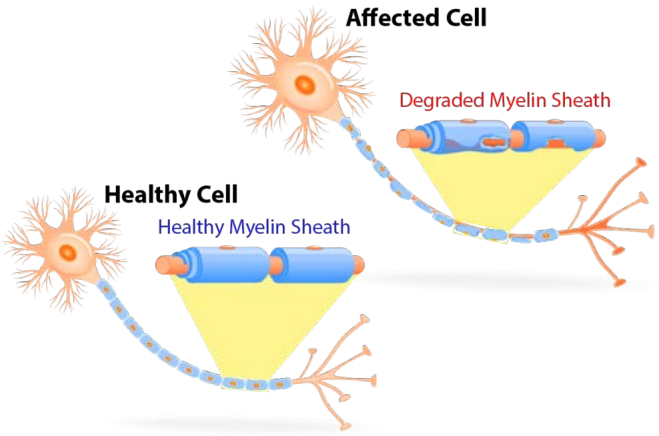

Figure 3.1: Illustrative examples of healthy and affected nerve cells in MS. Image source *pemf-tech.com*

Inflammation is another sign of the MS disease caused by T cells. These cells have an important function in the body's defense. T cells can penetrate into the CNS via disruptions in the blood-brain barrier (BBB) and attack myelin. BBB is responsible of preventing the penetration of T cells into the CNS; it may become permeable in case of an infection by a virus or a bacteria.

This behavior of the immune system is still the topic of active research; the cause and the etiology of MS are still unknown. But scientists believe in a combination of genetic, epigenetic, environmental and lifestyle factors (Muñoz-Culla et al., 2013). Today more than 2.3 million

people around the world are affected by this disease (Vos et al., 2016). MS patients are mostly in countries further away from the equator, and as shown in Figure.3.2, it is more widespread and common in northern Europe (Inglese and Bester, 2010; Koriem, 2016). The origin of this geographical variation and pattern are not yet understood. Some theory attempts tried to combine the data of MS patients into probable explanations, but none has proved definitive. For example, decreased vitamin D production as a result of low sunlight exposure (Koch et al., 2013) and the season of birth which is more mostly in May comparing to November (Kulie et al., 2009). Vaccinations and smoking were studied as risk factor but no association was shown (Marrie, 2004; Ascherio and Munger, 2007).

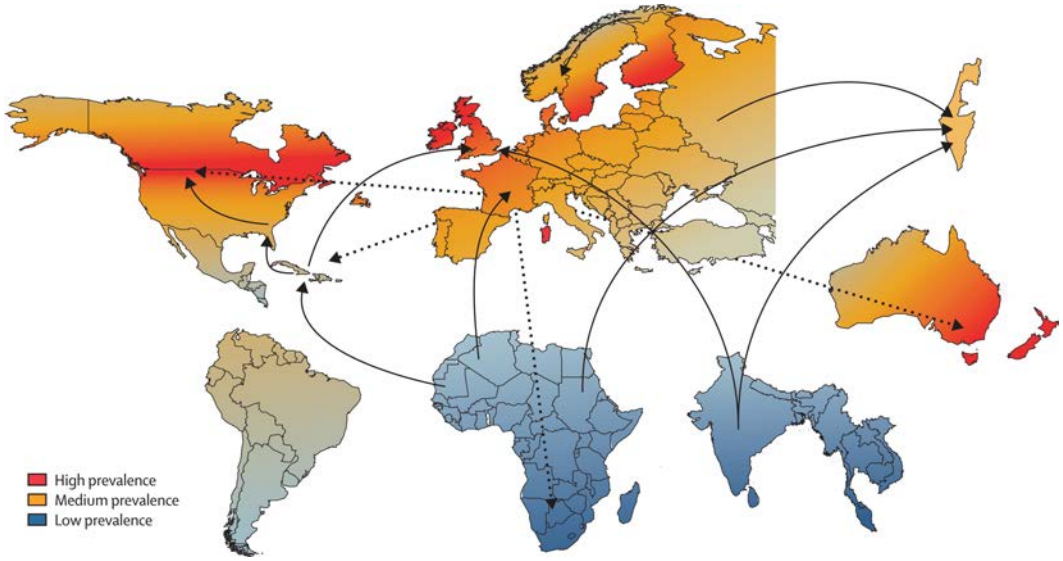

Figure 3.2: Geography of multiple sclerosis: The world map is represented to indicate regions with low prevalence of MS (blue), medium prevalence (orange), high prevalence (red), and absence of regions means the lack of information. The variation of colors is to show the geographical trends. Arrows shows the important migration between low-risk and high-risk zones. Image source: (Compston and Coles, 2008).

Currently, there is no available cure for MS (Hachinski et al., 2006). Existing treatments attempt to ameliorate the situation of MS patients, to help control and to prevent the appearance of new disability or attacks. MS is diagnosed in conjunction with the apparition of specific signs and symptoms and using medical imaging and laboratory testing. Some times, it is diffcult to confirm MS disease regarding the similarity of those signs and symptoms with other diseases. The McDonald criteria is mainly used in diagnosis (Organization et al., 2008). Actually, the National Multiple Sclerosis Society [1] and the Multiple Sclerosis International Federation [2] describe four types or pattern of progression of MS :

- Clinically isolated syndrome (CIS)
- Relapsing-remitting MS (RRMS)
- Primary progressive MS (PPMS)
- Secondary progressive MS (SPMS)

These patterns are characterized by different longitudinal progression of the disease, as depicted on Figure.3.3.

[1] https://www.nationalmssociety.org/
[2] https://www.msif.org/

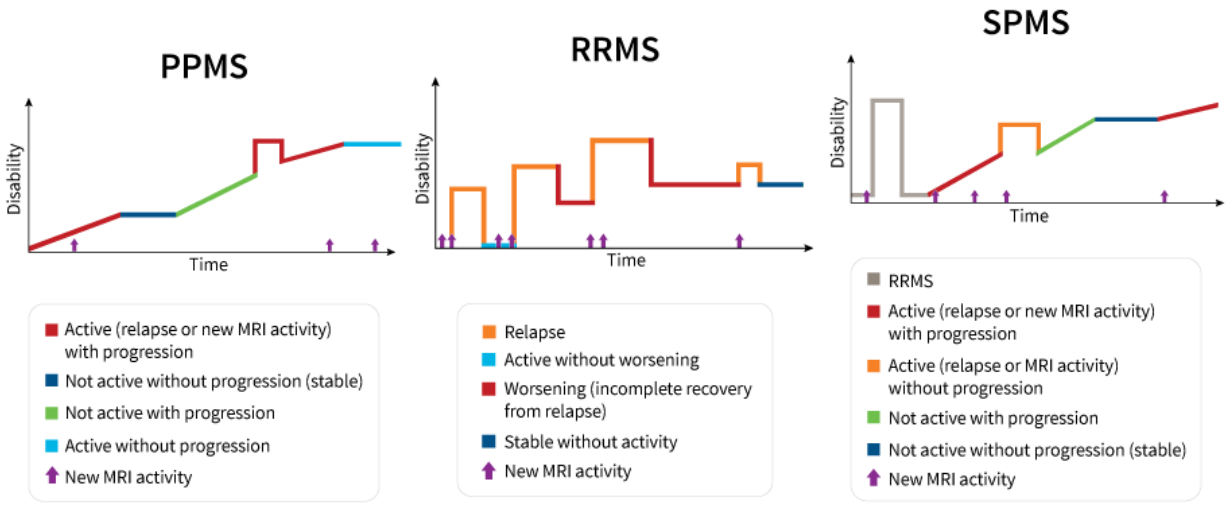

Figure 3.3: Graphics shows the kinds of disease activity that can occur in PPMS, RRMS and SPMS over time. Image source: *www.nationalmssociety.org*.

3.1.2 Magnetic resonance imaging (MRI)

Magnetic resonance imaging (MRI) is a non-invasive medical imaging technology used for creating multi-dimensional anatomical and physiological images of the body. MRI is a medical application of a physical phenomenon known as nuclear magnetic resonance (NMR). The MR scanner excites protons (hydrogen atoms) in water molecule naturally present in the human body using a strong magnetic field and radio-frequency excitation, then measures their response to this excitation. As MRI doesn't use damaging radiation, it is considered non-invasive and can be performed on the CNS, including brain and spinal cord.

MRI offers a powerful and sensitive technique for characterizing MS and provides an important para-clinical tool for lesion detection and treatment monitoring. MRI is now integrated into the McDonald criteria for diagnosis. However, according to the National Multiple Sclerosis Society, about 5% of MS patients have normal MRI, without lesions, when the disease is diagnosed.

Figure 3.4: Approximatif image: An operator uses the control console to perform a scan on a patient using Magnetic resonance imaging (MRI) scanner.

Structural (or conventional) MRI, a category of MRI scan, provides a 3D image with a typical resolution of 1mm, where anatomical structures are visible via T_1- or T_2-weighted contrast, to emphasize contrast between cerebrospinal fluid, gray and white matter. These different contrast are obtained with specific sequences and sets of parameters such as repetition time (TR) and echo

time (TE). This category of MRI is increasingly used and integrated into the clinical routine as a new criteria for the diagnosis of MS. It has a huge impact on this disease by enabling an earlier diagnosis. However, despite its growing role in scientific and clinical investigation of MS, this type of MRI shows poor associations with histological information and/or clinical disability of the MS patient. In addition, it has been shown in (Miller et al., 1998; Filippi and Grossman, 2002; Rovaris et al., 2006) that some regions in white matter appear normal using conventional MRI while they are involved in MS process. Conventional MRI has low specificity with MS pathology and low sensitivity to diffuse tissue injury in normal-appearing white matter (NAWM).

In contrast, quantitative MRI (qMRI) has shown a huge potential to provide intrinsic and normative value to tissue properties useful for diagnosis, prognosis and ultimately clinical trials in MS. MS has benefited mostly from advanced quantitative spinal cord MRI such as functional MRI (fMRI), magnetization transfer ratio (MTR) and diffusion MRI (dMRI) (Agosta et al., 2007a; Inglese and Bester, 2010; Abdel-Aziz and Ciccarelli, 2014). The qMRI techniques commonly used for spinal cord are:

Diffusion MRI (dMRI) is sensitive to microstructural tissue damage, including axonal orientation and demyelination.

Magnetization transfer ratio (MTR) imaging provides information on the structural integrity of the spinal cord and is most often used to derive information regarding myelination status.

Spinal functional MRI (fMRI) has been used to produce high spatial resolution maps of neuronal activity at vertebral levels in response to various stimuli by detecting associated changes in blood flow.

3.1.3 The human spinal cord imaging

CNS consists principally of the brain and the spinal cord which is continuous with the brain and protected by the vertebrae. The spinal cord possesses a thin, long, tubular and mobile structure. It extends from the brain stem to the lumbar region of the vertebral column. According to the surrounding vertebrae, the spinal cord is divided from head to foot into: cervical part [C1 - C7], thoracic part [T1 - T12], lumbar part [L1 - L5], sacral part and coccyx part as illustrated in Figure.3.5. Along its length, the spinal cord varies in width, ranging from 13 mm thickness in the cervical and lumbar parts to 6.4 mm thickness in thoracical part. The average length of the spine is about 45 cm for adults men and around 43 cm for adults women (Goto and Otsuka, 1997; Stroman et al., 2014). In axial view, the spinal cord has an elliptical form. It is protected by the bony structures of the vertebral column and is located inside the vertebral canal. The gray matter (GM) has a butterfly form and located in center of the spinal cord around central canal which contains cerebrospinal fluid (CSF). GM is composed by nerve cell bodies and surrounding by a peripheral region that contains neuronal white matter (WM) tracts. Figure.3.5 presents a model labeled of a cross-section of the spinal cord.

CNS coordinates human actions by transmitting signals to and from CNS and the peripheral nervous system (PNS). As a part of the CNS, the spinal cord is the main pathway that connects the brain to PNS. Spinal cord controls the transmission and the reception of nerve signals from the motor cortex to the body, and from the afferent fibers to the sensory cortex.The spinal cord contains the motor neurons which controls both voluntary and reflex movements such as walking.

The spinal cord is a clinically common and eloquent site frequently involved in MS. Spinal cord lesions in MS patients are frequent in the cervical part, restricted to two vertebral levels in length, fill less than half of the cross sectional area of the spinal cord and are generally peripheral

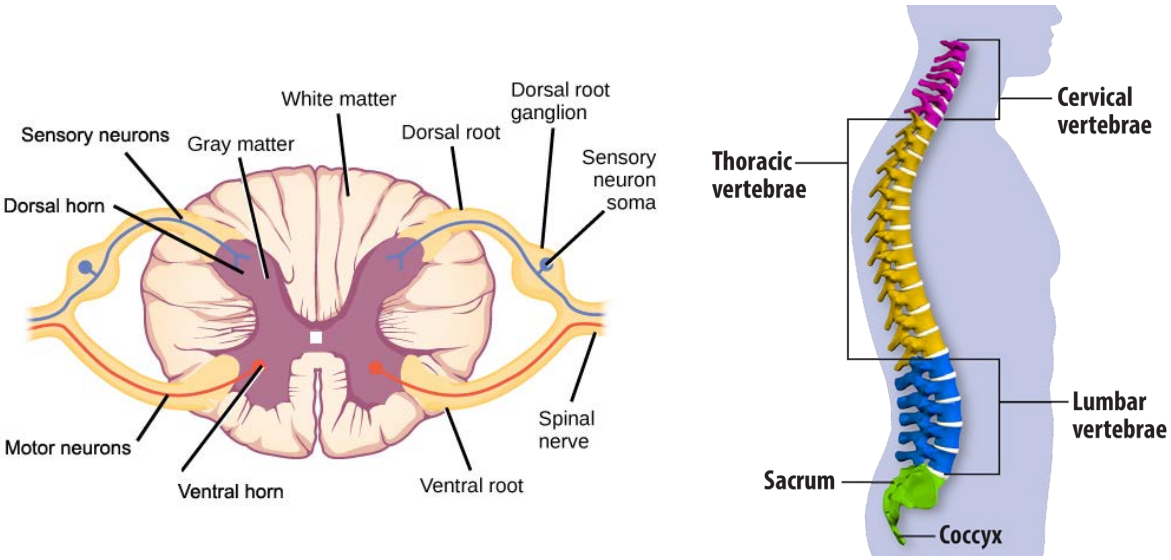

Figure 3.5: Illustration of the anatomy of the human spinal cord. Axial view (left) and lateral view (right) of spinal cord. Images source: *www.courses.lumenlearning.com* and *www.bey-om-sin.com*

(Wheeler-Kingshott et al., 2014). However, contrary to the brain, there are few studies and non-invasive investigation to enhance our understanding of human spinal cord function affected by MS.

Relatively few research laboratory in the world are actively studying and investigating spinal cord imaging (Stroman et al., 2014). This can be explained by the specific anatomical arrangement of the spinal cord and the surrounding structures which limits its accessibility for research (Stroman et al., 2014). Firstly, acquiring MRI scan in spinal cord site is especially challenging due to the presence of various surrounding tissue types: bone, CSF, gray and white matter, muscle, fat and air. This non-uniform environment causes loss of signal intensity and susceptibility-induced distortion. Secondly, the elongated shape of the spinal cord anatomy requires a large field of view (FOV) in the superior-inferior direction and its small cross-sectional size requires high spatial resolution. The third challenge for spinal cord imaging arises from the physiological motion within the spinal canal (Stroman et al., 2014).

The prevalence of spinal cord abnormalities in MS patients is about 74-85% and can reach up to 90% of patients with definite MS. This range is explained by differences in the imaging technique, clinical analysis and the MS patients group. For patients with clinically isolated syndrome (CIS), the ratio is around 30-40% (Lycklama et al., 2003; Wheeler-Kingshott et al., 2014). Such study confirmed for 5% of MS patients the value of additional spinal cord MRI when brain MRI is normal (Thorpe et al., 1996). Other studies found a correlation between atrophy of cervical part of the spinal cord and EDSS (Lin et al., 2004). Table. 3.1 summarizes some diffusion MRI studies established on MS patients. Note that the following are some parameters of diffusion MRI will be explained in next sections, AD: axial diffusivity; FA: fractional anisotropy; MD: mean diffusivity; RD: radial diffusivity.

3.2 Principles of diffusion MRI

Diffusion MRI is a relatively recent field of research, the first in vivo application of diffusion NMR was performed in the mid 80's (Le Bihan and Breton, 1985). There is a growing interest for dMRI because it helps understand the structural architecture of the brain and spinal cord connexions,

Studies	Data	ROI	Findings in MS patients
(Valsasina et al., 2005)	44 patients, 17 controls	C1-C5	FA decreases and the average cord FA correlates with EDSS
(Agosta et al., 2007a; Agosta et al., 2007b)	42 patients, 9 controls	C2,C3	FA and cross-sectional area decrease, MD increase
(Hesseltine et al., 2006)	24 patients, 24 controls	C2-C3	In NASC, FA is lower significantly in lateral, posterior and central.
(Miraldi et al., 2013)	32 patients, 17 controls	C2,C7	For NASC right column, FA decrease and RD increase in C2 and at C7, MD increase. No significant correlation with EDSS.
(von Meyenburg et al., 2013)	41 patients, 28 controls	C2,C7	For NASC right column, FA decrease and RD increase in C2 and at C7, MD increase.

Table 3.1: Summary of clinical imaging studies of multiple sclerosis using diffusion MRI parameters. AD: axial diffusivity; FA: fractional anisotropy; MD: mean diffusivity; RD: radial diffusivity; NASC: normal-appearing spinal cord.

in neuroscience imaging, surgical planning and in other medical applications. Diffusion MRI is a non-invasive MRI method that measures the local mobility profile of water molecules, from which we can describe and characterize the geometry of the underlying tissue micro-structure. To do so, diffusion MRI measures the average diffusion of water molecules, which probes the structure of the biological tissue at scales much smaller than the imaging resolution. In an environment without any hindrance, e.g. a glass of water, the diffusion of water molecules is Brownian. But in fibrous tissue such as white matter, water molecules tend to diffuse preferentially along the fibers. Using this physical phenomenon, researchers are able to obtain information about the neural architecture *in vivo* and provide models for brain and spinal cord connectivity.

3.2.1 Diffusion basics

At the microscopic scale, water molecules in tissues are in motion and collide with each other as a result of their thermal agitation. Water molecules are not static over time, they undergo Brownian motion (Brown, 1828). This effect, water molecules motion, can be characterized by the so-called diffusion coefficient D. In free water, this displacement is equal whatever the direction of observation. This type of diffusion is named as *isotropic diffusion*. However, in fibrous tissue space, the water molecule motion is restricted and hindered by tissue structures. The displacement is faster along one specific direction and lower along others. This type of diffusion is named as *anisotropic diffusion*. Figure.3.6 shows an example of these diffusions in tissue.

These differences in diffusion can be measured using MRI; at each spatial position (each voxel in the image), the motion of water molecules can be encoded and formulated by sensitizing the MRI scanner to the mean displacement done during a certain time. In order to explain more diffusion MRI of spinal cord, we explore the basic physical principles describing the diffusion process. So, the flux of water molecules in each direction in such area can be written in function of the diffusion coefficient D using Fick's first law (Fick, 1855):

$$J = -D\nabla C \tag{3.1}$$

where J is the mass flux (units: $mass/time$), D is the diffusion coefficient (units: $area/time$) and

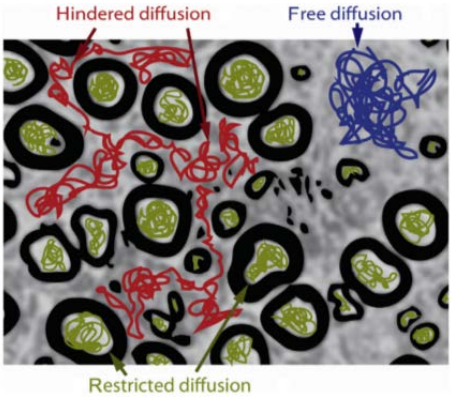

Figure 3.6: A model of diffusion type in different tissue environment. Isotropic diffusion (blue): Brownian motion in free space. Anisotropic diffusion; Restricted (green): motion is restricted within an intra-axonal space, Hindered diffusion (red): free motion but within extra-axonal space. Image source: (Schneider and Wheeler-Kingshott, 2014)

C is the concentration of water molecules (units: *mass/volume*). The minus sign embodies the notion that molecules move from area with high concentration to area with low concentration. J is proportional to C and D. But, D is an intrinsic property that proportional to quantity of diffusing protons, microstructural features and the temperature of the medium.

Figure.3.7 shows an illustrative experience of diffusion. A drop of red ink was introduced into a glass of water. In the beginning, the ink remains concentrated at the point of release, but by the time the ink spreads radially and spherically. By the time, the concentration of the ink particles becomes uniform in the glass and the net flux of particles turns off.

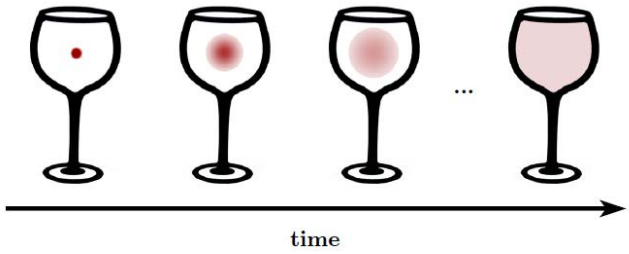

Figure 3.7: Diffusion at the macroscopic scale: net flux of ink molecules from a region of high concentration to a region of low concentration. Image source: Ben Jeurissen's PhD report.

The concentration of water protons is described in terms of probability of their motion across both space and time. Einstein introduced the *diffusion probability density function*, $p(r_0|r,t)$, which quantifies the displacement net vector from the initial position r_0 to r (units: m) within a certain *diffusion time* t (units: s). Assuming that function follows a Gaussian distribution, Einstein's equation for mean displacement applies (Einstein, 1956):

$$\langle r - r_0 \rangle = \sqrt{6Dt} \tag{3.2}$$

and it results in the solution:

$$p(r_0|r,t) = \frac{1}{\sqrt{4\pi Dt)^2}} e^{-\frac{\langle r-r_0 \rangle^2}{4tD}} \tag{3.3}$$

Then, to have to have the basis of diffusion MRI, we have to apply the Gaussian distribution of water protons into the Bloch equations (Cohen-Adad and Wheeler-Kingshott, 2014).

3.2.2 The Apparent Diffusion Coefficient

The *estimated* value of the diffusion coefficient in MRI in such tissue is often referred to as an *apparent diffusion coefficient* (ADC) (Le Bihan et al., 1986). When there is unordered tissue microstructure, ADC is equal no matter in which direction it is estimated. By the turn, p takes the form of a sphere which means isotropic diffusion. However, when there ordered fibers microstructure, ADC depends on the orientation these fibers. Thus, p takes the form of an ellipsoid which means anisotropic diffusion. The general diffusion displacement probability density function of water molecules is extremely complex. The most popular proposed model of diffusion is diffusion tensor imaging (*DTI*) model (Basser et al., 1994b) which can generalize Einstein's and Fick's law of diffusion. The scalar diffusion coefficient can be replaced by a diffusion *tensor* $\mathbf{D}$ which is related to the covariance matrix of spins displacement as follows:

$$\mathbf{D} = \frac{\langle \mathbf{r} \cdot \mathbf{r}^{\mathrm{T}} \rangle}{6t} = \begin{pmatrix} D_{xx} & D_{xy} & D_{xz} \\ D_{xy} & D_{yy} & D_{yz} \\ D_{xz} & D_{yz} & D_{zz} \end{pmatrix}. \tag{3.4}$$

$\mathbf{D}$ is a symmetric and positive-definite matrix and therefore it contains only 6 unique elements.

3.2.3 Diffusion in neural tissue

Neural tissue of spinal cord is built from nerve cells or neurons which transmit information by electrical and chemical signaling. It is formed by three parts: cell body, the dendrites and the axon (Figure.3.8). From the cell body, many dendrites extend. Both of them receive chemical signals from other neurons and process the information. The axon transmits the received information from the cell body towards other nerve cells using electrical conduction. The speed of axon transmission is raised by the insulator named myelin sheet. At the macroscopic level, the spinal cord is made up of three major components: cerebrospinal fluid (CSF), GM and WM. WM consists mostly of myelinated axons passing to and from brain, or different segments of the spinal cord. GM consists of nerve cell bodies and inter-neurons.

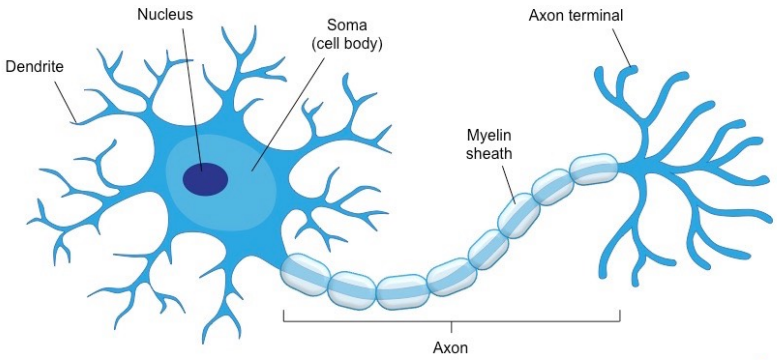

Figure 3.8: Structure of typical neuron. Image source: *www.socratic.org*

WM is composed of bundles of axons which contributes to diffusion anisotropy inside it; As seen previously, diffusion is more fluid and less restricted along the axon than perpendicular to it. Basing on this property, it will be possible to extract specific geometric and structural features about the WM medium (Figure.3.9).

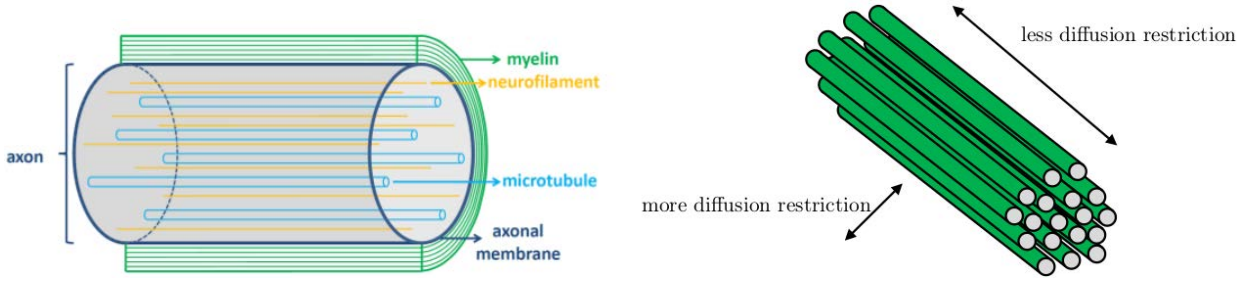

Figure 3.9: Schematic representation of a single axon (left) and its surrounded substance. A bundle of axons (right) typically found in the WM. Diffusion is more effective parallel to the WM bundles than perpendicular to it. Image source: Ben Jeurissen's PhD report.

3.2.4 Measuring diffusion with MRI

Nuclear Magnetic Resonance

NMR was firstly used to measure properties of substances in chemistry to perform NMR spectroscopy. Its principles were described by Felix Bloch and Edward Mills Purcell (Bloch, 1946; Purcell et al., 1946). The essential property of nuclei such as hydrogen (proton) is their intrinsic magnetic moment. When the spin of such proton is immersed into a strong magnetic field $\mathbf{B_0}$ (units: T), the spin will tend to align with this field and the moment of each spin precesses with a given frequency around this field called the Larmor frequency (units: rad/s):

$$\omega_0 = \gamma ||\mathbf{B_0}|| \tag{3.5}$$

where γ is the gyro-magnetic ratio (units: rad/(sT)) (see Figure.3.10). The human body is made up at 80% by water which contains protons. For 3T clinical scanner, the Larmor frequency is 127.6 MHz. At resting or normal state, the spins do not rotate in phase and the transverse contributions of them tends to cancel each other. The net magnetization, M, is aligned with the magnetic field $B0$. As soon as we excite spins by a radio signal $\mathbf{B_1}$ oscillating with pulsation ω_0, these spins begin to rotate in phase and to precess away from the $\mathbf{B_0}$ axis. The flip angle, θ, is proportional to the duration and the magnitude of the radio frequency pulse (see Figure.3.10).

Magnetic field gradients

The magnetic field can be made to vary over the spinal cord or the brain in order to reconstruct a 3D image. This can be done by the addition of a linear magnetic field gradient G on top of the main magnetic field B_0 (Carr and Purcell, 1954; Tuch et al., 2003):

$$B(x) = B_0 + Gx \tag{3.6}$$

where x is the position along the gradient direction as shown in Figure.3.11. By the way, given Equation. 3.5, the precessional frequency of the spins in such position x can be described as:

$$\omega(x) = \gamma B(x) = \gamma(B_0 + Gx). \tag{3.7}$$

The precession frequency which depends on the position x is the basis of spatial and diffusion encoding in MRI.

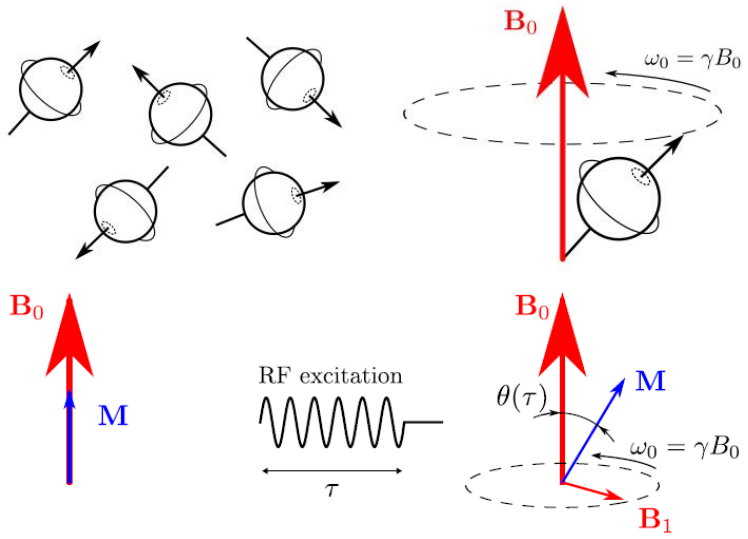

Figure 3.10: Net magnetization in presence of a strong magnetic field (1st line). Spin in rest state (2nd line,left). Spin under RF excitation(2nd line,right). Net magnetization in presence of a strong magnetic field. Images source: E. Caruyer's PhD report.

3.2.5 Diffusion MRI

Diffusion MRI (dMRI) is an imaging technique based on the physical principles of diffusion NMR. It permits the measuring of water diffusion within a spatial space in *in vivo* tissue. To measure diffusion, we need an MRI sequence with two diffusion-encoding gradients positioned symmetrically around the 180° RF pulse (Stejskal and Tanner, 1965). Consider two rectangular diffusion gradient pulses $\mathbf{g}(t)$ along the z-direction. The *dephasing* gradient pulse induces a phase shift ϕ_1 of the spin transverse magnetization:

$$\phi_1 = \gamma \int_0^{\delta} g_z(t) z(t)\, \mathrm{d}t = \gamma \delta g_z z_1 \tag{3.8}$$

where δ is the duration time of $\mathbf{g}$(t) and $z(t) = z_1$, spin position, is assumed to be constant during the short pulse duration δ. The duration δ and the strength g_z of the gradient define the amount of *dephasing*. Equivalently, the *rephasing* gradient pulse induces a phase shift ϕ_2:

$$\phi_2 = -\gamma \int_{\Delta}^{\Delta+\delta} g_z(t) z(t)\, \mathrm{d}t = -\gamma \delta g_z z_2 \tag{3.9}$$

where the minus sign reflects the application of the 180° RF pulse and Δ is the time between the two diffusion gradient pulses. When spins are *not* undergoing any diffusion along the gradient direction ($z_1 = z_2$), the net induced phase shift ϕ will be zero:

$$\phi = \phi_1 + \phi_2 = \gamma \delta g_z (z_1 - z_2) = 0 \tag{3.10}$$

Conversely, spins which undergo diffusion along the gradient direction during Δ will experience a net phase shift:

$$\phi = \gamma \delta g_z (z_1 - z_2) \neq 0 \tag{3.11}$$

These spins are not completely refocused, resulting a signal loss (Cercignani and Horsfield, 2001; Bammer, 2003). Generally, the signal loss at position $\mathbf{r}$, called pulsed gradient spin-echo signal (PGSE) S is given by:

$$S = S_0 \langle e^{i\phi} \rangle \leq S_0 \tag{3.12}$$

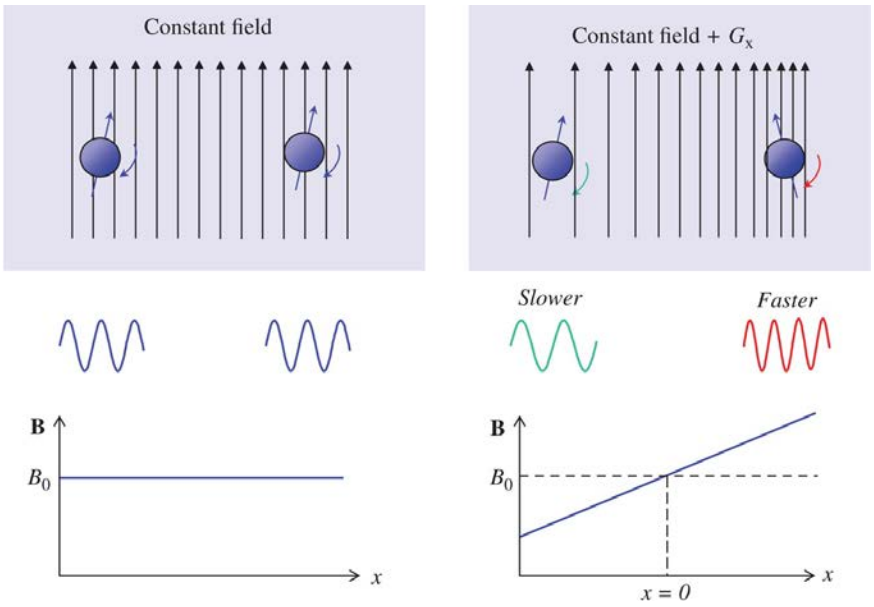

Figure 3.11: Effect of field gradient on spins. B_0 only, all spins precess at the same frequency (left). $B_0 + Gx$: precession frequency depends upon position. Image source: (McRobbie et al., 2017).

where S_0 is the signal intensity in the absence of a diffusion-encoding gradient, i.e. $\mathbf{g} = 0$ and $\langle e^{i\phi} \rangle$ represents the ensemble average of the spin population.

As presented in Section 3.2, the spin displacement distribution pursues the Brownian Motion which means that the phase of the spins also is randomly distributed. (Stejskal and Tanner, 1965) showed that the signal attenuation S/S_0 can be written as the 3D Fourier transform $\mathcal{F}$ of $p(r \mid r_0, \tau)$:

$$S/S_0 = \int p(r \mid r_0, \tau) e^{iq^T (r_0 - r)} \, dr = \mathcal{F}[p(r)] \tag{3.13}$$

where $q = \gamma \delta g$ is the q-vector and $\mathbf{g}$ is the applied diffusion gradient vector. The space of all possible 3D q-vectors is the so-called *q-space*. Moreover, for isotropic microstructure, the conditional probability density function $p(r \mid r_0, \tau)$ is defined as:

$$p(r \mid r_0, \tau) = \frac{1}{\sqrt{[4\pi\tau D]^3}} e^{-\frac{\|r - r_0\|^2}{4\tau D(r)}} \tag{3.14}$$

Combining Eq. 3.13 and 3.14, we can relate the signal attenuation S/S_0 to the diffusion coefficient D (ADC value) of the underlying tissue, it is also *so-called* Stejskal-Tanner relation:

$$S/S_0 = e^{-bD} \tag{3.15}$$

where b is the diffusion weighting tensor factor introduced by (Le Bihan et al., 1986):

$$b = \gamma^2 \delta^2 (\Delta - \frac{\delta}{3}) \|\mathbf{g}\|^2 . \tag{3.16}$$

A schematic illustration of the previous steps of framework acquisition is introduced in Figure.3.12. For anisotropic medium such as WM in spinal cord, the diffusion coefficient D depends on the direction and the strength of $\mathbf{g}$, Δ and δ. In clinical practice, dMRI scan are usually acquired using Echo-Planar Imaging (EPI) sequence (Stehling et al., 1991) which offers faster acquisition with less motion artifacts but more risk of distortion. The first attempt of studying anisotropic water diffusion in CNS for a cat using dMRI was by (Moseley et al., 1990) in which it was demonstrated the anisotropic water diffusion in WM and the isotropic water diffusion in GM. In parallel, (Chenevert et al., 1990) confirmed the anisotropic water diffusion in *in vivo* human WM. Later, other study found the anisotropic water diffusion in spinal cord (Barker, 2001).

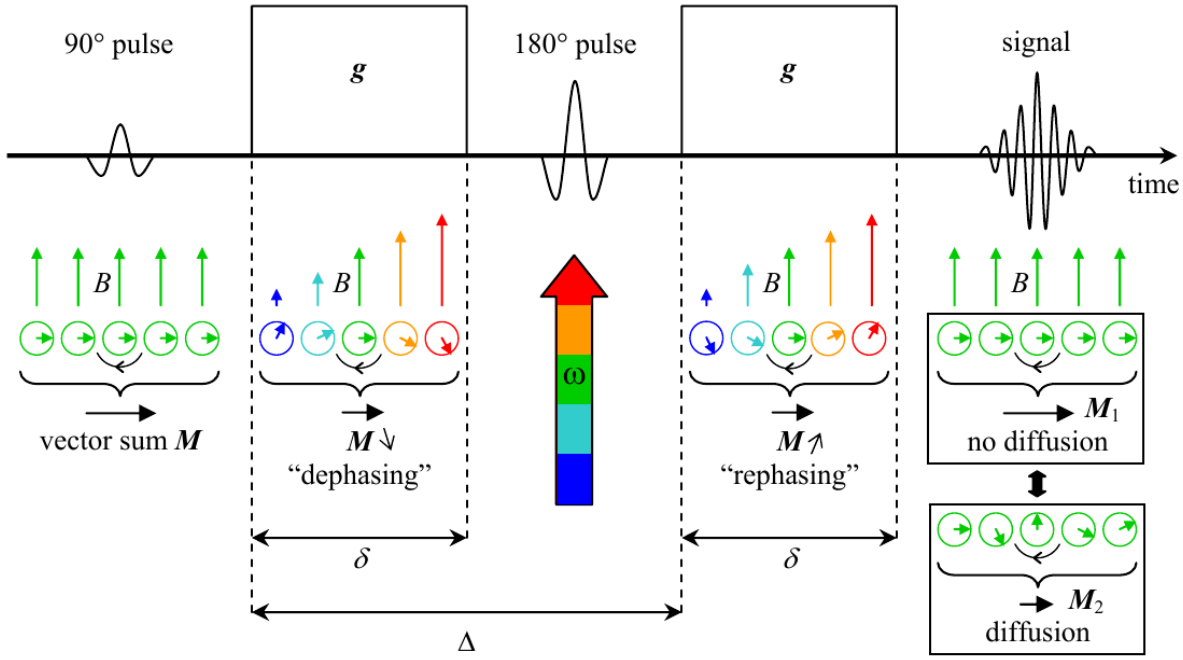

Figure 3.12: A schematic illustration of the diffusion MRI sequence. The length of the colored vertical arrows indicates the strength of the magnetic field B which is non-uniform during the application of the gradients **g**. After the first gradient application following the 90° RF pulse, signals lose their uniform phase ('Dephasing': the vector sum of the magnetic spin moments **M** decreases) because each proton starts to precess at different rates ω depending on its position in space (the color-encoding represents the amount of this precession rate). After the second gradient application following the 180° RF pulse, the system restores the uniform phase ('Rephasing': **M** increases). This rephasing is complete only when spins do not undergo a random motion (i.e., do not diffuse) during the time Δ in between the two applications of the gradients ($\|\mathbf{M}_1\| \geq \|\mathbf{M}_2\|$). Image and paragraph source: A. Leemans's PhD report.

3.3 Modeling the diffusion properties

Several reconstruction techniques were developed for diffusion MRI such as DTI, Ball-and-Stick (B&S), neurite orientation dispersion and density imaging (NODDI) and Q-Ball Imaging (QBI). This section will review the models we used in our work. Detailed reviews on reconstruction models are available in (Hagmann et al., 2006; Alexander, 2005). It is important to emphasize that the type of reconstruction model is strongly related to acquisition parameters of the dMRI sequence (*q-space* sampling). Figure.3.13 gives a general overview of some reconstruction models for diffusion MRI data with the recommended *q-space* sampling, modeling constraints and acquisition time.

3.3.1 Diffusion Tensor Imaging (DTI)

Based on Equation. 3.3, Equation 3.13 can be modified to estimate the full diffusion tensor (Basser et al., 1994a):

$$S(r)/S_0(r) = e^{-q^T Dq(\Delta - \frac{\delta}{3})} = e^{-b\,(\frac{g}{\|\mathbf{g}\|})^T D(\frac{g}{\|\mathbf{g}\|})} \tag{3.17}$$

This equation grants the estimation of the apparent diffusion tensor **D** from a selection of dMRI images $S(r)$ on different gradients directions and a reference image $S_0(r)$. As described previously, **D** contains only 6 unique elements, at least 6 dMRI scans are required.

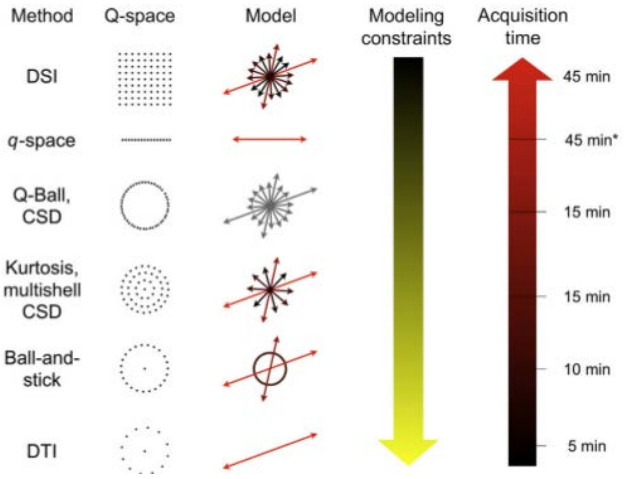

Figure 3.13: General overview of some reconstruction models for diffusion MRI data. B&S model provides the orientation and magnitude for various anisotropic compartments. DTI is the simplest model with the fast acquisition. Image source: (Cohen-Adad and Wheeler-Kingshott, 2014).

The probability density function $p(r \mid r_0, \tau)$ given by Eq. 3.3 characterizes the molecular diffusion. From this equation, the diffusion tensor field $\mathbf{D}$ is considered as a covariance matrix describing the translational displacement of this diffusion. Hence, to consider the physical interpretation of $\mathbf{D}$, the probabilistic iso-surface shape of molecular diffusion is represented by an ellipsoid shape. As $\mathbf{D}$ is a symmetric and positive definite second-rank tensor, it can be decomposed into real eigenvalues and eigenvectors:

$$\mathbf{D} = \mathbf{E} \cdot \Lambda \cdot \mathbf{E}^{-1} \tag{3.18}$$

with

$$\mathbf{E} = \begin{pmatrix} \mathbf{e_1} & \mathbf{e_2} & \mathbf{e_3} \end{pmatrix} \qquad \text{and} \qquad \Lambda = \begin{pmatrix} \lambda_1 & 0 & 0 \\ 0 & \lambda_2 & 0 \\ 0 & 0 & \lambda_3 \end{pmatrix} \tag{3.19}$$

are respectively the matrix of orthonormal eigenvectors $\mathbf{e_i}$ and the diagonal matrix of eigenvalues λ_i, with i $\in \{1,2,3\}$. In general, the first eigenvector $\mathbf{e_1}$ (i.e., corresponding with λ_1) describes the predominant diffusion direction. Figure.3.14 illustrates an example of diffusion tensor imaging (DTI).

In addition to the directional information, other scalar measures can be computed from eigenvalues which can reach our access to the tissue microstructure. Here we summarize the most popular measures (please refer to (Westin et al., 2002) for a good review of other measures):

Mean diffusivity (MD) which measures the average displacement of the water molecules. MD is much higher in CSF than in WM and GM.

$$MD = \frac{\lambda_1 + \lambda_2 + \lambda_3}{3} = \langle \lambda \rangle \tag{3.20}$$

Fractional anisotropy (FA) which measures the degree of diffusion anisotropy. FA is much higher in WM than in CSF and GM. Since to the organized structure of WM, FA is regularly used as a delegate marker for it.

$$FA = \sqrt{\frac{3}{2}} \frac{\sqrt{(\lambda_1 - \langle \lambda \rangle)^2 + (\lambda_2 - \langle \lambda \rangle)^2 + (\lambda_3 - \langle \lambda \rangle)^2}}{\sqrt{\lambda_1^2 + \lambda_2^2 + \lambda_3^2}} \tag{3.21}$$

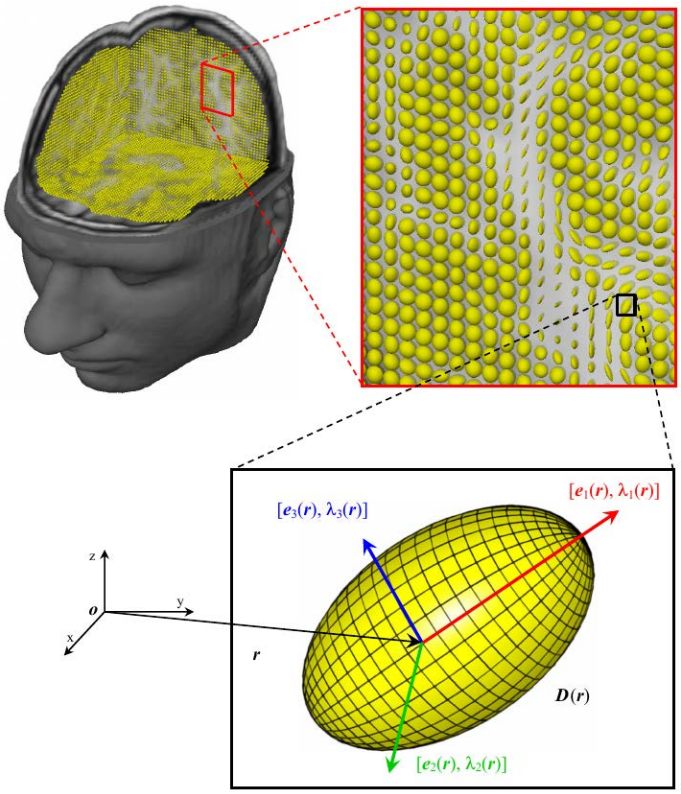

Figure 3.14: Ellipsoidal representation of the diffusion tensor field. Note that every voxel corresponding to position $\mathbf{r}$ of a dMRI scan, is described by the eigenvectors $e_i(\mathbf{r})$ and eigenvalues $\lambda_i(\mathbf{r})$ of the diffusion tensor $\mathbf{D}(\mathbf{r})$. Image source: A. Leemans's PhD report.

Axial diffusivity (AD) $\lambda_{\|}$, which measures the diffusion along the first eigenvector:

$$AD = \lambda_1 \tag{3.22}$$

Radial diffusivity (RD) $\lambda_{\perp}$, which measures the average diffusion perpendicular to the first eigenvector:

$$RD = \frac{\lambda_2 + \lambda_3}{2} \tag{3.23}$$

DTI model is increasingly used to characterize neuropathology such as MS. Recently, extensive research and studies have greatly advanced our knowledge about the usefulness of several measures extracted by DTI model as we present in previous section in Table. 3.1. These studies demonstrated the sensitivity of these features to MS lesions in WM medium for spinal cord. MS lesion and inflammation are characterized by subsequent microstructural changes in WM. These affect the diffusion signals and the microstructural composition of a voxel. Depending on the neuropathology disease, several cases of DTI profile take place by influencing the value of $\lambda_{\perp}$ and $\lambda_{\|}$ (Wang et al., 2011; Zhang et al., 2012). Figure.3.15 illustrates how the neuropathology can affect DTI measures.

While DTI model has an unprecedented ability for characterizing WM properties of the *in vivo* human spinal cord and brain, findings can sometimes be ambiguous. Indeed, the DTI model is inaccurate in the case of multiple WM fibers cross or merge within a voxel (Alexander et al., 2001; Tuch et al., 2002; Wheeler-Kingshott and Cercignani, 2009). DTI is inadequate to describe multiple fiber orientation within an individual voxel which can be considered as averaging of different oriented fibers. This effect, called the Partial Volume Effect (PVE), is taking place when

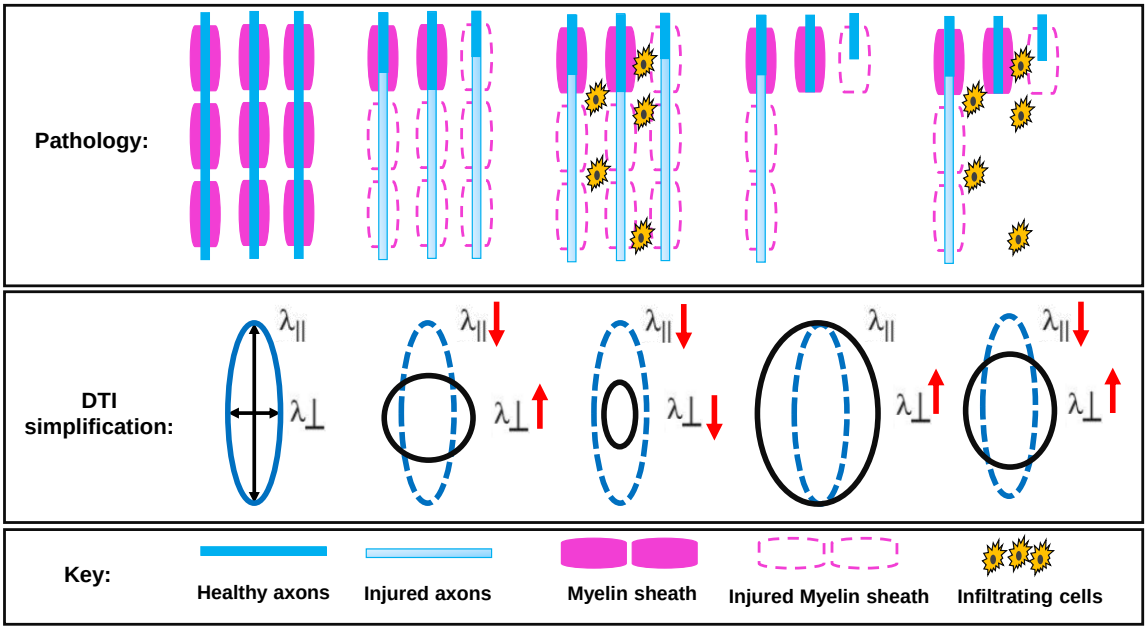

Figure 3.15: Schematic diagrams illustrating how neuropathology may affect DTI measures. Dashed blue ellipsoid represents DTI profile for normal myelinated with $\lambda_{\parallel} > \lambda_{\perp}$. Black drawings (elipsoid and circle) represent new DTI profile for abnormal tissue. (a) Normal myelinated axons and the corresponding DT,$\lambda_{\parallel}$, $\lambda_{\perp}$. (b,c) Axon and myelin injury with and without infiltrating cells. (d,e) Axon and myelin injury with axonal loss, with and without cell infiltrating cells.

the imaging protocol has a coarse resolution or when acquiring small structures. By the way, DTI is only well-founded for unidirectional fiber bundles and we need higher order model to be able to describe non-Gaussian distributions. Also, by considering Figure.3.15, one can understand that DTI measures are not sufficient to investigate pathology properties. Thus, more sophisticated diffusion MRI models are necessary.

3.3.2 Ball-and-Stick Model

The Ball-and-Stick (B&S) model was introduced by (Behrens et al., 2003; Behrens et al., 2007) and there are several numerical implementations freely available. B&S is a multiple tensor (multi compartment) model. The first compartment is *stick*, anisotropic component, which has fiber direction $\mathbf{n}$ and diffusivity d as parameters (Behrens et al., 2003). The *stick* compartment describes diffusion in an idealized cylinder with zero radius($\lambda_{\perp} = 0$). The signal for this component is:

$$S_1 = \exp\left(-bd(\mathbf{n}\cdot\mathbf{G})^2\right) \tag{3.24}$$

The second compartment is *ball*, an isotropic component which has only the diffusivity d_0 as parameter in its signal:

$$S_2 = \exp(-bd_0) \tag{3.25}$$

The global signal model is

$$S/S_0 = (1-f)S_1 + fS_2, \tag{3.26}$$

where f is the free water weight (FWW), the volume fraction of free water in the corresponding voxel. B&S is the most popular multi tensor model as it reduces the number of requested parameters (4 parameters in total). However, B&S doesn't provide information about radial diffusivity.

Model	Form	Degrees of freedom
Intra-axonal compartment models		
 Stick	$S = exp\left(-bd(\mathbf{n}\cdot\mathbf{G})^2\right)$	d, θ, Φ
Extra-axonal compartment models		
 Ball	$\mathbf{D} = d\mathbf{I}$	d
 Tensor	$D = d_{\|\|}\mathbf{n}\mathbf{n}^T + d_{\perp 1}\mathbf{n}_{\perp 1}\mathbf{n}_{\perp 1}^T + +d_{\perp 2}\mathbf{n}_{\perp 2}\mathbf{n}_{\perp 2}^T$	$d_{\|\|}$,$d_{\perp 1}$,$d_{\perp 2}$, θ, Φ, α

Table 3.2: Intra-axonal compartment models. The fibre orientation n is defined by the angles θ, Φ

3.4 Conclusion

In this chapter, we have presented a review of state-of-the-art for the most important topics and themes involved in our work. Firstly, we describe the multiple sclerosis disease within its signs, some of symptoms, pattern of progression, and world distribution. Secondly, we give an overview about the magnetic resonance imaging and its potential to characterize MS. Thirdly, we describe briefly the spinal cord anatomy and its prevalence of abnormalities in MS patients. We summarize also several spinal cord clinical imaging studies of multiple sclerosis using diffusion MRI parameters. Fourthly, we explain the principles of diffusion MRI modality from the basic. Finally, we describe two reconstruction techniques for diffusion MRI used in thus manuscript: Diffusion Tensor Imaging and Ball-and-Stick Models. In addition, we introduce each contribution chapter by more detailed and specific state-of-the-art.

Chapter 4

Distortion correction of diffusion MRI for spinal cord

Contents

4.1 Introduction

Echo-Planar-Imaging (EPI) is a fast and efficient magnetic resonance imaging (MRI) acquisition technique that has been increasingly used in medical imaging applications (Stehling et al., 1991). Besides the substantial reduction of scan time, EPI is desirable for diffusion-weighted imaging (DWI) and functional MRI in neuroscience as it produces images with high signal-to-noise ratio (SNR). However, EPI suffers from its high sensitivity to the B_0 field inhomogeneities. B_0 field inhomogeneities are caused by the local susceptibility variations in the human body; therefore they depend on the strength of the magnetic field, the subject and his orientation in the scanner.

In this respect, *in vivo* spinal cord imaging is especially challenging due to the presence of various surrounding tissue types: bone, CSF, gray and white matter, muscle, fat and air. Besides, the elongated shape of the spinal cord anatomy requires a large field of view (FOV) in the superior-inferior direction and its small cross-sectional size requires high spatial resolution. These requirements extend the readout durations in EPI which in turn distorts and blurs the image along the phase-encoding direction (PED). Also, a wide echo-spacing (ESP) (i.e., interval between two consecutive k-space lines) creates distortions due to B_0 field inhomogeneity.

These effects deform the shape of the reconstructed spine image so that a voxel normally at position $\mathbf{r}$ appears at a position $\mathbf{r} + \mathbf{d}_{\text{PED}}(\mathbf{r})$. Depending on its location in an EPI image, the displacement $\mathbf{d}_{\text{PED}}(\mathbf{r})$ can be expressed (Cohen-Adad and Wheeler-Kingshott, 2014) as:

$$\mathbf{d}_{\text{PED}}(\mathbf{r}) = \frac{\Delta f(\mathbf{r}) \;\; \text{ESP} \;\; \text{FOV}_{\text{PED}}}{N_{int} \;\; R}, \tag{4.1}$$

where $\Delta f(r)$ (in Hertz) represents the B_0 field inhomogeneity observed at position $\mathbf{r}$, ESP (in seconds) is the echo-spacing, FOV_{PED} is the FOV in PED (in m), N_{int} is the number of interleaves in EPI and R is the acceleration factor for parallel imaging. The displacement caused by distortion is proportional to the local magnetic field inhomogeneity. The relatively long times between sampling points in phase-encoding direction (PED) makes spatial distortion appears mainly along this direction. Thus, distortion is practically limited to PED and negligible in others directions (Jezzard and Balaban, 1995; Macdonald and Ruthotto, 2016). In addition to the spatial distortion presented above, there also is an intensity distortion in EPI (Jezzard and Balaban, 1995).

As seen in Eqn 4.1, increased B_0 field inhomogeneity, increased ESP and a large FOV in the PED give a share to geometric distortion. For example, with typical values in the spine for the EMISEP imaging protocol: $ESP = 0.95$ms, $FOV_{PED} = 16$cm, local B_0 field inhomogeneity $\Delta f(r) = 754.28$Hz and acceleration factor (GRAPPA parallel imaging) $R = 2$ could create local displacement up to 5.73cm for a single-shot EPI (N_{int} = 1) (Cohen-Adad and Wheeler-Kingshott, 2014).

Various acquisition-based solutions have been proposed to reduce susceptibility artifacts for spinal cord imaging but many of them are not available on clinical scanners. As seen in Eqn 4.1, some imaging parameters can be adjusted to reduce $d_{PED}(r)$. For example, in addition to reduce FOV, one can reduce echo spacing (ESP) (Wheeler-Kingshott et al., 2002). This can be achieved by increasing the readout EPI bandwith, acquiring data during the gradient ramps and segmenting k-space trajectory (Bammer et al., 2002). Also, further to adjusting the imaging parameters, repositioning the subject and reorienting the slice can decrease field inhomogeneity and render image more usable. For example, slices must been orthogonal to the cord to minimize partial volume

effect in axial imaging. Supporting the patient's head by a foam pads can reduce the natural curvature in the neck and hence the spinal cord be quasi-straight (Cohen-Adad and Wheeler-Kingshott, 2014).

In addition to optimizing the acquisitions parameters, spinal cord imaging quality has been shown to benefit from post-processing distortion correction techniques. Compared to brain imaging, few attempts and studies in neuroimaging applications have tailored and incorporated the use of these techniques in spinal cord imaging. There is a number of distortion correction techniques, most of them employ the distortion model derived in (Chang and Fitzpatrick, 1992), including co-registration, field map correction, point spread function (PSF), reversed gradient polarity method (RGP). In post-processing step, most of these techniques require an additional specific acquisition.

The first technique, *co-registration*, uses an anatomical reference image, typically a T_2-weighted acquisition. Applying non-linear registration, this technique warps the dMRI image onto the T_2-weighted image, which is much less affected by geometric distortions. The first step to registration generally consists in segmenting the ROI (here the spine) to estimate a non rigid deformation field. Comparing to others, this technique is advantageous as standard protocols generally contains by default a reference anatomical image. However, this way to correct distortion is difficult since the contrast and FOV of the anatomical and diffusion scans are quite different. To increase robustness to contrast changes, we generally use as a pixel-wise difference optimization metric the mutual information or cross-correlation between the two images (Andersson and Skare, 2010; Huang et al., 2008).

The second technique, *field map correction*, is popular and implemented in widely used softwares such as FSL[1]. This technique relies on a 2 minutes acquisition of the background magnetic field inhomogeneity, known as B_0 field map, usually based on the phase difference of a pair of conventional images (e.g. T_2-weighted) at two different echo times (Jezzard and Balaban, 1995; Reber et al., 1998). This map is in turn used to generate a warping field which will be applied to the EPI series. However, this field is exposed to large errors since it is sensitive to subject motion during acquisition. Furthermore, the phase maps are sensitive to high variation in the magnetic field. In this respect, several studies shown its impairments to correct distortion in several areas (Andersson et al., 2003; Holland et al., 2010).

Another technique is *point spread function* (PSF) mapping. An extra acquired scan is given by the convolution of the undistorted image with PSF of imaging system. PSF mapping provides information about intensity distribution and distortions for each voxel. Distortions due to susceptibility effects are quantified and corrected by considering the displacement field incorporated in the PSF. (Lundell et al., 2013) shown that this technique provides better anatomical consistency of fiber tractography in cervical spinal cord. However, this technique suffers from a relatively long acquisition time. PSF technique has been combined with parallel imaging and optimized for faster imaging (Zaitsev et al., 2004; Speck et al., 2008).

The last technique, commonly referred to as *reversed gradient polarity* (RGP), uses two EPI acquired with an opposite phase encoding direction - one head-feet and the other one feet-head (i.e., it is rotated 180°) for example, with the same FOV and matrix size (Chang and Fitzpatrick, 1992). According to Eqn 4.1, this inversion in PED causes a negative sign of $\Delta f(r)$. Thus, one can exploit the fact if two images were acquired with inverse polarity phase-encoding gradient, the corresponding displacement maps will have equal magnitude, but will be reversed from one image to another. The corrected image is therefore midway between the two distorted acquisitions. Some studies consider this technique as an alternative to *field map correction* as the field map here is estimated using an additional EPI. This last technique is distinctive by requiring only a quick additional EPI acquisition to correct distortion, just a few seconds. Furthermore, Cohen-Adad et

[1] https://fsl.fmrib.ox.ac.uk/fsl/fslwiki/FUGUE/Guide

al. shown its accurate estimation of both geometric and intensity distortion comparing to *PSF*, *field map* and *co-registration* (Cohen-Adad et al., 2009).

In this chapter, we focus on the use of this last technique, RGP, and we propose a comparative evaluation of post-processing techniques using this acquisition for correcting distortion. We first give an overview of the state-of-the-art methods we will evaluate. Then, we introduce a new geometric measure of alignment between the centerline of the spine and the reconstructed principal direction of diffusion. Finally, we compare these methods on a database of 95 subjects (29 controls and 66 MS patients) using the newly introduced measure of alignment, together with a comparison (cross-correlation) to the anatomical T2-weighted image. To the best of our knowledge, although these methods have already been benchmarked for brain MRI, this is the first time such a comparison is made for spine imaging.

4.2 Reversed gradient polarity technique

In this chapter, we focus on the comparative evaluation of field inhomogeneity-induced distortion correction methods using the RGP technique. More precisely we will compare 4 distortion correction methods: Block-Matching (BM) (Hedouin et al., 2017), Hyper-elastic Susceptibility artefact correction (HySCO) (Ruthotto et al., 2012), TOPUP (Andersson et al., 2003) and Voss (Voss et al., 2006). In this section, we give an overview of each of these methods.

4.2.1 Distortion model

A pair of spin-echo EPI are acquired in head-feet (HF) and feet-head (FH) phase encoding direction (PED), corresponding to the y-axis. Let I_F denote the forward gradient EPI image, acquired traversing k-space in the positive y-direction HF, and I_B (for backward) the oppositely-distorted reverse gradient image acquired traversing in the negative y-direction FH. The corrected image I_C is therefore midway between I_F and I_B. The problem is to find the deformation field from I_F (or equivalently from I_B) to I_C .

4.2.2 Method 1: Block-Matching

The block-matching (BM) strategy for field inhomogeneity-induced distortion in EPI (Hedouin et al., 2017) looks for a transformation by finding local correspondence between a small block (typically $3 \times 3 \times 3$ voxels) in the original and the target image (Ourselin et al., 2000; Commowick et al., 2012). The method follows the registration method introduced in (Avants et al., 2008) in which, instead of looking for a transformation $\mathbf{T}$ between two images, the transformation $\mathbf{T}^{1/2}$ is sought so that $I_B \circ \mathbf{T}^{-1/2}$ and $I_F \circ \mathbf{T}^{1/2}$ match as much as possible:

$$I_F \circ \mathbf{T}^{1/2} \approx I_B \circ \mathbf{T}^{-1/2} \approx \mathbf{I}_C \tag{4.2}$$

BM (Hedouin et al., 2017) adapts the approach to block matching algorithm presented by (Ourselin et al., 2000; Commowick et al., 2012) by constraining $\mathbf{T}^{1/2}$ to be aligned with the PED. The registration uses the cross-correlation metric as a measure of similarity. BM method is implemented and available in Anima[2], an open-source software for medical image processing.

[2] https://github.com/Inria-Visages/Anima-Public/

4.2.3 Method 2 : HySCO

The Hyper-elastic Susceptibility artefact COrrection method (HySCO) (Ruthotto et al., 2012; Macdonald and Ruthotto, 2016) is based on the physical distortion model derived in (Chang and Fitzpatrick, 1992). HySCO estimates the field inhomogeneity $b : \Omega \to \mathbb{R}$ by minimizing the following distance functional:

$$\mathcal{D}[b] = \frac{1}{2}\int_{\Omega} \Big(I_F(x+b(x)v)(1+v^{\top}\nabla b(x)) - I_B(x-b(x)v)(1-v^{\top}\nabla b(x))\Big)^2 dx \tag{4.3}$$

where v denotes the PED, $v = (0,1,0)^{\top}$, Ω the rectangular region of interest, $b(x)$ is the magnitude of the field inhomogeneity at $x \in \Omega$. Since this minimization is an ill-posed problem, HySCO considers a smoothness regularizer as following:

$$\mathcal{S}(b) = \frac{1}{2}\int_{\Omega} \|\nabla b(x)\|^2 dx \tag{4.4}$$

with imposing a constraint on the Jacobian determinant where $-1 \leq v^{\top}\nabla b(x)) \leq 1$ for almost all $x \in \Omega$ to ensure that the Jacobian determinants are strictly positive for both PEDs. Following Eqn. 4.3 and using the registration framework FAIR (Modersitzki, 2009), the field inhomogeneity is estimated by solving:

$$\min_{b\in\mathcal{B}} := \mathcal{D}[b] + \alpha\, \mathcal{S}[b] \tag{4.5}$$

where $\mathcal{B}$ denotes the closed ball and the parameter α balances between the regularity of the solution and minimization of the distance.

HySCO is implemented as a part of ACID [3] toolbox and integrated as a batch tool in the *Statistical Parametric Mapping* (SPM) [4] toolbox.

4.2.4 Method 3: TOPUP

An alternative application of RGP, called TOPUP, is proposed by (Andersson et al., 2003). TOPUP uses two images with opposite PEDs and estimates a transformation field which will be used to obtain the undistorted image I_C. Iteratively, TOPUP suggests a transformation field, calculates displacements maps, corrects I_F and I_B and evaluates the difference between both corrected images. TOPUP repeats these steps until the maximization of a computed similarity defined as the sum-of-squared differences between the corrected I_F and I_B. This similarity is a crucial bit because it allows TOPUP to estimate another transformation field using Gauss-Newton algorithm.

This distortion correction method is implemented on TOPUP algorithm, available within the FSL package [5]. Notice that when applying TOPUP algorithm on data, extreme slices of image volume are collapsed. We applied TOPUP with its default parameters except for resampling, we used Jacobian method.

4.2.5 Method 4: Voss

Voss et al (Voss et al., 2006) proposed a distortion correction method to reduce geometric and intensity distortions. For given image coordinates x and z, let denote $L_F^{x,z}(\cdot) = I_F(x,\cdot,z)$ be the intensity line (intensity profile) along the PED, y, for the forward image I_F. Similarly, we can

[3] http://www.diffusiontools.com/
[4] https://www.fil.ion.ucl.ac.uk/spm/
[5] https://fsl.fmrib.ox.ac.uk/fsl/fslwiki/topup

define $L_B^{x,z}$ for the backward image, I_B. The Voss method tries to find a transformation $U^{x,z}$ along the direction y to align the normalized cumulated intensity lines, defined as:

$$N_i^{x,z}(y) = \frac{1}{\alpha_i^{x,z}} \int_0^y L_i^{x,z}(y')dy' \qquad \text{for } i = F,B. \tag{4.6}$$

In the above, $\alpha_i^{x,z}$ is the normalization, defined as:

$$\alpha_i = \int_0^\infty L_i^{x,z}(y)dy \qquad \text{for } i = F,B \tag{4.7}$$

The cumulated intensity lines are then aligned by seeking a deformation $U^{x,z}$ such that

$$N_F^{x,z}(y + U^{x,z}(y)) = N_B^{x,z}(y - U^{x,z}(y)). \tag{4.8}$$

Note that this method realigns every line independently, so in order to increse the coherence between consecutive lines, a 3D Gaussian smoothing is applied to the deformation U.

This method, Voss algorithm, is available in Anima software. We used the method with default parameters in our comparison.

4.3 Geometric measure of alignment

In order to evaluate the impact of geometric distortion correction, we introduce in this section a measure of alignment between the geometry of the spine, represented by its centerline, and the principal direction of diffusion. In previous studies (Lundell et al., 2013; Voss et al., 2006; Cohen-Adad et al., 2009), one of the criterion used for the evaluation or the validation of distortion-correction was to use fiber tractography in the spine. We hypothesize that measuring the alignment of the diffusion direction and the spine geometry is an alternative, more direct way to evaluate the consistency between the diffusion anisotropy and the underlying image geometry.

The diffusion tensor model relates the local displacement of water molecules with the surrounding tissue microstructure. In the spinal cord white matter, it is mainly aligned with longitudinal fibers (Cohen-Adad et al., 2008b), which themselves follow a path parallel to the centerline of the spinal cord. We can therefore expect that the principal eigenvector of the diffusion tensor is locally aligned tangentially with the centerline of the spine. However, when the image is distorted, the apparent shape of the spine is affected, while the direction of the tensor is not. This results in a locally poorer alignment of the diffusion tensor with the spine. In what follows, we describe a method to measure how the diffusion tensors and the centerline of spinal cord align with each other.

4.3.1 Centerline extraction and modeling

We first segment the diffusion image to obtain a binary mask of the spinal cord (De Leener et al., 2014; De Leener et al., 2015). This segmentation is purely image-based, following the recommendation of the spinal cord toolbox (SCT), we computed the segmentation from the mean diffusion-weighted images. Using this binary mask of the spine, we compute the centerline in two steps: first, for every axial slice, we compute the barycenter of the mask within this slice; then we fit a degree-3 smoothing spline to the set of barycenters. This provides us with a continuous, differentiable representation of the centerline, from which we can compute the Frenet frame.

Let $\mathbf{x}(t) \in \mathbb{R}^3$ be a curve parametrized by $t \in \mathbb{R}^+$. Also, let $\mathbf{v}(\mathbf{t}) = \mathbf{x}(\mathbf{t})'$ denotes the velocity. We define the curvilinear abscissa s as:

$$s(t) = \int_0^t |\mathbf{x}'(\tau)| d\tau, \tag{4.9}$$

The Frenet frame at time t is defined as the orthogonal frame $(\mathbf{T}, \mathbf{N}, \mathbf{B})$ where $\mathbf{T}$ is the tangent, $\mathbf{N}$ is the normal and $\mathbf{B}$ is the binormal (see Figure.4.2).
The *tangent* unit vector $\mathbf{T}$ is defined as:

$$\mathbf{T} = \frac{d\mathbf{x}/ds}{\|d\mathbf{x}/ds\|} = \frac{\mathbf{x}'(\mathbf{t})}{\|\mathbf{x}'(\mathbf{t})\|} = \frac{\mathbf{v}(\mathbf{t})}{\|\mathbf{v}(\mathbf{t})\|}; \tag{4.10}$$

the *normal* unit vector $\mathbf{N}$ is defined as:

$$\mathbf{N} = \frac{d\mathbf{T}/ds}{\|d\mathbf{T}/ds\|} = \frac{\mathbf{T}'}{\|\mathbf{T}\|}; \tag{4.11}$$

the *binormal* unit vector $\mathbf{B}$ is defined as the cross product between $\mathbf{T}$ and $\mathbf{N}$:

$$\mathbf{B} = \frac{\mathbf{T} \times \mathbf{N}}{\|\mathbf{T} \times \mathbf{N}\|}. \tag{4.12}$$

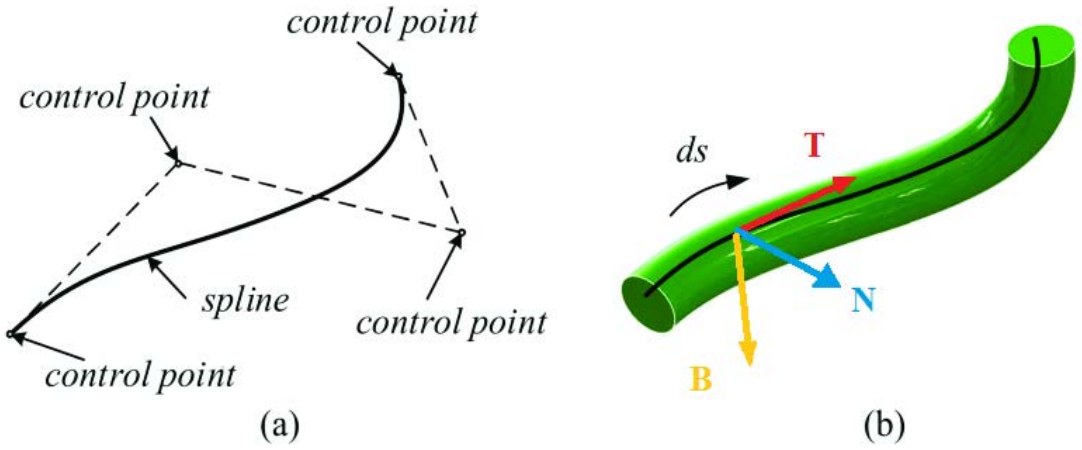

Figure 4.1: A spline model (a) and its Frenet frame (b). Image adapted from (Tang et al., 2018).

4.3.2 Measuring the alignment diffusion model within the cord

For every voxel at position $\mathbf{r}$ within the spinal cord, the binary mask, we first compute the the closest point $\mathbf{x}(t_0)$ to $\mathbf{r}$ along the centerline where t_0 is defined as follows:

$$t_0 = \arg\min_t \{||\mathbf{x}(t) - \mathbf{r}||\}. \tag{4.13}$$

Then we compute the coordinates of the principal eigenvector of the diffusion tensor, $\mathbf{e}_1(\mathbf{r})$, in the Frenet frame computed at $\mathbf{x}(t_0)$. In order to summarize the distribution of the principal eigenvectors $\mathbf{e}_1(\mathbf{r})$ within a region Ω, we compute the covariance matrix of these directions as follows:

$$\mathbf{M} = \frac{1}{\mathcal{V}(\Omega)} \int_\Omega \mathbf{e}_1(\mathbf{r}) \mathbf{e}_1(\mathbf{r})^\top d\mathbf{r} \tag{4.14}$$

where $\mathcal{V}(\Omega)$ is the volume of Ω. Intuitively, the matrix $\mathbf{M}$ will characterize the statistics of the angular deviation between the diffusion direction and the tangent to the centerline. From the eigendecomposition of the symmetric matrix, $\mathbf{M}$, we extract two statistics:

Mean angle direction (MAD) defined as the angle in degrees between the principal eigenvector of $\mathbf{M}$ and [1,0,0], which corresponds to $\overrightarrow{\mathbf{T}}$ in the Frenet frame

Angular concentration of directions (ACD) defined as the first eigenvalue of $\mathbf{M}$. Being the average of rank-1 non-negative symmetric matrices with eigenvalues (1,0,0), $\mathbf{M}$ has eigenvalues in the range of [0,1]. The more concentrated around the mean direction the closer to 1 is the ACD.

These statistics were computed for $\Omega \in \{\text{Brain stem, C1, } \ldots, \text{ C7, T1, T2}\}$ corresponding to every cervical and thoracic vertebral levels in the acquisition window.

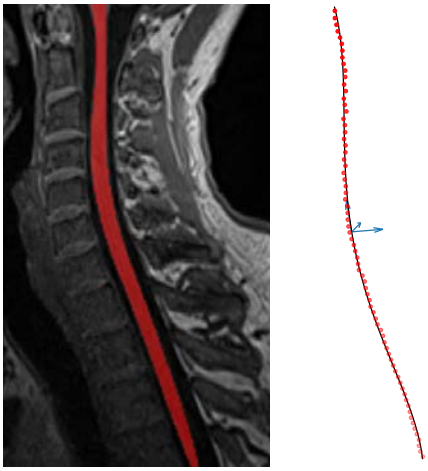

Figure 4.2: (left) T1 image with segmented spinal cord for reference; (right) barycenters of the spline mask (red dots), fitted centerline (black line) and the Frenet frame (blue arrows).

4.3.3 Centerline smoothing

When fitting the spline to the set of barycenters, we can control the smoothness of the fitted curve. In order to select the optimal smoothing parameters, we study its impact on the average MAD and ACD along the spine. We compare polynomial fitting and spline methods for fitting with several smoothing factors as shown in Figure. 4.3. This positive smoothing factor s used to choose the number of control points (knots) which in turn will be increased until a smoothing condition is satisfied. If $s = 0$, spline will interpolate through all data points.

4.4 Data acquisition

Data were acquired on 3T scanners at four sites in France: Marseille, Rennes, Strasbourg and Montpellier.

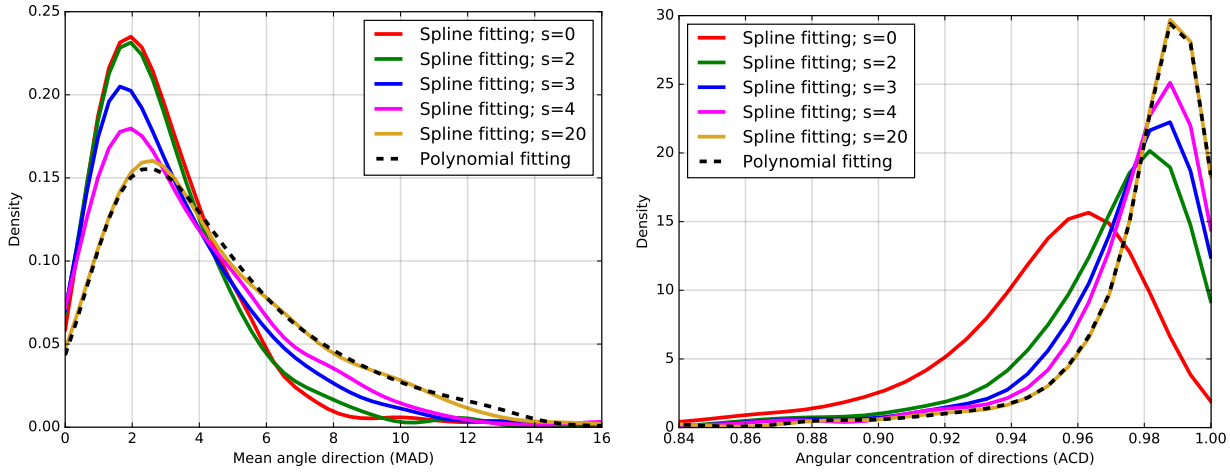

Figure 4.3: Distribution of mean angle directions (MAD) and angular concentration of directions (ACD) per vertebral level for cervical part (estimated with kernel density estimation).s is the smoothing factor.

4.4.1 Patients and healthy volunteers

29 healthy volunteers (mean age = 32.83±7.13, 18F/11M) and 66 MS patients (mean age = 32.20±6.30 ,42F/24M) were recruited in the study approved by the local research ethics committee. All participants provided informed written consent. Table. 4.1 illustrates more details about MRI scanner, centers and subjects characteristics.

Center	Marseille	Rennes	Strasbourg	Montpellier	**TOTAL**
3T Siemens MRI	Verio	Verio	Verio	Skyra	-
Volunteers	4	18	3	4	**29**
Gender	F/3M	10F/8M	3F	4F	**18F/11M**
MS Patients	7	44	8	7	**66**
Gender	4F/3M	28F/16M	5F/3M	5F/2M	**42F/24M**
					95 (60F/35M)

Table 4.1: Demographic information for all participating subjects, healthy volunteers and MS patients from several centers and total study cohort.

4.4.2 MRI data acquisition

Diffusion MRI

Images were acquired on 3T Siemens Verio and Skyra scanners (see Table 4.1 for the details). Thirty non-collinear diffusion-weighted images (DWI) were acquired at $b = 900$ s·mm^{-2}, six non-DWI ($b = 0$) measurements and one non-DWI ($b = 0$) with an opposite phase encoding direction (PED) were also acquired. This was repeated three times successively in order to increase the signal-noise ratio (SNR). Scans were performed in sagittal orientation and head-feet (HF) PED. The pulse sequence used for diffusion MRI is a single-shot Echo-planar imaging (ss-EPI) using parallel imaging (GRAPPA, acceleration factor 2). The reduced-FOV (field-of-view) technique was employed to reduce sensitivity of EPI to susceptibility artifacts. Sixteen slices were acquired with the following parameters without inter-slice gap: TR/TE = 3600/90 ms, with 2x2x2 mm^3 as

the resolution, and image matrix 80x80. The total acquisition time for the dMRI sequence was approximately 7 minutes.

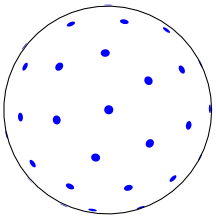

Figure 4.4: Gradient directions of diffusion MRI acquisition.

Anatomical reference MRI

The protocol also includes the following two high-resolution anatomical references:

T_1-weighted scan in sagittal orientation, magnetization-prepared rapid acquisition gradient echo (MPRAGE) sequence with an isotropic 1x1x1 mm^3 resolution, TR/TE = 1800/2.79 ms and FoV = 250 mm,

T_2-weighted scan in sagittal orientation, with anisotropic 0.7x0.7x2.75 mm^3 resolution, TR/TE = 3000/68.0 ms and Fov = 260 mm.

4.5 Methods

4.5.1 MRI Data pre-processing

Motion correction

dMRI data consist in a collection of several volumes ((6 b_0+30 DWI)x3) acquired during 7 minutes. In case of subject motion over the course of this acquisition, the collection of volumes have to be registered together. As it is often in anterior-posterior direction of the spinal cord, motion between DWI were corrected with allowing only slice-wise transformations in axial plane using SCT toolbox (Xu et al., 2013; De Leener et al., 2017). This way of realigning all volumes was shown to be more robust and accurate (Mohammadi et al., 2013).

Distortion correction

Then, dMRI data were corrected for susceptibility distortion using the cited four methods : Block-Matching (BM) available in Anima-Public, HySCO as implemented in SPM-ACID toolbox, TOPUP implemented in FSL package and Voss method implemented in Anima. We computed a displacement field using one non-DWI (b = 0) for each PED. Then, this field were applied on the whole of dMRI volume. We chose these two non-DWI (b = 0) carefully in such way they are close as possible in acquisition time to limit the effect of motion.

Segmentation of the cord and identification of vertebral level

Using SCT toolbox (De Leener et al., 2017), whole spinal cord segmentation was carried out on T_1-weighted, on T_2-weighted, on the mean of uncorrected DWI (b = 900 s·mm^{-2}) and on the mean of corrected DWI by each method. Then, we identify manually two vertebral levels, C3 and T1 as a requirement information for registering to PAM50 template.

4.5.2 Computing geometric metrics by vertebral level

Here, our aim is to compute statistics on geometric measures for each vertebral level. To do so, we register the PAM50 template (De Leener et al., 2018) and the T_1-weighted anatomical data and the mean diffusion-weighted image. Firstly, T_1-weighted anatomical data were registered to the PAM50 spinal cord template (De Leener et al., 2018). This generates forward and inverse warping fields from one to the other. Next, we register the PAM50-T1 template (De Leener et al., 2018) to the mean DWI using the inverse warping field from the previous step as an initial warping field. Here, we preferred to use T_1-weighted image rather than the T_2-weighted since the former has isotropic resolution, which makes the registration more effective. Alignment with the template provides robust definition of the inter-vertebral levels for the spine. This enables computation of the average metrics in spinal cord using the atlas-based approach introduced in (Lévy et al., 2015). As a result, we can quantify diffusion-based metrics averaged for each inter-vertebral level from C1 to T2. The processing pipeline is summarized in Figure. 4.5.

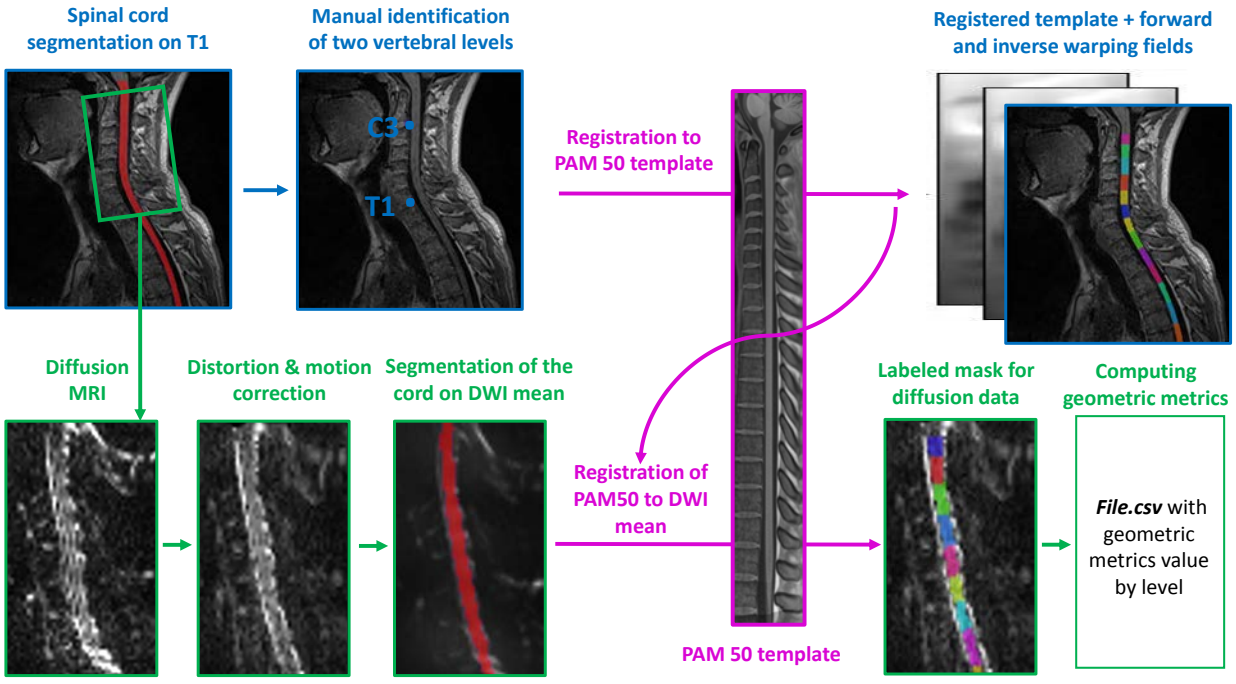

Figure 4.5: Illustration of the automated analysis pipeline. (1) Segmentation of the cord on T_1-weighted. (2) Manual identification of two vertebral levels. (3) Registration to the PAM50 template. (4) Motion and distortion correction of dMRI data. (5) Segmentation of the cord using DWI mean data. (6) Registration of PAM50-T1 registered to DWI mean data using the inverse warping field from previous registration as an initial warping field. (7) Computing MAD and ACD by vertebral level of the cervical part.

4.5.3 Computing cross-correlation and mutual information

Complementary to the geometric measure of alignment, we also compute the similarity between the corrected $b = 0$ image and the T_2-weighted image. Firstly, we rigidly registered T_2-weighted scan to the first $b = 0$ volume of the uncorrected and corrected dMRI scans. We then apply this rigid transform to the binary mask of the spinal cord obtained by segmenting T_2-weighted, which is now warped to the first $b = 0$ volume of the uncorrected and dMRI scans. Finally, we compute the cross-correlation (CC) and mutual information (MI) between the T2-weighted image and the $b = 0$ volume only within the spinal cord region.

Cross-correlation The cross-correlation, also referred to as Pearson correlation coefficient, is a measure of the linear correlation between two variables x and y. This coefficient has a value in $[-1, 1]$, where -1 and 1 are total negative and positive linear correlation respectively and 0 is no linear correlation. This coefficient is commonly represented by r_{xy} and defined as:

$$r_{xy} = \frac{\sum_{i=1}^{n}(x_i - x_m)(y_i - y_m)}{\sqrt{\sum_{i=1}^{n}(x_i - x_m)^2 \sum_{i=1}^{n}(y_i - y_m)^2}} \tag{4.15}$$

where n is the size of the mask in voxels, x_i and y_i are the intensities at voxel i of the T_2-weighted and dMRI images, x_m and y_m are their sample mean over the same ROI.

Mutual information The mutual information (MI) is a measure of the mutual dependence between two variables x and y. It quantifies the amount of information obtained about x through observing y. MI of x and y is given as:

$$MI(x,y) = \sum_{i=1}^{n}\sum_{i=1}^{n} p(x_i,y_i)\ log\left(\frac{p(x_i,y_i)}{p(x_i)p(y_i)}\right), \tag{4.16}$$

where $p(x,y)$ is the joint probability function of x and y, and $p(x)$ and $p(y)$ are the marginal probability distribution functions of x and y, respectively.

Preliminary version of this comparison Note that, there are some differences between the work we present in this chapter, and the preliminary versions we published in (Snoussi et al., 2019) and in (Snoussi et al., 2017). The first difference is the number of acquisitions, in (Snoussi et al., 2017) we compare the methods on a database of 69 subjects, in (Snoussi et al., 2019) on 95; in this chapter we use the same database as for the latter, but we removed 20 acquisitions after the quality check done on the registration of the binary mask to the first b=0 volume of dMRI data step, as described in paragraph 4.6.2. The second difference is in the processing pipeline. In this work and (Snoussi et al., 2017), we computed CC and MI within the rigidly registered mask of T_2-weighted to the first $b = 0$ volume of dMRI data. For (Snoussi et al., 2017), the registered mask was dilated by one voxel. However, in (Snoussi et al., 2019), CC and MI were computed within the overlap between the rigidly registered mask of T_2-weighted to first $b = 0$ volume of dMRI data and another binary mask obtained by segmenting mean DWI of dMRI data.

4.6 Quality Control

To ensure that the results are immune to image artefacts, and to identify problems during the processing pipelines, we performed a careful quality control (QC) on the raw data and after each

processing step. This is time-consuming process since it is mostly a manual procedure, and in our case the dataset consisted in more than 100 subjects, acquired several times (longitudinal follow-up at M0, M12, M24 and M36) with multiple image modalities. However, we believe it is a crucial step for the quality of the analysis and the accuracy of the results. In this section, we briefly describe the QC procedures in our pipeline.

4.6.1 Raw data

Size and volume For each subject, volunteer or patient, NIfTI files are organized into subfolders according to the different center names, acquisition dates and modalities. For each center, we used a uniform naming scheme for files and directories. We also checked whether all expected image modalities were present and had expected dimensions for each subject. For this part, we mainly used *medInira* (medical image processing and visualization software) [6] to visualize and choose the best image when an acquisition was repeated or redone. For diffusion MRI modality, we also checked whether both oppositely-phase encoding images, HF and FH, had the same affine matrix.

Conversion from DICOM to NIfTI In the conversion from DICOM to NIfTI format, one must also have access to the *b*-values and *b*-vectors, which correspond to the diffusion weighting factors and gradient directions.

Typically, it is common to have a mismatch between the orientation of the *b*-vectors and the image, which impacts the subsequent analysis of diffusion data. We compared using *dcm2nii* [7] and *mrconvert*, which is a part of MRtrix package [8], and manually checked that tensor orientation were consistent with the underlying spine structure. Figure 4.6 shows an example of the difference of tensors orientation between data converted by *dcm2nii* and *mrconvert* for the same image. We concluded that few tools are better suited for modern DICOM scans and using some classic tools is obsolete. Note that just recently some softwares as FSL noticed this important remark [9].

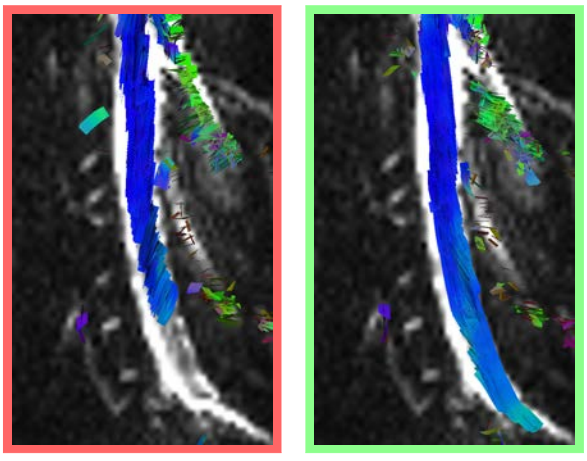

Figure 4.6: DICOM conversion influences DTI tensors orientation. Computed tractography superimposed on dMRI data converted by *dcm2nii* (left) and by *mrconvert* (right).

[6] https://med.inria.fr/
[7] https://www.nitrc.org/plugins/mwiki/index.php/dcm2nii:MainPage
[8] http://www.mrtrix.org/
[9] http://people.cas.sc.edu/rorden/mricron/dcm2nii.html

Ghosting data In order to not bias distortion correction comparison study, we did a QC to be sure that there is no artifacts related to motion or ghosting in the selected data. Note that RGP technique of distortion correction is not effective if original images are overly distorted. A quality check was performed in order to keep normal data and discard unusable data. Some examples of discarded data in this QC step are reported in Figure.4.7.

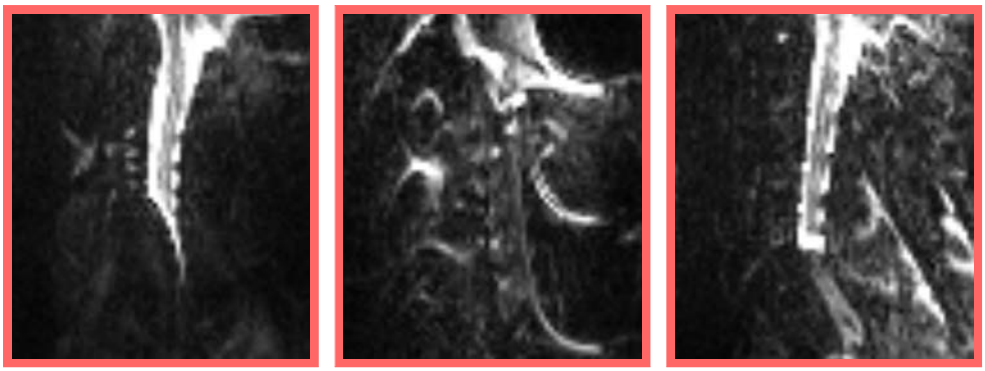

Figure 4.7: Examples of discarded data due to a problem during the acquisition related to motion or ghosting

4.6.2 Processing pipeline

Segmentation of spinal cord for anatomical images The propagated segmentation of the spine fails occasionally due to the presence of low contrast variations between the spinal cord and the surrounding cerebro-spinal fluid (CSF). Generated masks were reviewed by one rater (H.S.) and manual adjustments were made to correct some segmentation failures. Possible solutions to amend the generated masks include:

- smoothing the image along the centerline of the spinal cord to minimize leaking problems,
- providing a centerline binary mask with many points to ensure a correct orientation of the propagated segmentation
- adjusting other parameters.

In total, 7 T_1-weighted images out of 95, 6 T_2-weighted images out of from 95 and approximately 135 dMRI out of 95×5 were adjusted. Figure 4.8 illustrates some failed segmentation before and after adjusting.

Labeling of T_1-weighted and template registration For registering the data to the template, the manual localization of two vertebral levels is required. In the *Spinal Cord Toolbox* (SCT), there are two ways for generating the cord segmentation labeled with vertebral level. The first way is fast and automatic but fails occasionally as shown in Figure. 4.9. The second way is by selecting manually two referring labels using a viewer. Although it is more time-consuming, we followed the latter procedure then we checked and reviewed visually all labeling masks by one rater (H.S).

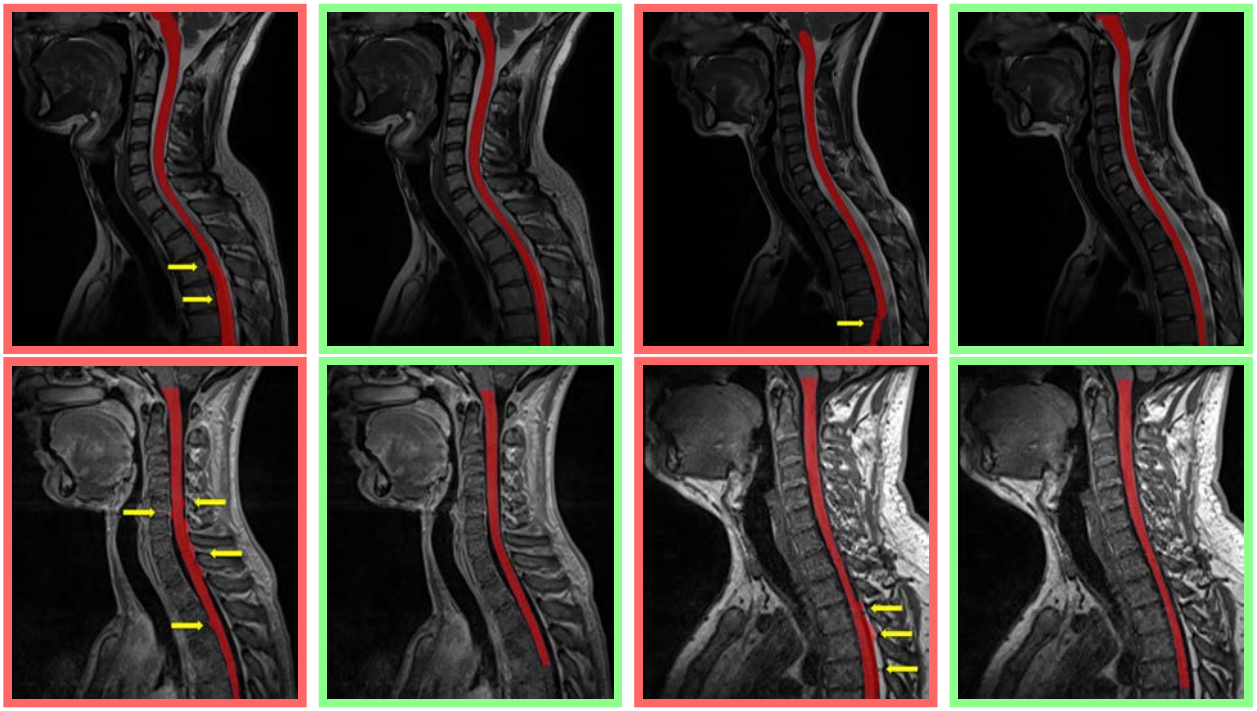

Figure 4.8: Examples of failures in segmentation (red box) and the result after changes (green box) for T_2-weighted images (first line), and for T_1-weighted images (second line).

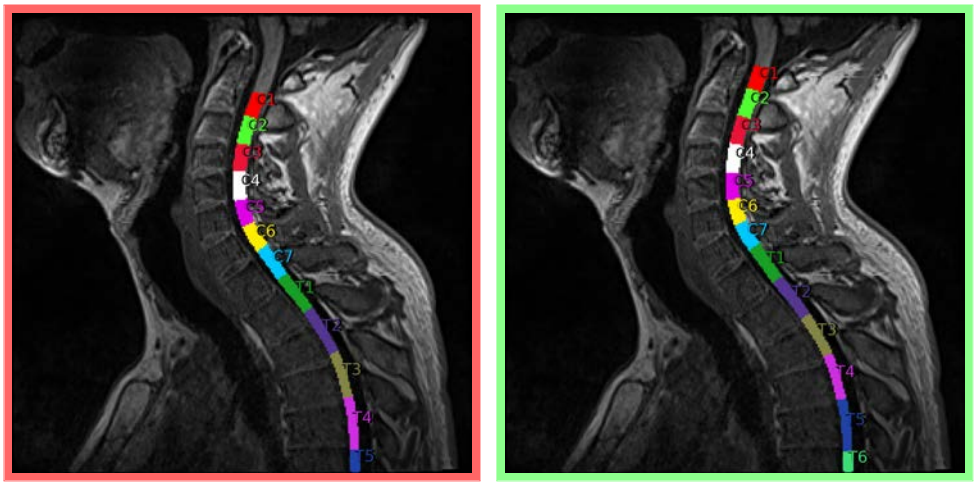

Figure 4.9: Checking of labeling

Registration of mask T_2-weighted to diffusion image Quality of the registration of the binary mask obtained from T_2-weighted to the first $b = 0$ volume were checked by visual inspection. After this step of QC, we only kept out of 95 dMRI data for computing cross-correlation and mutual information.

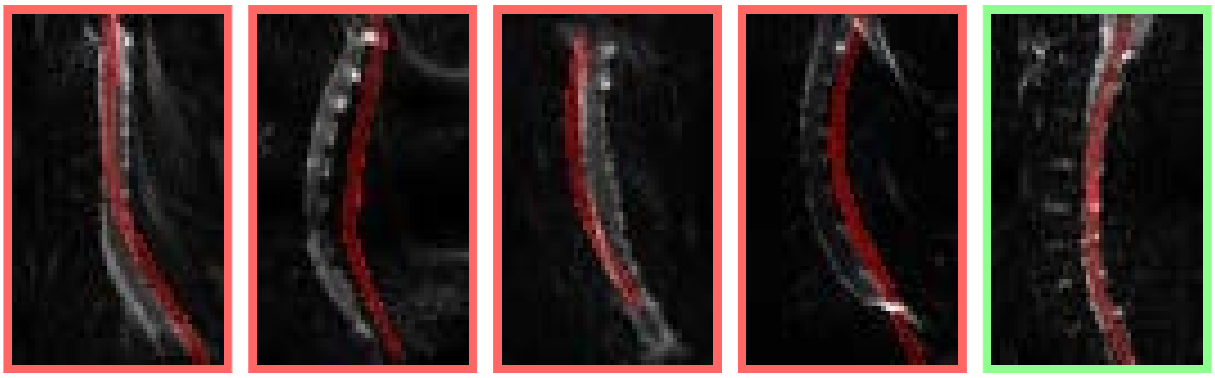

Figure 4.10: Examples of $b = 0$ volume corrected by various methods; the mask of the spinal cord computed using T_2-weighted and registered to diffusion image is overlaid. Failed and effective registration are in red and green box respectively.

4.7 Results

4.7.1 Geometric statistics

For every distortion correction method, geometric statistics were computed for every cervical and thoracic levels in the acquisition window. Results of mean and standard deviation of each metric, MAD and ACD, for brain stem (BS) and each vertebral level are presented in tables 4.2 and 4.3. Paired Tukey test was computed to compare the performance of each method to the non-corrected dMRI. For colors in tables, dark green means that p-value shows significant improvement and inferior to 10^{-3}, weak green means that p-value shows significant improvement but $10^{-3} <$ p-value $< 5.10^{-2}$, dark red means that p-value shows significant deterioration and inferior to 10^{-3}, and weak red means that p-value shows significant deterioration but $10^{-3} <$ p-value $< 5.10^{-2}$.

Mean Angle Direction (MAD)

	Block-Matching		**HySCO**		**TOPUP**		**Voss**		**Uncorrected**	
Levels	Mean	STD	Mean	STD	Mean	STD	Mean	STD	Mean	STD
BS	4.50	3.59	4.86	3.48	5.58	4.61	4.61	3.76	5.04	3.94
C1	4.18	5.75	3.83	3.89	3.84	2.39	3.58	2.89	4.06	2.83
C2	3.07	1.98	2.90	2.04	2.82	1.70	2.71	2.01	2.36	1.44
C3	2.39	1.64	2.44	1.55	2.74	1.75	2.41	1.56	2.71	1.61
C4	2.34	1.91	2.49	1.82	2.96	1.81	2.41	1.63	2.56	1.71
C5	2.39	1.61	2.93	2.29	3.34	2.13	2.89	1.77	2.58	1.44
C6	2.96	2.10	3.06	2.04	3.55	2.16	3.07	2.26	3.13	2.13
C7	3.25	2.82	3.77	3.83	3.89	3.50	3.62	4.08	3.78	3.21
T1	4.31	4.40	4.42	4.25	5.32	7.59	6.36	6.20	5.19	4.64
T2	11.31	10.72	10.68	10.05	16.22	17.43	15.26	12.28	14.19	14.76

Table 4.2: Mean and standard deviation for Mean Angle Direction (MAD) metric for data corrected by Block-Matching, HySCO, TOPUP and Voss and uncorrected data. Weak green means that p-value shows significant improvement with $10^{-3} <$ p-value $< 5.10^{-2}$, weak red means that p-value shows significant deterioration. BS: brain stem.

Angular Concentration of directions (ACD)										
	Block-Matching		**HySCO**		**TOPUP**		**Voss**		**Uncorrected**	
Levels	Mean	STD	Mean	STD	Mean	STD	Mean	STD	Mean	STD
BS	84.32	8.66	82.06	8.57	78.10	9.46	84.96	8.01	80.22	8.71
C1	96.49	4.96	95.93	4.56	95.60	5.84	96.06	3.92	95.10	5.76
C2	97.75	2.14	97.23	2.29	97.68	2.20	97.57	2.21	97.25	2.55
C3	97.91	2.08	97.80	2.01	97.82	1.89	97.83	2.23	97.71	2.23
C4	97.73	2.34	97.77	1.82	97.59	2.33	97.93	1.57	97.83	1.69
C5	97.62	1.68	97.35	2.06	97.83	1.64	97.76	1.44	97.48	1.63
C6	96.08	4.03	95.80	3.75	96.53	3.56	96.57	3.19	96.02	3.31
C7	94.63	6.17	93.69	6.52	94.84	7.44	95.03	5.05	94.32	6.08
T1	93.09	7.92	91.37	7.49	91.88	9.17	91.61	7.70	89.99	9.58
T2	83.56	12.66	80.23	14.47	85.00	13.99	84.67	11.40	77.59	16.15

Table 4.3: Mean and standard deviation **multiplied by 10^2** for ACD metric for data corrected by Block-Matching, HySCO, TOPUP and Voss and uncorrected data. Dark green means that p-value shows significant improvement with p-value $< 10^{-3}$, weak green means that p-value shows also significant improvement but $10^{-3} <$ p-value $< 5.10^{-2}$. BS: brain stem.

Figure.4.11 shows the MAD and ACD by vertebral level. This way of representation shows that extreme vertebral level of the acquisition window are more affected by distortion. Note that for MAD, a decrease is considered as an improvement (less bias in the direction), while for ACD, an increase is considered as an improvement (higher concentration around the mean direction).

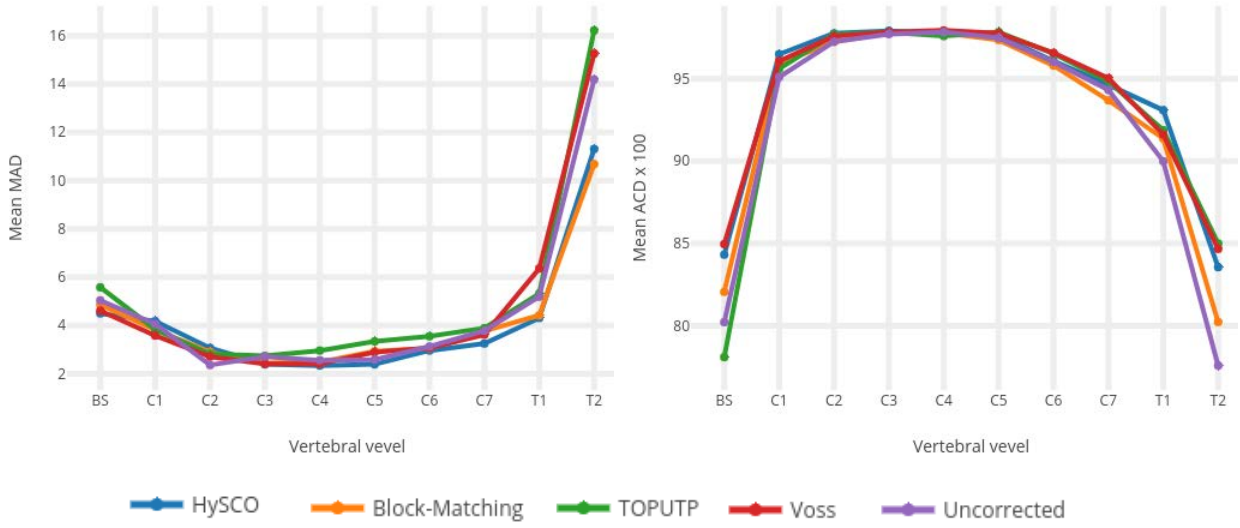

Figure 4.11: Mean MAD (in degree) and mean ACD ($\times$ 100) by vertebral level. This way of representation shows that extreme vertebral level of the acquisition window are more affected by distortion.

4.7.2 Comparison with anatomical images

Since T_2-weighted image is not affected by distortion, it can be considered as a gold-standard for the evaluation of distortion correction. So, we also compare the corrected volume ($b = 0$) of dMRI data by each method to the T_2-weighted image. We report results of cross-correlation and

mutual information. Note that results presented here are slightly different to the study reported in (Snoussi et al., 2017) because of difference in pipeline treatment and dataset ($N = 69$ *vs.* $N = 75$).

Cross-correlation study

A Paired Tukey test was performed on the cross-correlation scores and reported in Table. 4.4. In Figure.4.12 results are reported using box plots.

Cross-correlation					
Methods	BM	HySCO	TOPUP	Voss	Uncorrected
Mean	0.185	0.242	0.179	0.148	0.160
STD	0.114	0.119	0.150	0.115	0.107
P-value	0.029	2.10^{-4}	0.189	0.173	-
t-statistic	2.215	7.303	1.325	-1.375	-

Table 4.4: Paired Tukey test for Block-Matching, HySCO, TOPUP and Voss for Cross-correlation for the whole of the spinal cord region. Dark green means that p-value shows significant improvement and inferior to 10^{-3}, weak green means that p-value shows significant improvement but $10^{-3} <$ p-value $< 5.10^{-2}$.

Mutual information study

A Paired Tukey test was performed also on the mutual information scores and reported in Table. 4.5. In Figure.4.12 results in boxplot format.

Mutual information					
Methods	BM	HySCO	TOPUP	Voss	Uncorrected
Mean	0.304	0.330	0.312	0.293	0.277
STD	0.051	0.049	0.064	0.053	0.054
P-value	10^{-5}	4.10^{-14}	6.10^{-7}	9.10^{-4}	-
t-statistic	4.652	9.198	5.433	3.449	-

Table 4.5: Paired Tukey test for Block-Matching, HySCO, TOPUP and Voss for Mutual information for the whole of the spinal cord region. Dark green means that p-value shows significant improvement and inferior to 10^{-3}, weak green means that p-value shows significant improvement but $10^{-3} <$ p-value $< 5.10^{-2}$.

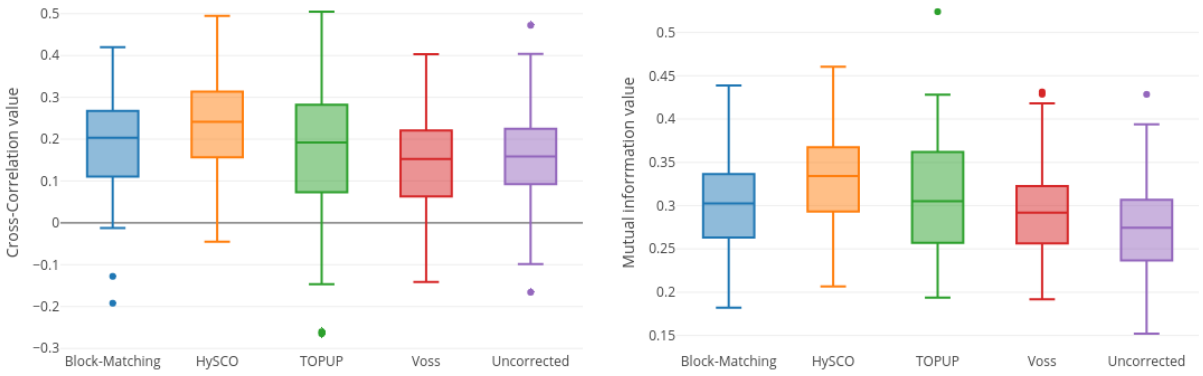

Figure 4.12: Boxplots graphics of cross-correlation (left) and mutual information (right) between T2 and corrected b=0 diffusion images.

4.7.3 Vertebral level volume

Further more, we computed the volume in mm^3 of each vertebral level for uncorrected and corrected data as shown in Table. 4.6. This table contains also results of paired Tukey test to compare the volume of each method to the non-corrected dMRI. This will be useful to study the effect of these distortion methods on the volume vertebral level and also to have an idea about the quantity of region in which we apply our geometric metrics.

	BM		HySCO		TOPUP		Voss		Uncorrected	
Level	Mean	STD	Mean	STD	Mean	STD	Mean	STD	Mean	STD
C1	560.5	123	583.9	106	555.9	118	555.8	110	568.7	104
C2	530.7	118	552.0	101	528.7	123	526.8	103	538.7	108
C3	913.2	155	967.6	165	911.5	173	934.8	146	917.8	155
C4	959.8	157	1021	163	923.0	175	949.4	142	943.4	152
C5	855.4	158	901.6	150	823.3	170	837.3	143	835.5	150
C6	777.3	137	810.8	126	725.1	161	753.7	141	749.6	134
C7	743.6	127	764.4	120	681.7	134	710.4	132	732.6	127
T1	790.4	138	820.9	153	722.3	158	742.8	173	757.6	158
T2	456.9	277	501.0	283	363.7	265	339.5	283	397.9	271

Table 4.6: Volume of every vertebral level (in mm^3) of spinal cord, segmented mask, corrected by Block-Matching, HySCO, TOPUP, Voss and uncorrected. Dark red means that p-value shows significant difference and inferior to 10^{-3}, weak red means that p-value shows significant difference but $10^{-3} <$ p-value $< 5.10^{-2}$.

4.8 Discussion and conclusion

In this Chapter we have proposed a novel geometric based metrics and framework for studying the impact of distortion correction in diffusion MRI of the spinal cord. We showed a difference in geometric alignment after correcting with one method or another.

For Block-Matching method, as shown in Table. 4.2, we can remark that it performs significantly better in T1 vertebral levels. However, there is a significant deterioration in C2 as HySCO. For ACD metric, BM improves the concentration significantly in brain stem region, C1, C2, T1 and T2.

For HySCO method, as shown in Table. 4.2, for MAD metric we can observe that it performs significantly better than uncorrected in T1 and T2 vertebral levels. But, this method has significant deterioration at C2 vertebral level, as BM, but mean MAD of HySCO is more close the uncorrected. For ACD metric, we remark a significant improvement at edges of the spinal cord (brain stem, C1, C7 and T1 regions) as shown in Table. 4.3.

For TOPUP method, we consider significant deterioration in MAD in C2 and C5 vertebral levels without any significant improvement. For ACD metric, there is significant improvement at C2, C5, C6 and T2 vertebral levels.

For Voss method, there is a significant improvement in MAD metric for C1 vertebral level and significant deterioration in T1 vertebral level. But, there is a very remarkable amelioration for ACD in all vertebral levels, except C3 and C4 which are in the middle of the field-of-view of the acquisition.

Complementary to the geometric measure of alignment, we also compute the similarity between the corrected $b = 0$ image and the T_2-weighted image. For cross-correlation, there is a significant amelioration only for Block-Matching and HySCO as demonstrated in Table. 4.4. For mutual information, there is a significant amelioration for all methods as shown in Table. 4.5.

Further more, we computed the volume in mm^3 of each vertebral level for uncorrected and corrected data as shown in Table. 4.6. A paired Tukey's test was performed in the mean of volume of each vertebral level of dMRI corrected and uncorrected. We consider that all methods have a remarkable significant impact on the volume in mm^3. For Voss there is significant decrease of volume for C1, C7 and T1. For TOPUP, there is also significant decrease of volume in C7 and T1. For HySCO there is a significant increase of all vertebral level volume except C2. For BM, there is a significant increase in vertebral level volume for C6, T1 and T2. Causes of these results may be related to the re-sampling step necessary after unwarping. These significant difference of volume may affect and reorient such analysis as they include new voxels/new information in vertebral level.

Otherwise, a clinically useful details to note that the mean time per subject is about 2 seconds for HySCO algorithm, 5 seconds for Voss algorithm, 170 seconds for Block-Matching algorithm (multi-threaded) and 500 seconds for TOPUP algorithm. These mean times were obtained on an Intel CORE i7.

The novel statistics we propose, based on the quantifying the alignment of diffusion directions with the spine macroscopic structure, provide a new light to the evaluation of distortion correction methods. Based on the assumption that the distortion only affects the apparent shape of spine and not the direction of tensor, we proposed two novel statistics which take into account the alignment of the diffusion tensor with the apparent centerline of the spinal cord. This geometric evaluation was used to compare four distortion correction methods conducted on 95 scans. The fragmentation by levels of the spine shows the different impact of distortion between edges (C1, C2, T1, T2) and center (C3,C4) of the imaging window. This local evaluation provides a performance measure complementary to classical comparison with a reference anatomical image. We can also report per-level statistics, and provide a measure different and complementary to the comparison with an anatomical reference image. This idea of metric is only relevant to spinal cord as it has a simple apparent geometry.

One conclusion when considering these results is that these methods of distortion correction have different impact on the raw data. This difference confirm the necessity to do such study for

comparing and evaluating with more details these results. In addition, we show that the impact of each method affect the characterization of the angular deviation between the diffusion direction and the tangent to the centerline. Therefore, the choice of such method is crucial step in a pipeline analysis. Furthermore, a possible next step could be to introduce these geometric metric in the method of distortion correction as a registration or convergence criterion.

In our work, using diffusion MRI acquired in sagittal way with Head-Feet (HF-FH) PED, we show that distortion is limited only for extremes of FOV, especially those in PED. The extremes of FOV in HF-FH contain brain stem, C1, C2 and C7, T1 and T2. However, acquisition in Anterior-Posterior (AP-PA) PED, the extremes of FOV will be empty but the acquisition will may be hampered by more distortion as result of perpendicular inhomogeneity field depending the size of matrix. One interest perpective of our work is to apply the current evaluation of distortion correction and compare between them.

Chapter 5

Characterization of Multiple Sclerosis Abnormalities within the Cervical Spinal Cord

Contents

5.1 Introduction

Spinal cord is a clinically common and eloquent structure frequently involved in MS. Spinal cord lesions in MS patients are frequent in the cervical part, commonly restricted to two vertebral levels in length, fill less than half of the cross sectional area of the spinal cord and generally peripheral (Stroman et al., 2014). In clinical practice, conventional MRI (including T_2-weighted and T_1-weighted scans) of the brain and spine is increasingly used and integrated as a new criteria in the diagnosis and follow-up of MS patients (Amélie et al., 2015). It has a huge impact on this disease by enabling an earlier diagnosis, an a precise follow-up of the evolution of lesions in patients. However, despite its growing role in scientific and clinical investigation of MS, conventional MR images show little correlation with histological findings and clinical disability of the MS patients (Barkhof, 2002). In addition, some regions in white matter appear normal using conventional MRI while they are involved in the MS process (Miller et al., 1998; Filippi and Grossman, 2002; Rovaris et al., 2006). This suggests that conventional MRI has a relatively low specificity with respect to MS pathology and low sensitivity to diffuse tissue injury in normal-appearing white matter (NAWM). In this context, the development of quantitative MRI, and in particular diffusion MRI (dMRI), has recently shown its potential to provide intrinsic and normative value to tissue properties useful for diagnosis, prognosis and ultimately clinical trials in MS. MS has benefit mostly from advanced quantitative spinal cord MRI such as fMRI, MTR and dMRI (Agosta et al., 2007a; Inglese and Bester, 2010).

While in general brain MRI has received detailed attention over the past years, the interest for quantitative MRI of the spine is relatively recent. One of the challenges of analyzing diffusion MRI data is that it is multivariate in nature. This requires the use of statistical tools adapted to this kind of data. In this chapter, we propose a pipeline to extract average dMRI metrics per vertebral level, and we perform a statistical analysis to show their changes associated with the presence and evolution of MS lesions within the same vertebral level. The pipeline is generic in nature, and it is applied to metrics extracted from the diffusion tensor and the ball-and-stick models (Behrens et al., 2003).

5.2 Quantifying metrics in the spinal cord

WM in the spinal cord is organized into myelinated axon bundles that ensure adequate communication between the peripheral and the central nervous system. The cord is divided into four different parts: the cervical, thoracic, lumbar and sacral parts. Each part is also divided into several vertebral levels. For MS patients, a damage caused to a spinal pathway can lead to neuropathic pain or motor and sensory deficits. Given that each spinal axon bundle is associated to specific functions, the diagnosis or promotion of functional recovery depends on the type, the extent and location of the damaged pathways. The first methodological question for a group-based statistical analysis is how to define a common spatial reference across subjects.

In this section, we discuss three possible choices: either using manual-drawn regions of interest (ROI), identifying major tracts using tractography or using an atlas. In what follows, we present the details of each solution and we summarize the comparison of these in Table. 5.1

5.2.1 ROI-based approach

A region of interest (ROI), defined as a binary mask, can be manually drawn by selecting voxels on each axial slice in an MR image by an anatomical expert. In parallel, one can improve the gray/white matter separation using automated segmentation methods (Ellingson et al., 2007a).

From this, metrics averaged within each ROI can be computed to report values specific to a given tract or region. Although this is a standard method in neuroimaging (Ciccarelli et al., 2007; Cohen-Adad et al., 2008a; Onu et al., 2010), ROI-based approach has several limitations: (i) very time-consuming, in particular for large populations, (ii) the definition of a specific axon bundles is biased by the anatomy knowledge of the expert, (iii) ROIs masks don't compensate for partial volume effect (PVE) with surrounding gray matter and CSF, which is a problem for low spatial resolution typical in dMRI.

5.2.2 Tractography-based approach

Tractography is a 3D representation of the WM fiber architecture reconstructed using dMRI data. By following the principal directions of diffusion reconstructed locally, it artificially connects neighboring voxels with coherent principal diffusion direction. Performing the tractography in the spinal cord facilitates retrieving and tracking major axon bundles and longitudinal pathways (Wheeler-Kingshott et al., 2002; Ciccarelli et al., 2007; Ellingson et al., 2007b). Once the fiber bundles are reconstructed, diffusion MRI metrics can be quantified within voxels that include specific segment or tract (Van Hecke et al., 2008). Several tractography methods have been proposed differences mainly in the adjacent information used to estimate and reconstruct posterior trajectory (Mori and Van Zijl, 2002). Various implementations of tractography algorithms are available in software packages such as TrackVis [1], Camino (Cook et al., 2006) or medInria [2]. Tractography is a semi-automatic procedure, and therefore offers the potential to reduce user bias when compared to the ROI-based approach described in section 5.2.1. However, there is a number of challenges to tractography in the spinal cord.

First, in order to quantify metrics specific to WM, white and gray matter must be segmented prior to tractography using the diffusion MRI data (Ellingson et al., 2007a). Besides, tractography is sensitive to the geometric distortions, and the reconstructed tracts may terminate prematurely as an effect of the distortion. In addition, pathological changes in MS may lead to increased water mobility and decrease anisotropy in WM (Song et al., 2005), which can cause an interruption or a discontinuity of the reconstructed WM fibers at the site of an MS lesion. Last, to improve tractography, it is generally recommended to acquire images with isotropic resolution (Caan, 2016). In these images, the small cross-sectional of the cord implies PVE with the surrounding CSF, GM and the non-longitudinal branches in GM and through spinal segments, which contributes in reducing the specificity of the estimated principal directions of diffusion.

5.2.3 Atlas-based approach

This approach consists in registering the subject's spinal cord to a template, where ROIs have been manually labelled, in order to quantify metrics specific to each ROI. For spinal cord, a template was created (Fonov et al., 2014; Leener et al., 2018) with an anatomical labelling to extract per-ROI average metrics using partial volume correction (Lévy et al., 2015). The principal motivation for using this approach is to provide an automated framework to defined a common spatial reference for quantifying MRI data within spinal cord pathways.

This approach solves many issues existing in ROI and tractography approaches. The atlas is aligned with PAM50 template (Fonov et al., 2014) which is a symmetric and straight anatomical template of the spinal cord that involves vertebral levels from C1 to T6 and has isotropic resolution (0.5 mm). Thus, after registration of the dMRI data to the template, the warping field is applied to

[1] http://trackvis.org/
[2] https://med.inria.fr/

white matter atlas which is in turn aligned in native space with the spinal cord of the subject. The intensity value of each voxel in the WM atlas represents the fractional volume (in the range $[0, 1]$) of a specific tract, normalized by the probability to be in the WM (Taso et al., 2014). Therefore, during metric extraction partial volume effect is accounted for using Gaussian mixture models. Also, this approach facilitates multi-center and longitudinal studies. We would like to thank the authors of (Lévy et al., 2015) and developers of the spinal cord toolbox for the discussions and their help in optimizing the pipeline.

ROI-based approach	
⊕ Better control (accuracy increase) ⊕ Adapted to axial acquisition	⊖ Manual procedure : time consuming ⊖ Manual delineation bias ⊖ PVE not accounted ⊖ Large bias on small tract
Tractography-based approach	
⊕ Semi-automatic procedure: fast ⊕ Relative lower user bias ⊕ Typically isotropic resolution and sagittal acquisition (Already in EMISEP protocol)	⊖ Sensible to susceptibility distortions ⊖ Not applicable with gapped slices ⊖ PVE not accounted
Atlas-based approach	
⊕ Free from manual delineation bias ⊕ PVE accounted during metric extraction ⊕ Less sensibility to susceptibility distortions ⊕ Higher accuracy and precision for L/R CST comparing to ROI-based	⊖ In the process of discovering them...

Table 5.1: Quantification of dMRI metrics approaches. PVE: Partial volume effect, CST: corticospinal tract

5.3 Data acquisition

Data were acquired on 3T scanners at four sites in France: Marseille, Rennes, Strasbourg and Montpellier.

5.3.1 Multiple sclerosis patients and healthy volunteers

29 healthy volunteers (mean age = 32.83±7.13, 18F/11M) and 66 MS patients (mean age = 32.20±6.30 ,42F/24M) were recruited in the study approved by the local research ethics committee. All participants provided informed written consent. Healthy volunteers and MS patients are from 4 hospitals in France: Marseille, Rennes, Strasbourg and Montpellier. Details about MRI scanners, centers and subjects characteristics are reported on Table. 5.2.

Center	Marseille	Rennes	Strasbourg	Montpellier	**TOTAL**
3T Siemens MRI	Verio	Verio	Verio	Skyra	-
Volunteers	4	18	3	4	**29**
Gender	F/3M	10F/8M	3F	4F	**18F/11M**
Mean age(year)	34.0±4.74	32.61±7.97	34.67±5.25	31.25±5.67	32.83±7.13
Mean weight(kg)	72.5 ± 6.7	65.4 ± 11.4	65.0 ± 7.5	56.0 ± 4.1	65.0 ± 10.7
Mean size(m)	1.75 ± 0.03	1.72 ± 0.09	1.66 ± 0.06	1.64 ± 0.04	1.71 ± 0.08
MS Patients	7	44	8	7	**66**
Gender	4F/3M	28F/16M	5F/3M	5F/2M	**42F/24M**
Mean age(year)	32.57±8.30	31.43±6.14	34.0±5.29	34.57±4.78	32.20±6.30
Mean weight(kg)	72.3 ± 11.6	70.9 ± 16.3	67.2 ± 7.7	69.1 ± 13.6	70.4 ± 14.8
Mean size(m)	1.70 ± 0.09	1.70 ± 0.10	1.70 ± 0.09	1.68 ± 0.06	1.70 ± 0.09
					95 (60F/35M)

Table 5.2: Demographic and clinical information for all participating subjects, healthy volunteers and MS patients in the EMISEP cohort.

5.3.2 MRI Acquisition

Scans were acquired on Siemens 3T MRI scanners (Verio and Skyra). We give a brief presentation of each MR modality we processed in what follows.

Diffusion MRI

Thirty diffusion-weighted images (DWI) were acquired at $b = 900$ s·mm^{-2} with non-collinear gradient directions, six non-DWI ($b = 0$) measurements and one non-DWI ($b = 0$) with an opposite phase encoding direction (PED) were also acquired. This was repeated three times successively in order to increase the signal-noise ratio (SNR). Scans were performed in sagittal orientation and head-feet (HF) PED. The pulse sequence used for diffusion MRI is a single-shot echo-planar imaging (ss-EPI) using parallel imaging (GRAPPA, acceleration factor 2). The reduced-FOV (field-of-view) technique was employed to reduce sensitivity of EPI to susceptibility artifacts. Sixteen slices were acquired with the following parameters without inter-slice gap: TR/TE = 3600/90 ms, with $2 \times 2 \times 2$ mm^3 as the resolution, and image matrix 80×80. The total acquisition time for the dMRI sequence was approximately 7 minutes.

Anatomical reference MRI

The protocol also includes two high-resolution anatomical references:

T_1-weighted scan in sagittal orientation, magnetization-prepared rapid acquisition gradient echo (MPRAGE) sequence with an isotropic $1 \times 1 \times 1$ mm^3 resolution, TR/TE = 1800/2.79 ms and FoV = 250 mm

T_2-weighted scan in sagittal orientation, with anisotropic $0.7 \times 0.7 \times 2.75$ mm^3 resolution, TR/TE = 3000/68.0 ms and Fov = 260 mm

In addition to T_2-weighted scan, other modality was acquired for segmentation of MS lesions: sagittal T_2*-weighted.

5.3.3 Segmentation of MS lesion

For 53 MS patients (out of the 66), the MS lesions were segmented manually by 9 neurological expert, as described in (Eden et al., 2019). In brief, lesion were segmented manually using both axial T_2 and sagittal T_2*-weighted by 9 raters including radiologists and experienced readers using ITK-SNAP Toolbox v3.6.0. From these segmentations, we computed for each vertebral level:

- the number of MS lesions within the vertebral level,
- the total volume of lesions, normalized by the volume of the vertebral level.

We report on Figure.5.1 the histogram of volume lesions, for the range of cervical levels [C1-C7] and [C2-C4], respectively.

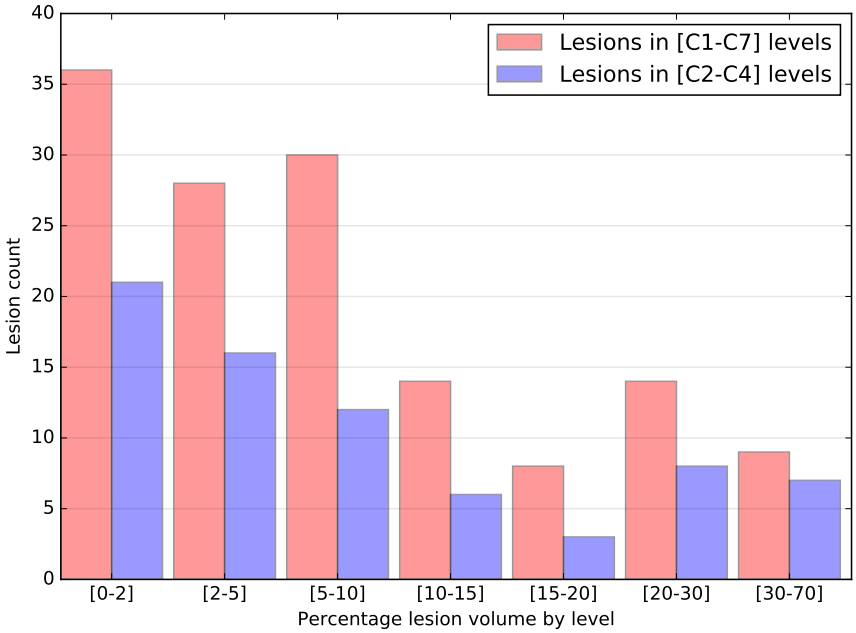

Figure 5.1: Distribution of lesion's volume in [C1-C7] and [C2-C4] regions.

5.4 Methods

5.4.1 MRI Data pre-processing

In this section, we present the processing pipeline, from the raw images to extracted diffusion measures per subject and per vertebral level. The whole processing pipeline is depicted on Figure.5.2.

Motion and distortion correction

Motion between DWI were corrected using the method presented in (Xu et al., 2013) and implemented in the Spinal Cord Toolbox (SCT). Then, dMRI data were corrected for susceptibility distortion using HySCO (Hyperelastic Susceptibility Artefact Correction) method as implemented in SPM toolbox (ACID branch) presented in (Ruthotto et al., 2012). HySCO had the efficient performance for diffusion MRI of spinal cord as shown in Chapter. 4 and (Snoussi et al., 2017; Snoussi et al., 2019).

Segmentation of the cord and identification of vertebral level

Using SCT toolbox (De Leener et al., 2017), the whole spinal cord segmentation was carried out on T_1-weighted, as well as on the mean of DWI ($b = 900$ s·mm^{-2}) corrected for distortion. Then, we manually identified two vertebral levels, C3 and T1, to fulfill the requirements for the registration to the PAM50 template.

5.4.2 Computation of diffusion-based metrics

The diffusion-weighted signal in white matter was modelled in the spinal cord using Diffusion Tensor Imaging (DTI) in the one hand and Ball-and-Stick (B&S) model (Behrens et al., 2007) in the other hand, which we briefly describe in the sequel.

Diffusion tensor model The diffusion tensor model assumes that the probability of water molecules displacement follows a zero-mean 3D Gaussian. The diffusion tensor, directly related to the covariance matrix, is a 3×3 symmetric, positive-definite matrix. From its eigenvalue decomposition, we can extract rotation-invariant indices. In this chapter, we focussed on the radial diffusivity (RD), the axial diffusivity (AD), the mean diffusivity (MD) and the fractional anisotropy (FA). Note that MD can be expressed as a combination of AD and RD:

$$MD = \frac{AD + 2\,RD}{3} \tag{5.1}$$

Ball-and-stick model Contrary to the diffusion tensor model, the ball-and-stick model is a two-compartment model, where each compartment provides a normalized MR signal S_1 and S_2. These signal models correspond to intra- and extra-axonal diffusion, respectively. For the intra-axonal compartment, S_1 refers to signals coming from water inside the axons in which the diffusion is restricted. For the extra-axonal compartment, S_2 refers to signals coming from water outside the axons. For ball-and-stick model, the first compartment is a *stick*, anisotropic component, which has fiber direction $\mathbf{n}$ and diffusivity d as parameters (Behrens et al., 2003). The *stick* compartment describes diffusion in an idealized cylinder with zero radius. The signal for this component is:

$$S_1(d, \mathbf{n}; b, G) = \exp\left(-bd(\mathbf{n} \cdot \mathbf{G})^2\right), \tag{5.2}$$

where b is the diffusion-weighting parameter and $\mathbf{G}$ is the gradient direction.

The second compartment, called a *ball*, is an isotropic component which has only the diffusivity d_0 as parameter in its signal described as:

$$S_2(b) = \exp(-bd_0). \tag{5.3}$$

In our implementation, d_0 is fixed to $3.0 \cdot 10^{-3}$ mm^2/s, which corresponds to the free diffusion coefficient of water.

The signal model is therefore

$$S(d, \mathbf{n}, f; b, G) = (1 - f)\, S_1(d, \mathbf{n}; b, G) + f\, S_2(b).$$

The parameters of interest we extracted from this model are f, the free water weight (FWW), and d, the stick axial diffusivity (or Stick-AD).

In addition to these metrics we also computed the mean angle direction (MAD) and angular concentration of directions (ACD), the geometric measures of alignment of the diffusion direction

with the local orientation of the spine introduced in Chapter 4. MAD and ACD were computed using both diffusion reconstruction models, DTI and B&S. A summary of the extracted metrics is reported in Table 5.3.

Type of metric	Diffusion Tensor Imaging (DTI) model	Ball-and-Stick (B&S) model
Scalar metrics	AD, FA MD, RD	FWW Stick-AD
Geometric metrics	MAD-DTI ACD-DTI	MAD-B&S ACD-B&S

Table 5.3: Computed scalar and geometric metrics using both diffusion reconstruction models: 10 metrics.

5.4.3 Quantification of metrics per vertebral level

Here, our aim is to compute the mean of metrics for each vertebral level. To do so, we proposed a processing pipeline to align the labels defined in the PAM50 template (De Leener et al., 2018) to the native DWI space of each subject, as summarized in Figure.5.2.

First, the T_1-weighted anatomical image was registered to the PAM50-T1 spinal cord template (De Leener et al., 2018); this generates forward and inverse warping field between them. Next, the PAM50-T1 template (De Leener et al., 2018) was registered to the mean DWI using the inverse warping field from previous registration as an initial warping field.

Here, we preferred T_1-weighted to T_2-weighted since its isotropic resolution made the registration more effective. Alignment with the template provides robust definition of the inter-vertebral levels for the spine. This enables computation of the average metrics in spinal cord using the atlas-based approach introduced in (Lévy et al., 2015), which overcome biases related to partial volume effects. As a result, we can quantify diffusion-based metrics averaged for each inter-vertebral level in cervical part. Especially for scalar metrics, we quantify them only in white matter referring to PAM50 template. The processing pipeline is summarized in Figure.5.2.

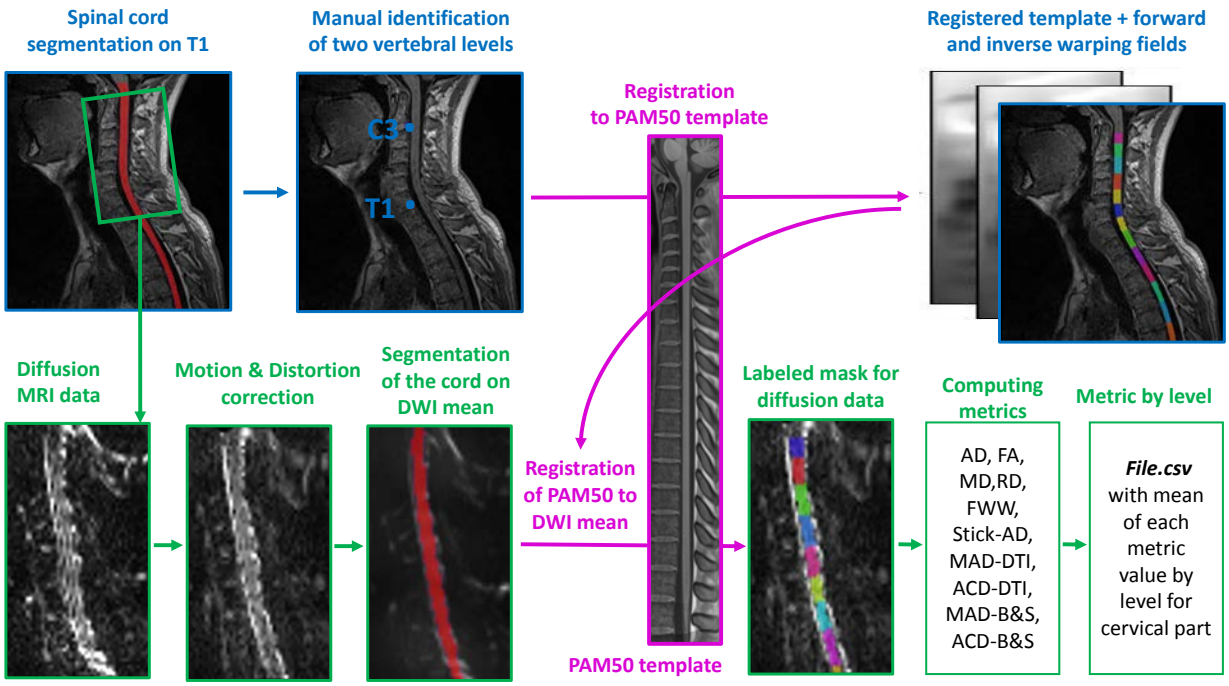

Figure 5.2: Illustration of the automated analysis pipeline. (1) Segmentation of the cord on T1. (2) Manual identification of two vertebral levels. (3) Registration to the PAM50 template. (4) Motion and distortion correction of dMRI data. (5) Segmentation of the cord using DWI mean data. (6) Registration of PAM50-T1 registered to DWI mean data using the inverse warping field from previous registration as an initial warping field. (7) Computing DTI and Ball&Stick metrics. (8) Quantification of metrics by vertebral level of the cervical part.

5.4.4 Quality Control

As we described in Chapter.4, Section.4.6, we performed a careful quality control (QC) on the raw data and after each processing step in order to ensure the quality of the analysis and the accuracy of the results.

5.5 Classical statistical analysis

From the processing pipeline we just described, we obtain data specific to every vertebral level of every subject in our cohort. In this section, we report results of a statistical analysis between patients and controls, for each metric separately.

5.5.1 Pairwise comparisons

The EMISEP cohort is comprised of 29 healthy volunteers and 53 MS patients with segmented lesions. This sample size is relatively small compared to the number of metrics we extracted, and the relatively small volume of the regions of interest across which we computed the mean. In this section, we study the opportunity to pool data from several vertebral levels to increase the statistical power of our analysis.

To do so, we performed a two-way analysis of variance between vertebrae levels for each metric to illustrate the interaction term between them. We compare all pairs of vertebrae levels

of one subject, for each level of all the other subjects. This test reveals the degree to which one subject is differentially effective at each vertebrae level of a second subject. This test can be performed using the Estimated Marginal Means (EMMs), sometimes called least-squares means, are predictions from a linear model over a reference grid; or marginal averages thereof.

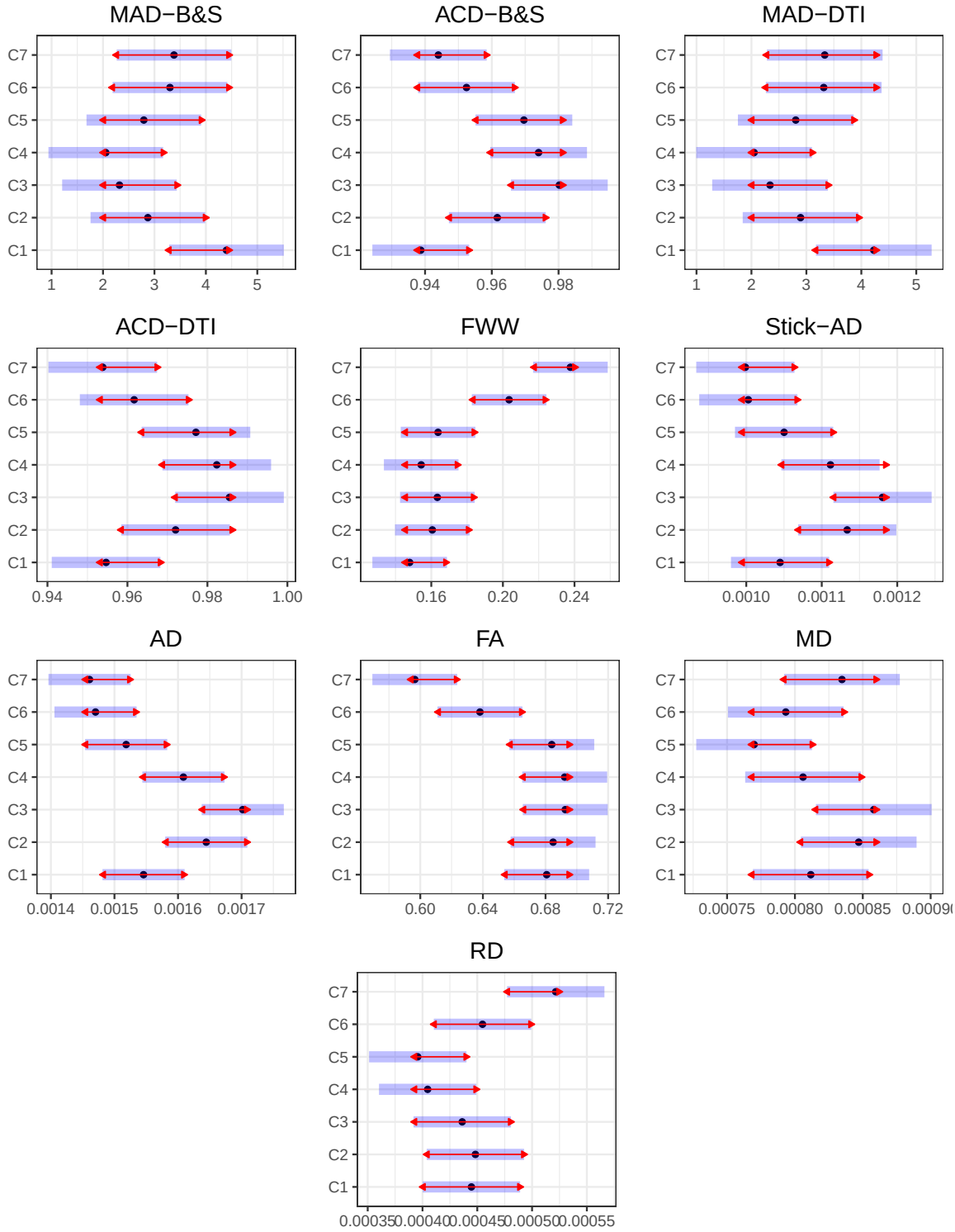

Figure 5.3: Estimated marginal means (x axis) for each metric in cervical vertebral levels (y axis) for healthy volunteers data. The blue bars are confidence intervals for the EMMs, and the red arrows are for the comparisons among them. If an arrow from one level overlaps an arrow from another level, the difference is not significant (p-value > 0.05). Else, the difference is significant (p-value< 0.05).

Figure.5.3 summarizes graphically this comparisons for all 10 metrics computed only on healthy volunteers data. The blue bars are confidence intervals for the EMMs, and the red arrows are for the comparisons among them. If an arrow from one level overlaps an arrow from another level, the difference is not significant and p-value between them is superior to 0.05. Alternatively, if there is no overlap between two red arrows, this means that the difference between these two vertebral levels is significant and p-value inferior to 0.05.

Table 5.4 summarizes intervals of vertebral levels in which there is no significance difference. We remark that for all metrics, the [C2,C4] interval shows no significance difference. This leads to the possibility of merging metrics quantified in C2, C3 and C4 vertebral levels.

Metric	Interval without significance difference
MAD-B&S	[C1-C3] or [C2-C7]
ACD-B&S	[C1-C2] or [C2-C5] or [C3-C5]
MAD-DTI	[C1-C3] or [C2-C7]
ACD-DTI	[C1-C2] or [C2-C6] or [C5-C7]
FWW	[C1-C5] or [C6-C7]
Stick-AD	[C1-C2] or [C2-C4] or [C4-C7]
AD	[C1-C2] or [C2-C4] or [C5-C7]
FA	[C1-C5] or [C6-C7]
MD	[C1-C4] or [C4-C7]
RD	[C1-C6] or [C6-C7]
Common interval	**[C2-C4]**

Table 5.4: Summary of the pairwise comparisons for each metric between all vertebrae levels for healthy volunteers data

5.5.2 Unpaired t-test between healthy volunteers and MS patients

We perform Welch's t-test between healthy volunteers and MS patients data in [C2,C4] region. This t-test is an adaptation of Student's t-test and is more reliable when the two samples have unequal variances and/or unequal sample sizes. It is often referred to as *unpaired* or *independent samples* t-tests. In this statistic test and as illustrated in Equation. 5.4, for each metric i, we have 29×3 vertebral levels considered as 87 healthy controls in $\mathcal{V}_i$, 66×3 vertebral levels considered as all MS patients in $\mathcal{ALL}_i$, 86 vertebral levels considered as vertebral level without lesion detected in $\mathcal{NAWM}_i$, and 36 vertebral levels posses lesion with volume superior to 5% of the corresponding vertebral level volume in $\mathcal{MS}_i(5)$. More details about these in following equation:

$$
\begin{aligned}
\mathcal{V}_i &= \Big[volunteer_1 \Big[m_i(c_2), m_i(c_3), m_i(c_4) \Big], ..., volunteer_{29} \Big[m_i(c_2), m_i(c_3), m_i(c_4) \Big] \Big] \\
\mathcal{ALL}_i &= \Big[patient_1 \Big[m_i(c_2), m_i(c_3), m_i(c_4) \Big], ..., patient_{66} \Big[m_i(c_2), m_i(c_3), m_i(c_4) \Big] \Big] \\
\mathcal{NAWM}_i &= \Big[patient_1 \Big[m_i(c_j) \Big], ..., patient_{66} \Big[m_i(c_j) \Big] \Big], \; c_{j \in (2,3,4)} \; without \; lesion \\
\mathcal{MS}_i(thr\%) &= \Big[patient_1 \Big[m_i(c_j) \Big], ..., patient_{66} \Big[m_i(c_j) \Big] \Big], \; c_{j \in (2,3,4)} \; with \; lesion > thr\%
\end{aligned}
\tag{5.4}
$$

where, m_i is the chosen metric with its index $i \in \{1,..,10\}$, c_2, c_3 and c_4 are the vertebral level and thr is threshold of volume lesion. Note that we refer to vertebral level as normal-appearing white matter (NAWM) when there is no lesion detected by 9 raters. Mean, standard deviation and t-test results for these vectors are presented in Table. 5.5.

For both geometric metrics and AD, there is no detectable difference between values in healthy controls and MS patients even without lesion. In contrast, FWW significantly increases in MS patients, regardless of the presence and the volume of lesions. For the second component of Ball-and-Stick model, Stick-AD, there is significant decrease on MS patients. FA shows significant decrease on all MS patients and those whom possess lesions > 5% of the corresponding vertebral level volume. RD increases significantly with all MS patients and those have lesion > 5%. Finally, MD shows significant increase on MS patients having lesion when compared to healthy volunteers. Otherwise, for ACD-DTI, we remark that there is a significant difference on $\mathcal{NAWM}$ comparing to healthy volunteers without any significant on MS patients with lesions.

Note that for this t-test we fixed the threshold of volume lesion as compromise with the size of available data. FWW, FA, MD and RD of MS patients still have significant difference for various threshold until 22%, but Stick-AD has a p-value < 0.05 until 12% and p-value < 0.07 until 16%.

Data	**Healthy volunteers**		**MS patients**					
	$\mathcal{V}_i$ (n=87)		$\mathcal{ALL}_i$ (n=198)		$\mathcal{NAWM}_i$ (n=86)		$\mathcal{MS}_i(5\%)$ (n=36)	
Metric	Mean	STD	Mean	STD	Mean	STD	Mean	STD
MAD-B&S	2.4152	1.8907	2.6798	1.7963	2.5939	1.8188	2.7365	1.6500
ACD-B&S	0.9720	0.0294	0.9669	0.0270	0.9639	0.0271	0.9672	0.0234
MAD-DTI	2.4272	1.8977	2.7089	1.7963	2.6386	1.8352	2.7830	1.5926
ACD-DTI	0.9800	0.0209	0.9748	0.0201	0.9731	0.0184	0.9756	0.0166
FWW	0.1594	0.0431	0.1849	0.0669	0.1774	0.0672	0.2076	0.0735
Stick-AD	0.0011	0.0003	0.0011	0.0003	0.0011	0.0003	0.0010	0.0002
AD	0.0017	0.0002	0.0016	0.0002	0.0016	0.0003	0.0017	0.0002
FA	0.6899	0.0800	0.6584	0.0941	0.6774	0.0941	0.6150	0.0908
MD	0.0008	0.0001	0.0009	0.0002	0.0008	0.0002	0.0009	0.0002
RD	0.0004	0.0001	0.0005	0.0002	0.0004	0.0002	0.0005	0.0002

Table 5.5: For C2, C3 and C4 levels, mean and STD of each metric for healthy volunteers, for MS patients with or without lesions and for MS patients with lesion >5%. Dark green means that there is a significant difference between healthy volunteers and MS patients and p-value is inferior to 10^{-2}, weak green means that p-value shows significant difference but 10^{-2} < p-value < 5.10^{-2}. n represents the number of vertebral level data available in [C2,C4] region.The unit of FWW, Stick-AD, AD, MD and RD is mm^2/s, for MAD-DTI and MAD-B&S is degree.

5.6 Multivariate learning for the detection of MS lesions

In this section, we propose to use the diffusion MRI data to automatically detect the presence of a lesion. Based on a selection of metrics extracted from diffusion, we learn a linear classifier using linear discriminant analysis. In order to reduce the dimension of the feature vector, we present two different strategies :

- We manually select a set of measures with limited cross-correlation

- We perform a principal component analysis (PCA) and then learn a linear classifier on the reduced set of PCA components which explain more than 90% of the variance.

Throughout this section, we will evaluate classification results using the area under the curve (AUC) of the receiver operating characteristic curve (ROC). When applicable, we report mean and standard deviation of ROC AUC for 1,000 splits of the dataset into training and testing parts, representing respectively 67% and 33% of the original dataset. More details of how this is computed is summarized in section 5.A.

5.6.1 Univariate classification using diffusion metrics

Complementary to the t-tests presented in section 5.5.2, we computed the classification score when using each individual metric as a criterion for classification. To compute the ROC AUC for each metric independently, we follow Algorithm. 1. The data vector X and label vector Y of each metric is constructed as follows:

$$\begin{aligned} X_i(thr) &= \Big[\Big[\ \ \mathcal{V}_i\ \ \Big], \Big[\mathcal{MS}_i(thr\%)\Big]\Big], \ with\ thr\ \in\ \{2\%, 4\%, \ldots, 20\%\} \\ Y_i(thr) &= \Big[\Big[0,..,0\Big], \Big[\ \ \ 1,..,1\ \ \ \Big]\Big] \end{aligned} \tag{5.5}$$

where, $i \in \{1,..,10\}$ is the index of the chosen metric, and thr is the threshold of volume lesion.

Algorithm 1 ROC AUC for each metric independently

I. We fix thr from {0.02,0.04,..,0.20}

II. We construct the data vector X and its label vector Y. We give 0 to healthy volunteers and 1 to MS patients.

III. We standardize X to get X_{scaled} by centering to the mean and component wise scale to unit variance.

IV. We compute ROC AUC score between X_{scaled} and Y.

Results are presented in Figure.5.4; we remark that FA, MD and RD have the best performance of classification between vertbral levels of healthy volunteers and MS patients. FA reaches 0.8 score of ROC AUC from 12% of lesion volume, RD reaches the same score from 15% and MD from 18%. These 3 metrics have monotonic increasing ROC AUC as a function of lesion volume. FWW reaches 0.75 score of ROC AUC at 10% of volume lesion and remains in the range $[0.68, 0.75]$ along the various thresholds. However, MAD-B&S, MAD-DTI, ACD-B&S, ACD-DTI and Stick-AD have a poor score of ROC AUC and remains in $[0.57, 0.70]$. This is in line with the p-values reported above in section 5.5.2.

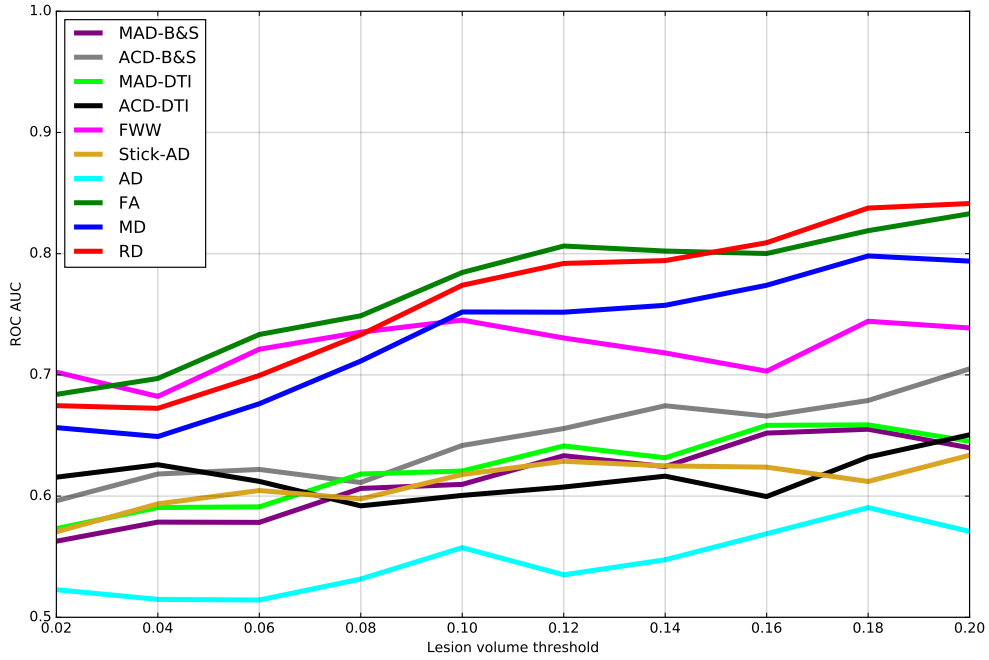

Figure 5.4: ROC AUC for scalar and geometric metrics between MS patients and healthy volunteers. Lesion volume is the part of the vertebral volume occupied by a lesion.

5.6.2 Linear discriminant analysis of native diffusion features

In order to build a classifier which combines a set of metrics, we use Linear discriminant analysis (LDA) (Ripley, 2002), which is a generalization of Fisher's linear discriminant (Fisher, 1936). LDA is a method used to find a linear combination of features that separates or characterizes two or more classes of objects. The resulting combination may be used as a linear classifier.

Learning and testing a linear classifier The full experience setup is summarized in algorithm 2. So, the data vector X_{comb} and label vector Y_{comb} is constructed as following:

$$\begin{aligned} X_{comb}(thr) &= \Big[\Big[X_i(thr)\Big],..,\Big[X_j(thr)\Big]\Big] \\ Y_{comb}(thr) &= \Big[\Big[Y_i(thr)\Big],..,\Big[Y_i(thr)\Big]\Big] \end{aligned} \tag{5.6}$$

where i and j are the index of the chosen metrics and thr is threshold of volume lesion.

Note that depending on the volume lesion threshold, the number of vertebral level we have in the patient group by differ. In fact, X_{comb} contains vertebral levels of healthy volunteers (29×3) and vertebral levels of MS patients that possess lesion. Figure.5.5 shows the count of vertebral levels having lesion for different threshold of percentage lesion volume cumulatively in [C2-C4] region. This figure gives an idea about the sample size of training/testing datasets used in the following analysis.

Algorithm 2 ROC AUC for a combination of metric

I. We fix thr from {0.02,0.04,..,0.20}

II. We construct the data vector X_{comb} and its label vector Y_{comb}. For label vector, we give 0 to healthy volunteers and 1 to MS patients.

III. We standardize X_{comb} to get X_{scaled} by centering to the mean and component wise scale to unit variance.

IV. We split X_{scaled} 1000 consecutive times in different X_{train} (67%) and X_{test} (33%) with their corresponding Y_{train} and Y_{test}.

IV.1. We fit LDA using X_{train} and Y_{train}.

IV.2. Using the fitted LDA, we predict confidence score on X_{test} to obtain Y_{LDA}.

IV.3. We compute ROC AUC score between Y_{test} and Y_{LDA}.

V. We calculate the mean and variance of ROC AUC scores which is computed in 1,000 consecutive times.

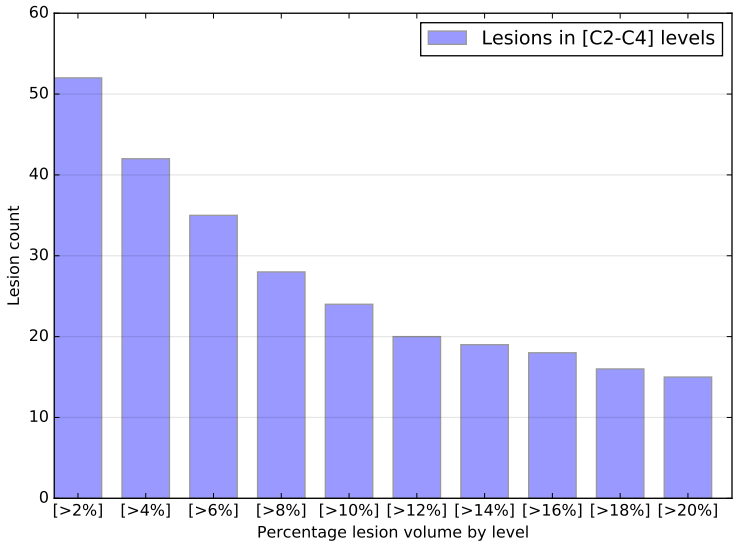

Figure 5.5: Distribution of lesion's volume in [C2-C4] region in 10 thresholds.

Selecting a subset of measures As mentionned earlier, since the sample size is relatively small, we need to reduce the degrees of freedom of our linear classifier by choosing a subset of metrics. We will try to choose a subset of metrics which bring complementary information; to do so, we first calculate the normalized covariance matrix for all metrics in [C2-C4] region on healthy volunteers $\mathcal{V}$, $\mathcal{NAWM}$, $\mathcal{MS}(5\%)$ and $\mathcal{MS}(10\%)$ as shown in Figure.5.6. Dark blue square shows strong correlation between 2 metrics and white square indicates no relationship between them.

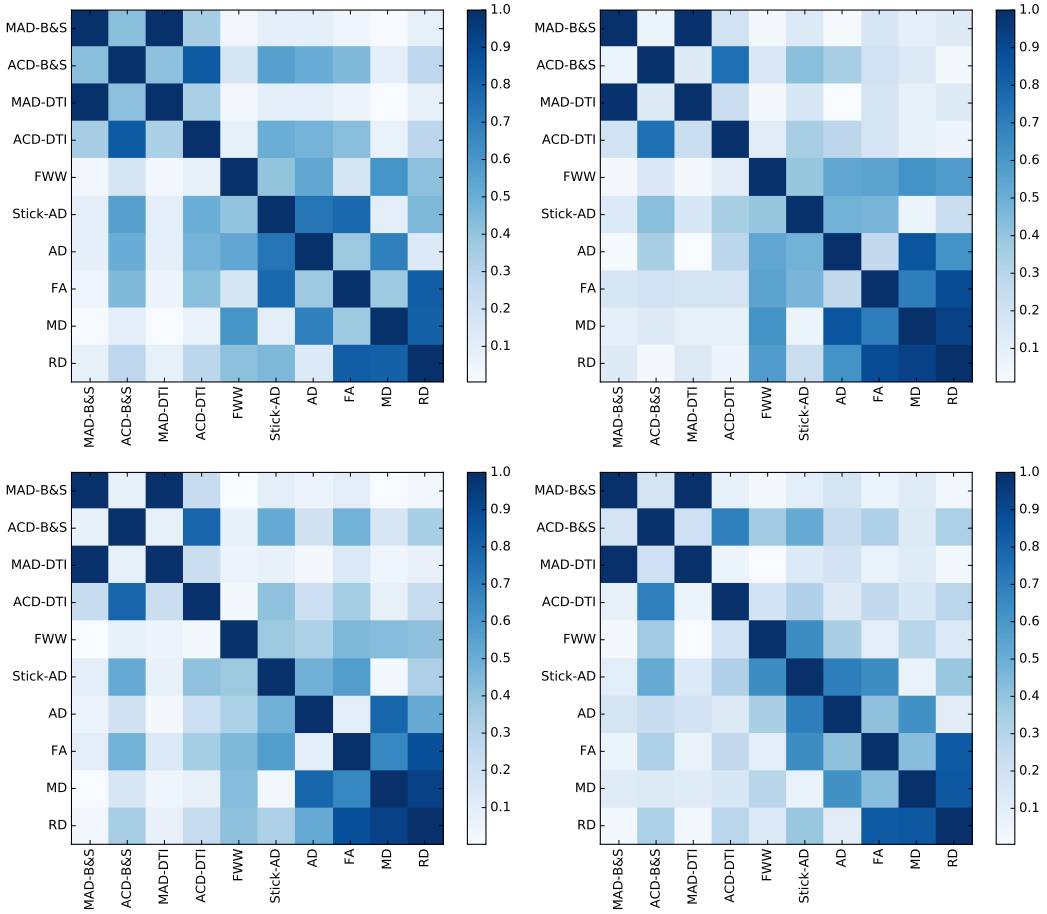

Figure 5.6: Normalized covariance matrix of metrics in [C2-C4] levels for healthy volunteers (1st line left), NAWM (1st line right), $\mathcal{MS}(5\%)$ (2nd line left), $\mathcal{MS}(10\%)$ (2nd line right). Dark blue square shows strong correlation between the two metrics and white square indicates no relationship between them.

Based on these correlations, we can propose in Table 5.6 combinations of metrics to be studied. We restrict ourselves to metrics with high potential because they show good classification (see section 5.6.1) and/or present significant difference between MS patients and controls (see section 5.5.2).

2 metrics	FWW	RD
	FWW	MD
	FWW	FA
	Stick-AD	MD
	Stick-AD	RD
	Stick-AD	FWW
	FA	MD
	FA	RD

3 metrics	FA	RD	FWW	
	FA	RD	MD	
	FA	AD	RD	
	FA	MD	FWW	
	AD	RD	FA	
	FWW	MD	Stick-AD	
	FA	RD	Stick-AD	
4 metrics	FA	RD	MD	FWW

Table 5.6: Proposed combinations of 2, 3 and 4 metrics to be studied.

Results of linear discriminant analysis In Figure.5.7 and Figure.5.8, we show ROC AUC mean and its variance of each combination superposed by ROC AUC each metric used in this combina-

tion. This superposition is useful since it shows whether using a combination of metrics improves on using each metric separately.

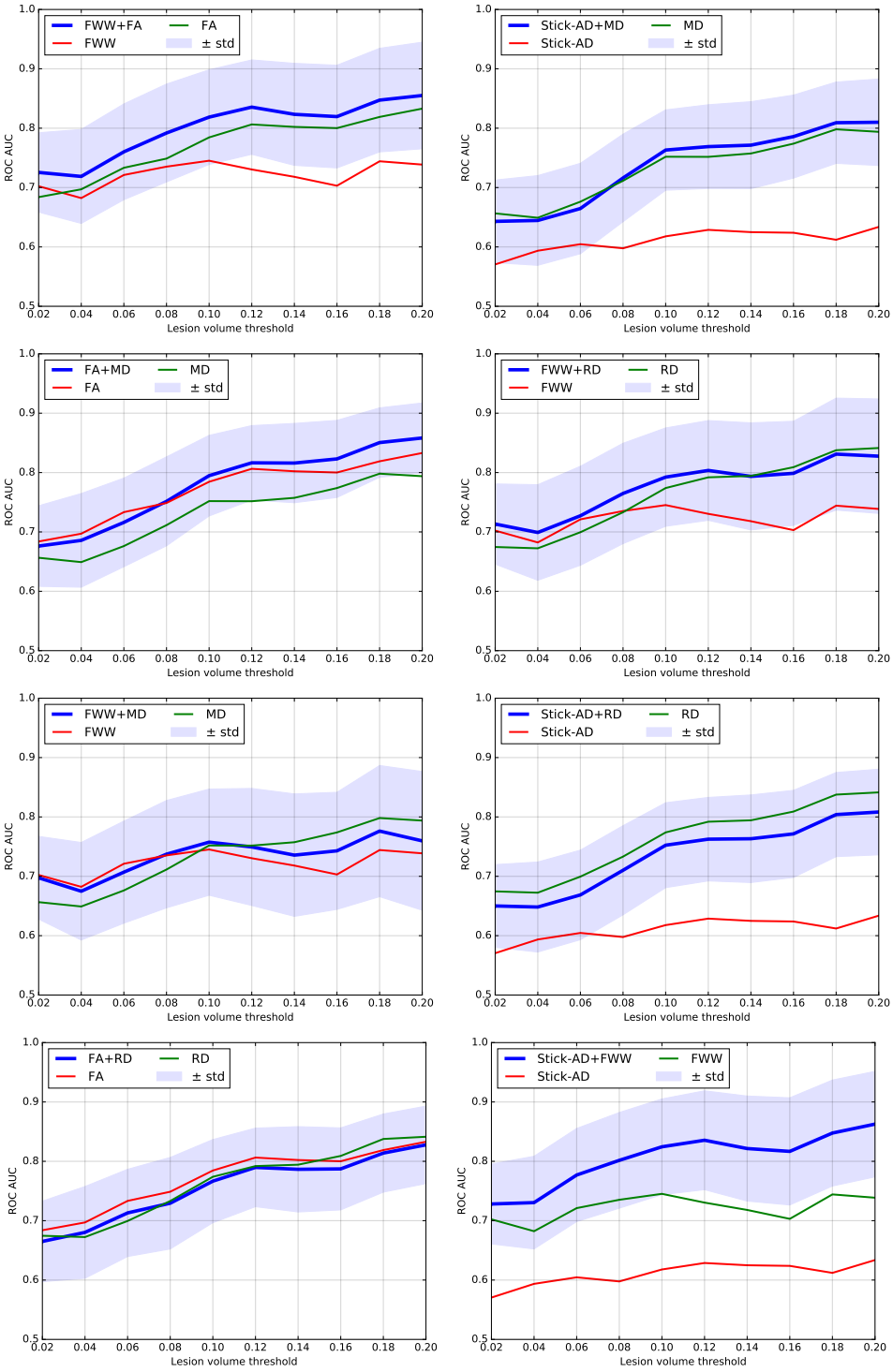

Figure 5.7: ROC AUC for various combinations of **2 metrics** between MS patients and healthy volunteers.

Figure.5.7 shows that when combining FWW and Stick-AD metrics, ROC AUC mean score to separate controls and MS patients is better then using each metric independently. Also, when combining Stick-AD by MD or RD, ROC AUC mean score still better then that of Stick-AD. For [FA, FWW] and [FA, MD], the combination is slightly better as the ROC AUC score of each

metric still in the variance margin of ROC AUC score of combination. For [RD, FWW], [MD, FWW], [RD, FA] and [RD, Stick-AD], ROC AUC mean is similar or close the ROC AUC of each metric composed this combination. With $\mathcal{MS}(10\% - 20\%)$ and, the best scores of classification are approximately in [0.83,0.87] using [FA,FWW] and [Stick-AD,FWW].

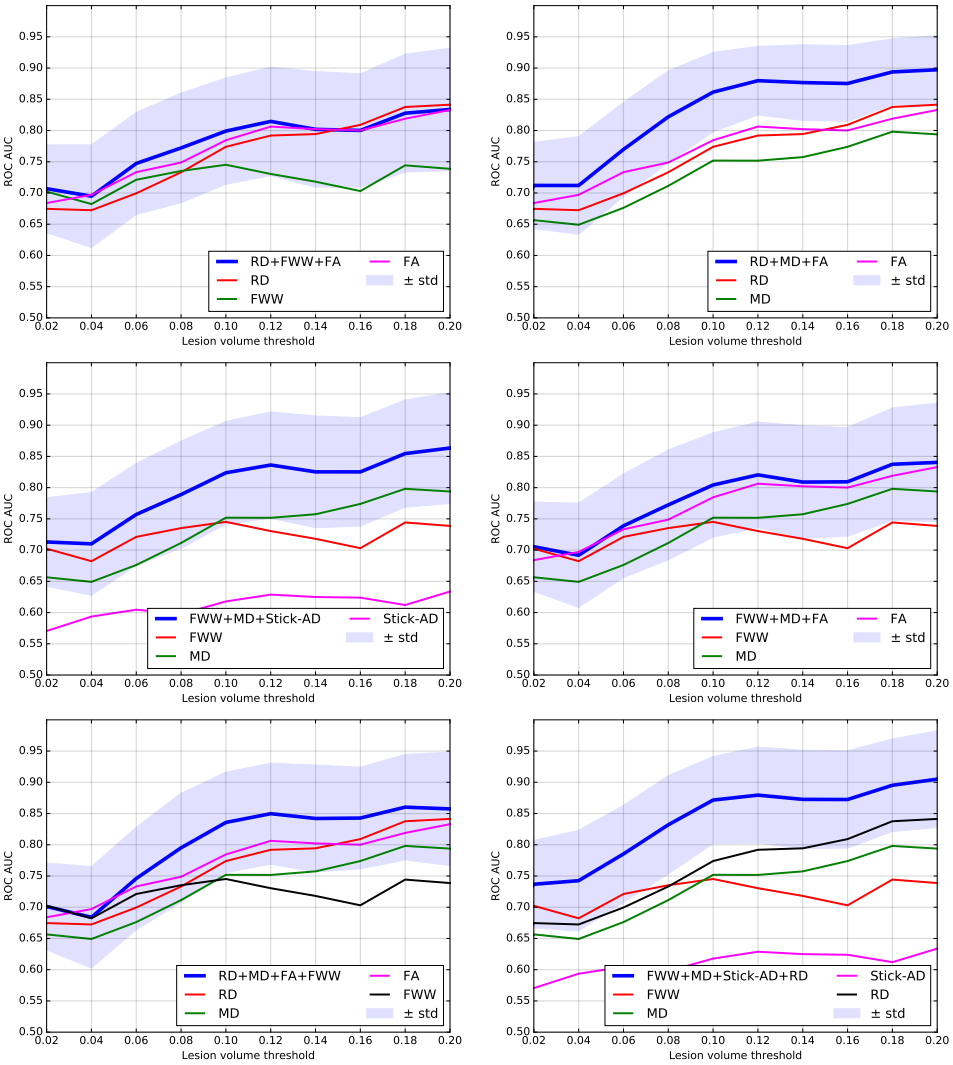

Figure 5.8: ROC AUC for various combinations of **3 and 4 metrics** between MS patients and healthy volunteers.

In Figure.5.8, we show the mean and the variance of ROC AUC score for combination of 3 metrics : [RD,FWW,FA], [RD,MD,FA], [FWW,MD,Stick-AD] and [FWW,MD,FA].

For these combination, we remark that for both of [RD,MD,FA] and [FWW,MD,Stick-AD], the ROC AUC mean of combination is better than ROC AUC score of each metric independently. For $\mathcal{MS}(10\% - 20\%)$, [FWW,MD,Stick-AD] has ROC AUC mean in [0.82,0.86] and [RD,MD,FA] in [0.86,0.90] which is an interesting result. For [RD,FWW,FA] and [FWW,MD,FA], there is no remarkable difference. Otherwise, we present also in Figure.5.8, two combination of 4 metrics: [RD,FWW,FA,MD] and [FWW,Stick-AD,MD,RD]. For $\mathcal{MS}(10\% - 20\%)$, [RD,FWW,FA,MD] has ROC AUC mean in [0.84,0.86] and [FWW,Stick-AD,MD,RD] has ROC AUC mean in [0.87,0.91]. In Figure.5.9, we overlaid various combinations in order to have more compare between them.

To sum up, we can deduce that from all combinations, the combinations [RD,MD,FA] and

[FWW,Stick-AD,MD,RD] give the best score of prediction between healthy volunteers and MS patients with lesion.

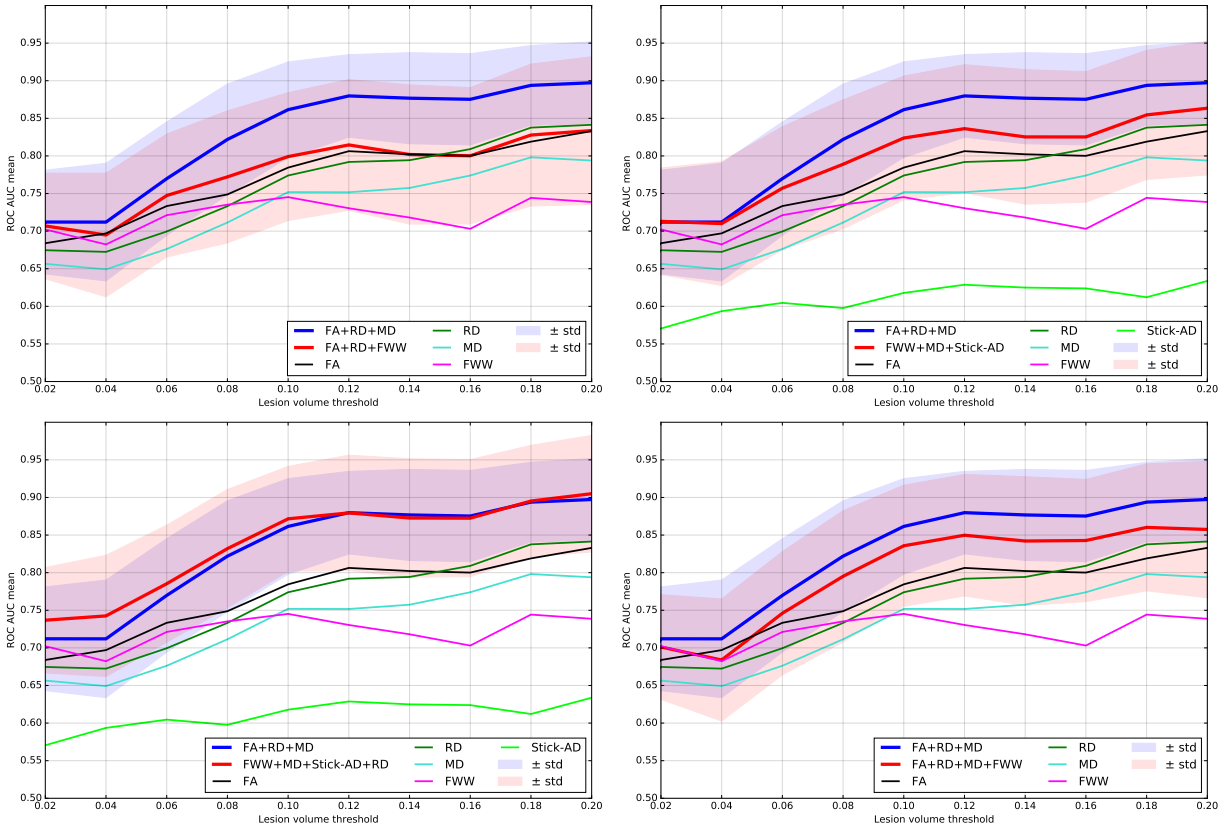

Figure 5.9: Overlays of ROC AUC mean for the best combinations.

5.6.3 Principal component analysis prior to LDA

In order to reduce the dimension of the feature vector, an alternative to manually selecting a subset of metrics, as done in the previous section, is to use principal component analysis (PCA). PCA will compute a linear, orthogonal transform of the original feature vector into a new space of features, which will be ranked by their decreasing variance. In this space, keeping the first few components generally gives a good approximation of the original data. The vector data X_{PCA} and vector label Y_{PCA} for PCA are computed as follows:

$$\begin{aligned} X_{PCA}(thr) &= \Big[\Big[X_1(thr)\Big],..,\Big[X_9(thr)\Big]\Big] \\ Y_{PCA}(thr) &= \Big[\Big[Y_1(thr)\Big],..,\Big[Y_9(thr)\Big]\Big] \end{aligned} \tag{5.7}$$

Note that only kept 9 metrics out of 10: we removed AD (computed from DTI) since it is linearly related to MD and RD (see Eq. 5.1). In fact, this collinearity renders the interpretation of the LDA estimated coefficients impossible. For example, if an increase in AD, is associated with an increase in MD and they both decrease variable X, every change in AD will be compensated by a change in MD and the effect of AD on X or on LDA classification will be underestimated.

In Algorithm. 3, we present steps followed to compute ROC AUC of PCA components on various thresholds of percentage for volume lesion. The cumulative sum for percentage of variance

explained by the 9 components of PCA fitted in [C2-C4] region is presented in Table. 5.7.

Algorithm 3 Principal Component Analysis

I. We fix thr from {0.02,0.04,..,0.20}

II. We construct the data vector $X_{PCA}(thr)$ and its label vector $Y_{PCA}(thr)$. For label vector, we give 0 to healthy volunteers and 1 to MS patients.

III. We standardize X_{PCA} to get X_{scaled} by centering to the mean and component wise scale to unit variance.

IV. We split X_{scaled} 1000 consecutive times in different X_{train} (67%) and X_{test} (33%) with their corresponding Y_{train} and Y_{test}.

IV.1. We define PCA model with k components, where k is in {1,..,9}

IV.2. We fit PCA with X_{train} and apply the dimensionality reduction on X_{train} to obtain X_{train_PCA}.

IV.3. We transform X_{test} using PCA from training set to obtain X_{test_PCA}.

IV.4. We define LDA model and fit it using X_{train_PCA} and Y_{train}.

IV.5. Using the fitted LDA, predict confidence score on X_{test_PCA} to obtain Y_{LDA}.

IV.6. We compute ROC AUC score between Y_{test} and Y_{LDA}.

V. We calculate the mean and variance of ROC AUC scores which is computed in 1000 consecutive times.

Data	cumulative sum for percentage								
	1st	2nd	3rd	4th	5th	6th	7th	8th	9th
$\mathcal{V}+\mathcal{MS}(02\%)$	41%	67%	85%	94%	98%	100%	100%	100%	100%
$\mathcal{V}+\mathcal{MS}(10\%)$	39%	65%	85%	93%	98%	100%	100%	100%	100%
$\mathcal{V}+\mathcal{MS}(20\%)$	40%	65%	86%	93%	98%	100%	100%	100%	100%

Table 5.7: The cumulative sum for percentage of variance explained by the 9 components of PCA fitted in [C2-C4] region. $\mathcal{V}$ is data of healthy volunteers, $\mathcal{MS}(thr)$ is data of MS patients patients possess lesion > thr% and $\mathcal{ALL}$ is data of all MS patients with/without lesion.

First two PCA components

ROC AUC mean for PCA components is presented in Figure.5.10. In previous section, we found that a combination of 3 metrics [FA,MD, RD] and a combination of 4 metrics [FWW,MD,Stick-AD,RD] give the best ROC AUC score, so we will focus only on the two components PCA as though a dimensionality reduction algorithm. In addition of this reason, we remarked that the classification accuracy of PCA drop after the second components, even though 99% of the total variance is covered as shown in Figure.5.11. For $\mathcal{MS}(10\%-20\%)$, 2 components of PCA has ROC AUC mean in [0.80,0.85]. However, we remark that [FA,MD, RD] and [FWW,MD,Stick-AD,RD] of metrics have a prediction score better than 2 components of PCA.

In Figure.5.12, the two first components of PCA for data including $\mathcal{MS}(5\%)$, $\mathcal{MS}(10\%)$, $\mathcal{MS}(15\%)$ and $\mathcal{MS}(20\%)$.

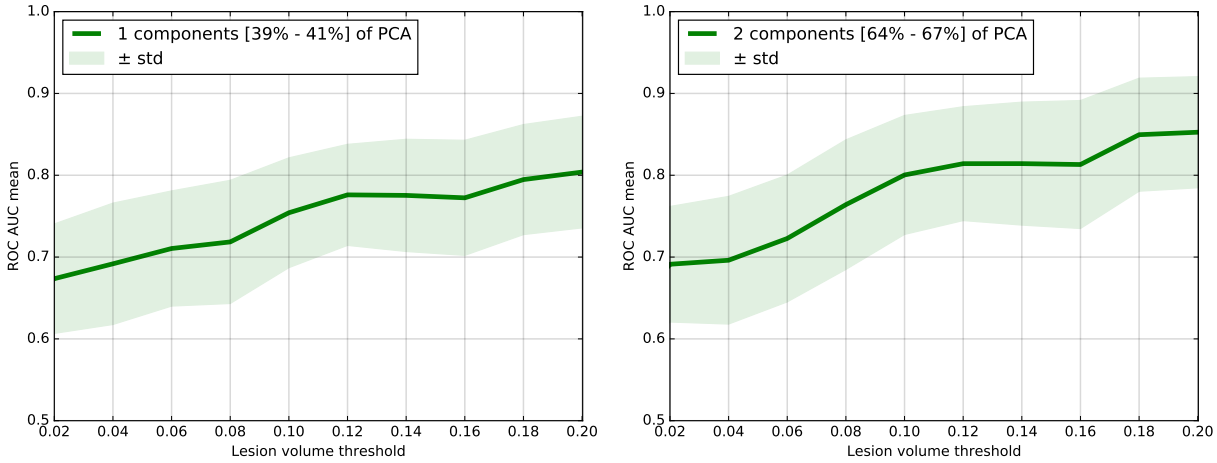

Figure 5.10: ROC AUC mean for PCA components trained on 9 metrics.

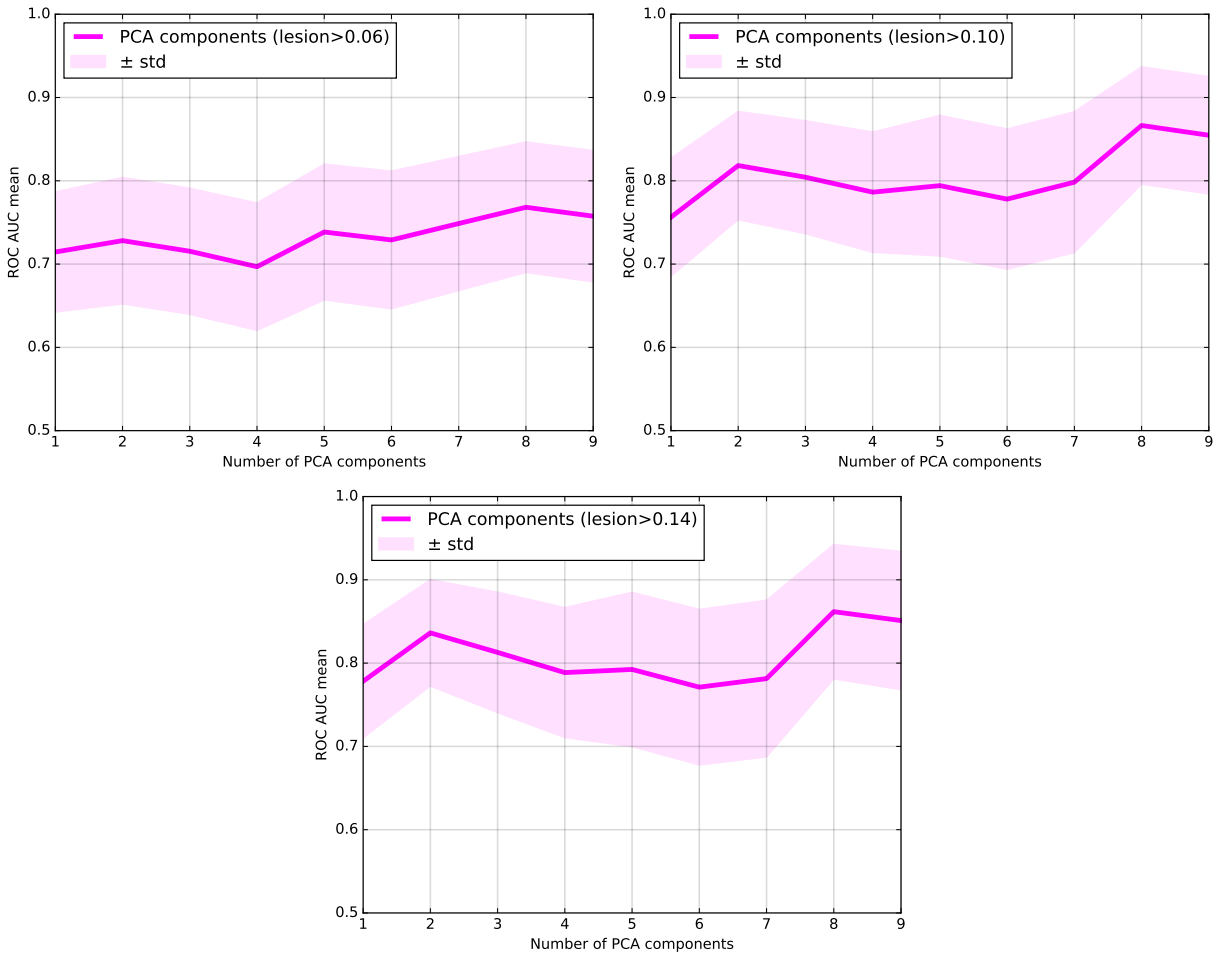

Figure 5.11: Variation of ROC AUC score of PCA using various number of components for volume lesion > to 6%, 10% and 14%.

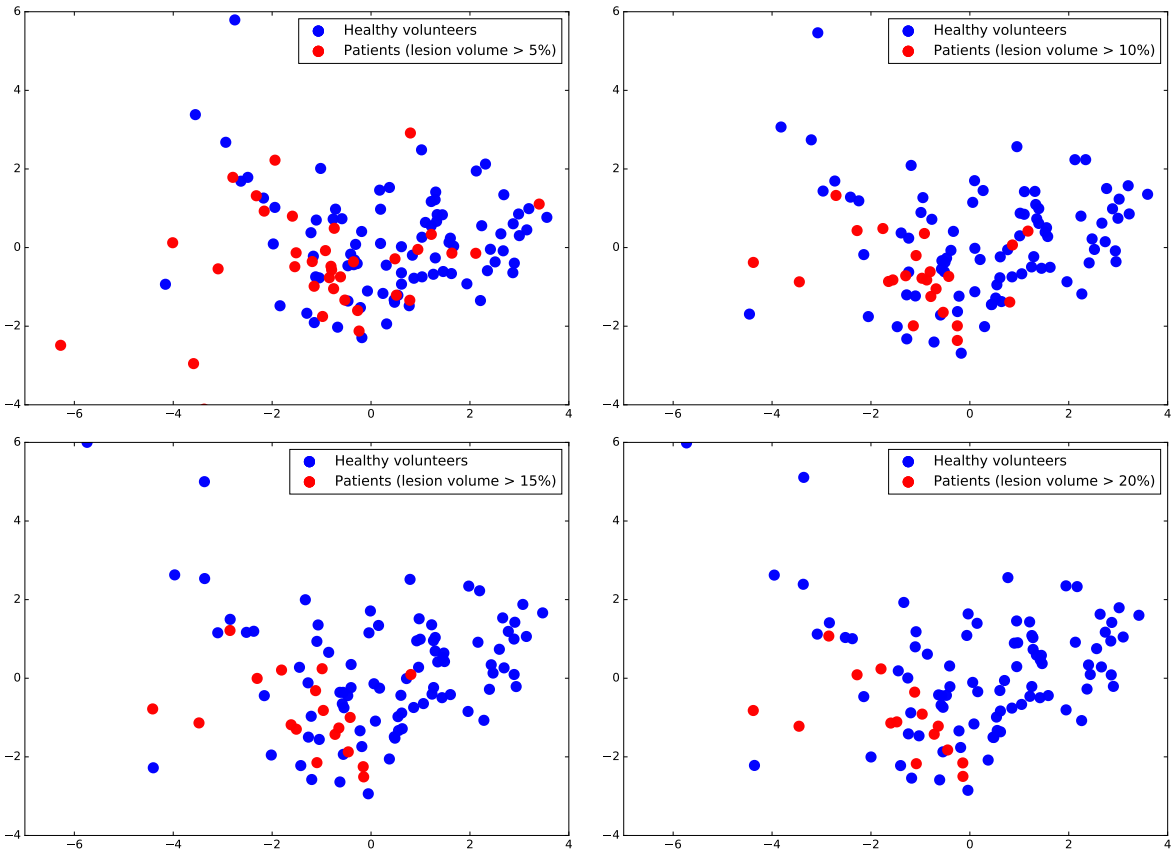

Figure 5.12: First two components [64%-67%] of PCA trained on 9 metrics.

Weights of each metric

After doing the LDA on the PCA data, having a way to interprete the results (the weights of the LDA) could be useful. Here, we re-project the weights of the LDA back to the original feature space. To do so, we follow steps explained in Algorithm. 4.

Algorithm 4 Weights of scalar and geometric metrics

I. We fix thr from {0.02,0.04,..,0.20}

II. We construct the data vector $X_{PCA}(thr)$ and its label vector $Y_{PCA}(thr)$. For label vector, we give 0 to healthy volunteers and 1 to MS patients.

III. We standardize X_{PCA} to get X_{scaled} by centering to the mean and component wise scale to unit variance.

IV. We define PCA model with 2 components.

V. We fit PCA with X_{scaled} and apply the dimensionality reduction on X_{scaled} to obtain X_{fitted}.

VI. We define LDA model and fit it using X_{fitted} and $Y_{PCA}(thr)$.

VII. Using the PCA, we transform back the weights vectors of LDA to its original space.

Table. 5.8 presents the LDA weights of each metrics which confirm that RD, MD, FA and FWW are representative metrics. This results is in correlation with the previous section in which we found [FA,MD, RD] and [FWW,MD,Stick-AD,RD] as a best combinations.

Data	LDA Weights									Score
$\mathcal{V}$+$\mathcal{MS}(0)$	0.01	-0.02	0.19	-0.05	0.02	-0.02	-0.20	0.23	0.24	0.71
$\mathcal{V}$+$\mathcal{MS}(4)$	0.00	-0.07	0.17	-0.09	0.01	-0.07	-0.23	0.22	0.25	0.70
$\mathcal{V}$+$\mathcal{MS}(8)$	-0.02	-0.01	0.26	-0.08	-0.02	-0.02	-0.28	0.34	0.35	0.75
$\mathcal{V}$+$\mathcal{MS}(12)$	-0.02	-0.05	0.29	-0.13	-0.02	-0.06	-0.36	0.41	0.45	0.79
$\mathcal{V}$+$\mathcal{MS}(16)$	-0.01	-0.05	0.29	-0.13	-0.01	-0.07	-0.36	0.42	0.45	0.82
$\mathcal{V}$+$\mathcal{MS}(20)$	-0.03	-0.07	0.32	-0.16	-0.02	-0.09	-0.42	0.47	0.51	0.85
	MAD	ACD	FWW	StickAD	MAD	ACD	FA	MD	RD	
	B&S metrics				DTI metrics					

Table 5.8: LDA weights and score on the first 2 components of PCA trained on 9 metrics.

5.7 Discussion and Conclusion

In this chapter we have proposed a pipeline to extract average dMRI metrics per vertebral level in spinal cord and we performed a statistical analysis to show their sensitivity associated with the presence and evolution of MS lesions within the same vertebral level. Diffusion measures involved are extracted from the diffusion tensor and the ball-and-stick models.

We show that FWW, Stick-AD, FA, MD and RD have a significant difference between healthy volunteers and MS patients within [C2-C4] region in cervical spinal cord. In regards to FA, MD and RD, there are already showed in other studies involved in spinal cord (Valsasina et al., 2005; Agosta et al., 2007a; Agosta et al., 2007b; von Meyenburg et al., 2013). However, we have many additions to them; firstly the size of the used data to validated these results is relatively large. Secondly, 9 raters including radiologists and experienced readers how are segment MS lesions in anatomical scans which guarantee high accuracy. Third, the proposed pipeline especially the way that we chose to quantify diffusion measures, atlas approach, is semi-automated and free from manual delineation bias. This method also accounts for partial volume effect using Gaussian mixture models. Fourth, we did a strict quality check of each step of the pipeline as a crucial step for the quality of the analysis and the accuracy of the results.

Beyond our study using DTI metrics, we also investigated the sensitivity of multi-compartment models, in particular FWW and Stick-AD, to detect lesions in MS patients. We show that the B&S multi-compartment model can provide novel information about the evolution of tissue microstructure, and should be included in the processing workflow. This also suggests that the acquisition protocol should be design to enable richer multi-compartment models, including several b-values (Scherrer and Warfield, 2012). To our knowledge, only neurite orientation dispersion and density imaging (NODDI) the multi-compartmental diffusion models have been used to measure and investigate microstructure and characterizing abnormalties on MS patients (By et al., 2017). But, this study used only one slice of cervical spine to investigate the sensitivity and feasibility of NODDI in patients with MS.

In our work, we performed a two-way analysis of variance between vertebrae levels for each metric to illustrate the interaction term between them. Table.5.4 summarizes intervals of vertebral levels in which there is no significance difference and we found the [C2,C4] interval shows no significance inter-difference for all 10 metrics. In fact, as we select best representative metric

for underlying microstructure of MS strucutre in t-test Table.5.5, it was possible to pool [C2-C5] instead of [C2,C4] for FWW, Stick-AD, FA, MD and RD. However, for MD metric, we found that p-value between C3 and C5 equals to 0.065, close to significant, as illustrated in Figure. 5.3. Thus, we prefered to keep [C2,C4] interval.

Furthermore, another important contribution is the way that we proposed, multivariate learning, to use the diffusion MRI data to automatically detect the presence of a MS lesion. Based on a selection of metrics extracted from diffusion, we learned a linear classifier using linear discriminant analysis (LDA) and we reduced the dimension of the feature vector using two different strategies. Throughout these strategies, we evaluated the classification results using the area under the curve (AUC) of the receiver operating characteristic curve (ROC).

The first strategy is to select manually a set of measures with limited cross-correlation. We found that combining some metrics reaches up the prediction score of such MS lesion and more performing than using each metric independently as shown in Figure. 5.7, 5.8 and 5.9. Also, we consider that a combination of 3 metrics [FA,MD, RD] and a combination of 4 metrics [FWW,MD,Stick-AD,RD] give the better ROC AUC score between healthy volunteers and MS patients with lesion. For $\mathcal{MS}(10\% - 20\%)$, MS patients with lesion volume between 10% and 20%, [RD,MD,FA] has ROC AUC mean score in [0.86,0.90] and [FWW,Stick-AD,MD,RD] has ROC AUC mean in [0.87,0.91]. These intervals of prediction score demonstrate that the classification accuracy is good and close to excellent (see section 5.A for more information about the traditional guide for classifying accuracy of ROC AUC).

The second strategy is to perform a principal component analysis (PCA) and then learn a linear classifier on the reduced set of PCA, first two components which explain more than 65% of the variance. For $\mathcal{MS}(10\% - 20\%)$, 2 components of PCA has ROC AUC mean in [0.80,0.85]. This prediction score is good but not better than the [FA,MD, RD] and [FWW,MD,Stick-AD,RD] combinations of metrics. In addition, Figure.5.12 illustrates the two first components of PCA for data including $\mathcal{MS}(5\%)$, $\mathcal{MS}(10\%)$, $\mathcal{MS}(15\%)$ and $\mathcal{MS}(20\%)$. This way of representation facilities a visual inspection to reassure our findings. In addition, we re-project the weights of the LDA back to the original feature space (Algorithm. 4) and we interpreted the LDA weights of each metric used in PCA. Results presented in Table. 5.8 is in correlation with our previous findings and confirm that RD, MD, FA and FWW are representative metrics.

In conclusion, we demonstrated the grade of sensitivity to underlying microstructure changes in MS of each metrics including DTI and Ball-and-Stick reconstruction models. Multi-compartment model can provide novel information about the evolution of tissue microstructure. We showed also that choosing a subset of metrics which bring complementary information has significantly increase the prediction score of the presence of this disease.

5.A Evaluating the classification results

5.A.1 Receiver operating characteristic curve analysis

Receiver operating characteristic (ROC) curve, is a graphical plot that illustrates the performance of a binary classification as its discrimination threshold is varied (McClish, 1989; Fawcett, 2006). It is the probability of detection (true-positive rate (TPR)) as a function of the probability of false alarm (false-positive rate (FPR)) at various threshold settings as shown in the illustrative example in Figure. 5.13.

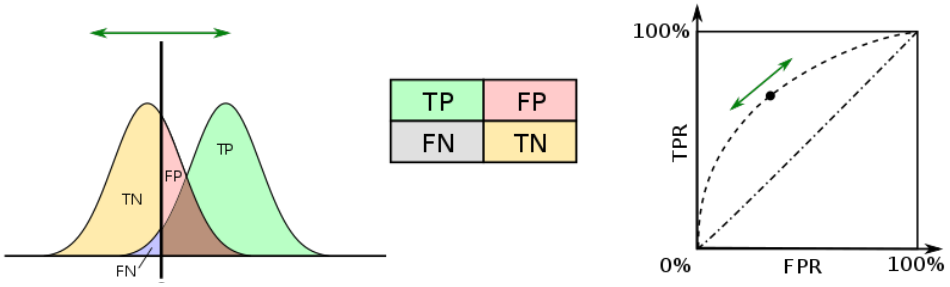

Figure 5.13: An illustrative example of the Receiver operating characteristic (ROC) curve. (adapted from *commons.wikimedia.org*).

As comparison of different classifiers in the ROC curve is not easy, one can reduces ROC curve to a scalar value that describes the expected accuracy by computing Area under the ROC curve, often refereed to AUC. AUC is the probability that a classifier will rank a randomly chosen positive instance higher than a randomly chosen negative one. Therefore, ROC AUC analysis involves evaluation of how much such classifier is efficient of distinguishing between classes and thus to select the optimal classifier and discard suboptimal ones. Higher the AUC, better the classifier is at predicting class 1 as class 1 and class 2 and class 2. The AUC score is always belongs to [0,1], when equals to 1 represents perfect classification and worthless classification if equals to 0.5 (Tharwat, 2018). Otherwise, there is no a standard scale or guide of ROC AUC score to segregate the quality of a classifier and still depending on the context. Traditional academic point system can be an approximative guide for classifying accuracy [3] : $[0.5-0.6]$:fail, $[0.6-0.7]$:poor, $[0.7-0.8]$:fair, $[0.8-0.9]$:good, $[0.9-1.0]$:excellent.

5.A.2 Training and testing data

Training a classifier and testing or evaluating it on the same data is a methodological mistake: a model that would just repeat the labels of the samples that it has just seen would have a perfect score but would fail to predict anything useful on yet-unseen data. To avoid over-fitting, we have to split our data into two different sets: a training set, 67% of data, which is used for learning the parameters of LDA, and a testing set, 33% of data, which is used for evaluating the fitted LDA.

Nevertheless, by defining these two sets of data, the prediction score may depend on the particular random choice for the pair of training and testing sets. To resolve this issue, we use random permutation cross-validation iterator. We split the whole data 1,000 consecutive times in different

[3] http://gim.unmc.edu/dxtests/roc3.htm

training and testing sets, then we return the averaged and the variance values of the 1,000 prediction scores obtained with these different sets. In our case, we use a cross-validation strategy available in *Scikit-Learn* in which random splits do not guarantee that all folds will be different.

Chapter 6

Reproducibility and Evolution of Diffusion MRI Measurements within the Cervical Spinal Cord in Multiple Sclerosis

Contents

6.1 Introduction

Multiple Sclerosis (MS) is a neuro-inflammatory disease associated with a range of clinical symptoms and progressive physical disability. The use of non-invasive MRI techniques is key to a better understanding and follow-up of the pathology. However, there is usually a poor correlation between the radiological observation and the clinical outcome, a large discrepancy between the clinical observations and how the pathology is exhibited on brain images, something which is known as the clinical-radiological paradox (CRP). One of the hypotheses is that the clinical deficit may be more related to the spinal cord damage than the number or location of lesions in the brain. The prevalence of spinal cord abnormalities is about 74-85% and can reach up to 90% of patients with definite MS. These differences across patients can be explained by variations of the imaging technique, clinical analysis and the MS patients group. For CIS patients, the rate of lesions in spinal cord is around 30-40% (Lycklama et al., 2003; Wheeler-Kingshott et al., 2014). It is now accepted that for 5% of MS patients, there is a value to an additional spinal cord MRI when brain MRI is normal (Thorpe et al., 1996).

One of the potential improvements in our understanding of the pathology is using advanced quantitative MRI as well as investigate the extent of tissue damage in the cervical spinal cord (Barkhof, 2002). Focal lesions are visible and detectable on conventional MRI (T1- and T2-weighted). But, diffusion MRI is known to provide quantitative information about tissue microstructure *in vivo* and figures of neuronal degeneration and axonal loss, in the brain as well as in the spinal cord (Clark et al., 2000).

Over the past decade, several groups started working on the improvement of MRI techniques for the spinal cord (Cohen-Adad and Wheeler-Kingshott, 2014). Theses studies involve several metrics extracted from the diffusion MRI measurements as biomarkers of the pathology such as FA, RD, MD, and FWW using DTI or multi-compartment models. However, in general, one can share these studies of involvement of diffusion metrics in two way of investigation: the first way is as we did in the previous Chapter. 5, determination and selection of the best diffusion metrics that characterize MS lesions using anatomical data sets as a *gold-standard* and radiological reference. The second way is to perform longitudinal study to check the temporal evolution of MS pathology between two diffusion MRI acquisitions, at baseline time and after such specific period. Few longitudinal diffusion MRI studies have been performed in MS patients (Caramia et al., 2002; Agosta et al., 2007a; Oreja-Guevara et al., 2005; Théaudin et al., 2012). The objective of longitudinal follow-up is to show correspondence between lesions progression in the MR images and the evolution of the EDSS score.

In this chapter, we propose to study the EMISEP cohort and provide quantitative figures of pathology evolution between M0 and M12 in the cervical spine, exhibiting how the pathology damage spans in the cervical spinal cord. We first investigate how reproducible diffusion metrics are for each vertebral level in the cervical spine, using a test-retest dataset on a group of 8 healthy subjects. Then, based on the test re-test quantitative calibration, we compute these measures on a group of 31 MS patients, and follow their longitudinal evolution between baseline and follow-up 12 months later.

6.2 Data acquisition

Data were acquired on 3T scanners at one site in Rennes in France, please refer to Chapter 4 for a complete description of the imaging protocol.

6.2.1 MS Patients and healthy volunteers

8 healthy volunteers (4 females, 4 males, median age 31 years, range 21-35) and 31 MS patients (21 females, 10 males, median age 30 years, range 20-49) were recruited in the study approved by the local research ethics committee. All participants provided informed written consent.

6.2.2 MRI Acquisition

MS patients and healthy volunteers were scanned on a 3T Siemens Verio scanner. Each subject was scanned twice with the same acquisition protocol. For MS patients, the second acquisition was performed within 12 months of the first one, however for healthy volunteers both acquisitions were performed few minutes apart with new reposition.

Thirty non-collinear diffusion-weighted images (DWI) were acquired at $b = 900$ s·mm^{-2}, six non-DWI ($b = 0$) measurements and one non-DWI ($b = 0$) with an opposite phase encoding direction (PED) were also acquired. Scans were performed in sagittal orientation and head-feet (H-F) PED. The pulse sequence used for diffusion MRI is echo planar imaging (EPI). The reduced-FOV (field-of-view) technique was employed to reduce sensitivity of EPI to susceptibility artifacts. Sixteen slices were acquired with the following parameters without inter-slice gap: TR/TE = 3600/90 ms, with 2x2x2 mm^3 as the resolution, and image matrix 80x80. The total acquisition time for the dMRI sequence was approximately 7 minutes.

The protocol also includes high-resolution T_1-weighted image for anatomical reference with an isotropic 1x1x1 mm^3 resolution.

6.2.3 EDSS score and the appearance of new lesion

In the context of the EMISEP project, the lesions in the brain of each MS patient were segmented at the baseline M0 on Fluid-attenuated inversion recovery (FLAIR) MRI sequence. Besides, the number and localization of new lesion appeared in spinal cord at M12 were annotated after segmentation on sagital T_2*-weighted. In addition, The Kurtzke Expanded Disability Status Scale (EDSS) scores at M0 and M12 were provided. The EDSS is based on a neurological examination by a clinician by assigning a score in eight functional systems such as sensory and visual (Kurtzke, 1983). Table. 6.1 summarizes the MS patients in this group with most noticeable evolution (EDSS change or new lesions).

Patient	EDSS M0	EDSS M12	Nb new lesion in SC	Nb lesion in brain M0
MS Patient08-04	1	1	1 in C3	1
MS Patient08-06	0	0	1 in C4-C5	0
MS Patient08-10	0	3	2 in C2-C3	3
MS Patient08-28	0	1	0	4
MS Patient08-39	0	1	1 in C1	0
MS Patient08-61	1.5	2.5	0	0
MS Patient08-62	2	2.5	0	2
MS Patient08-79	0	2	0	0

Table 6.1: Evolution of EDSS score between baseline M0 and 12-months M12 follow-up. The 4th column presents the number of new lesions in spinal cord at M12. The 5th column presents the number of lesions in brain at baseline M0. Boxcolors mean MS patients with EDSS increase, with New lesion in SC at M12 and with EDSS increase + New lesion in SC at M12.

6.3 Methods

We preprocess data in this chapter as we did in Chapter 5: motion correction using SCT, distortion correction using HySCO, segmentation of the cord on T_1-weighted and DWI mean, manual identification of two vertebral level, C3 and T1, as a requirement information for registering to PAM50 template, registration of PAM50-T1 registered to DWI mean data and finally computing and quantifying DTI and Ball&Stick metrics for each vertebral level of the cervical part. We summarize in Figure.6.1 the processing pipeline. Here we only computed metrics that have significant difference between MS patients and healthy volunteers in Table.5.5 as found in Chapter 5: FWW, Stick-AD, FA, MD and RD.

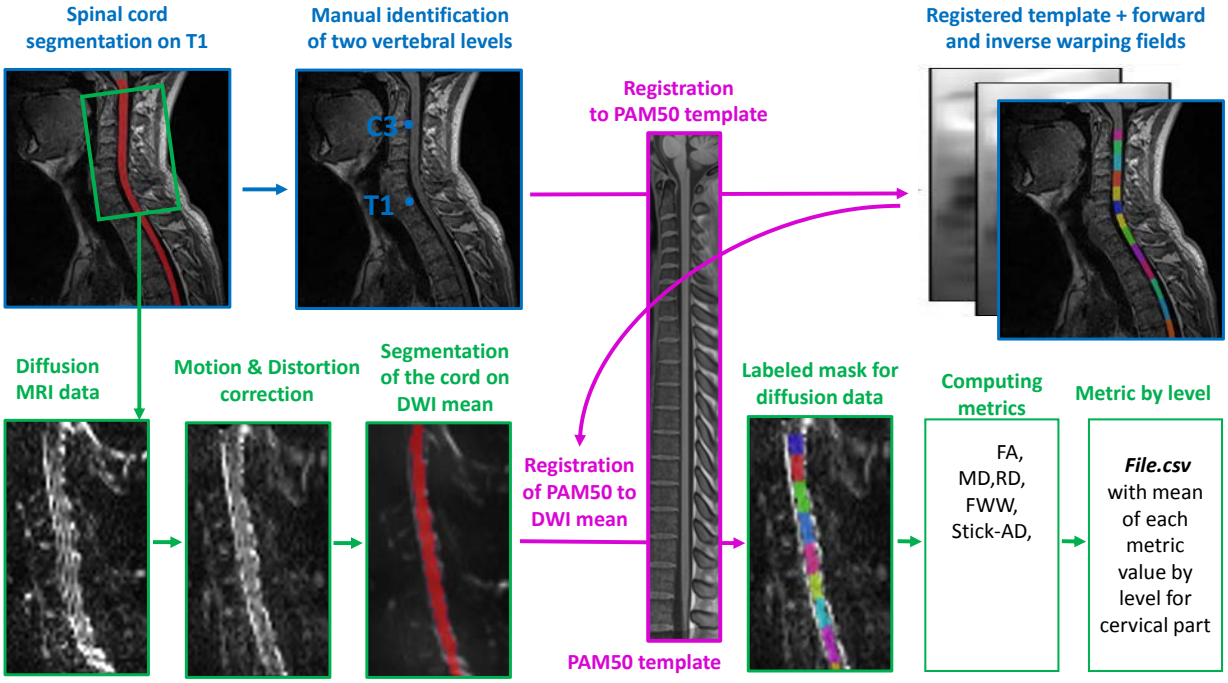

Figure 6.1: Illustration of the automated analysis pipeline. (1) Segmentation of the cord on T1. (2) Manual identification of two vertebral levels. (3) Registration to the PAM50 template. (4) Motion and distortion correction of dMRI data. (5) Segmentation of the cord using DWI mean data. (6) Registration of PAM50-T1 registered to DWI mean data using the inverse warping field from previous registration as an initial warping field. (7) Computing DTI and Ball&Stick metrics. (8) Quantification of metrics by vertebral level of the cervical part.

6.4 Results

6.4.1 Inter-subject and intra-subject variability

In Figure.6.2, we show boxplots representation of each metric for scan (s) and re-scan (r) of the 8 healthy volunteers. Table 6.2 shows the standard deviation of difference between scan and re-scan for each level, and standard deviation of scan and re-scan each metric averaged on each vertebral level. Figure.6.2 and Table 6.2 demonstrate that the variance inter-scan and re-scan is inconstant especially for C1, C6 and C7. Also, the inter-subject variance is not constant. For some metric, the variance is higher in C7, C5 or C1. This can be explained by the fact that larger distortions

	Levels						
Metrics	C1	C2	C3	C4	C5	C6	C7
STD of difference between scan and re-scan (multiplied by 1000)							
FWW	59.41	45.09	36.01	54.21	29.73	77.35	102.61
Stick-AD	0.09	0.16	0.15	0.20	0.21	0.24	0.26
FA	81.79	39.73	54.59	59.08	56.74	43.84	62.14
MD	0.19	0.12	0.09	0.12	0.09	0.10	0.19
RD	0.18	0.11	0.12	0.13	0.09	0.10	0.13
STD for both of scan and re-scan (multiplied by 1000)							
FWW	72.56	40.82	44.64	50.64	78.85	128.77	134.30
Stick AD	0.15	0.21	0.14	0.14	0.11	0.14	0.15
FA	79.76	52.86	47.43	48.23	83.35	117.92	118.16
MD	0.15	0.12	0.08	0.08	0.11	0.15	0.18
RD	0.16	0.10	0.10	0.09	0.13	0.18	0.19

Table 6.2: Standard Deviation of difference between scan and re-scan, and Standard Deviation of scan and re-scan (multiplied by 1000) of DTI and Ball-and-Stick metrics averaged on each vertebral level. Diffusivities are measured in mm^2/s.

are observed in images at the top and the bottom of the field of view. In Figure.6.3, which shows boxplots representation of each metric for scan M0 and M12 of the 31 MS patietns, we remark by a visual inspection that the variance inter-scan re-scan and inter-subject is more stable.

Otherwise, in previous Chapter. 5, we performed a two-way analysis of variance between vertebrae levels of 29 healthy volunteers for each metric to illustrate the interaction term between them. Table. 5.4 summarizes intervals of vertebral levels in which there is no significance difference. We remarked that for all metrics, even just the selected five one in this Chapter, the [C2,C4] interval shows no significance difference which leads to the possibility of merging metrics quantified in C2, C3 and C4 vertebral levels.

However, in such reproducibility study, the absence of significance difference of variance between vertebral levels is not as critical as in the previous chapter. In this part of work, if we merge vertebral levels, we will likely increase the overall variance and we will be stricter in our Bland-Altman diagram. Thus we propose to merge all cervical levels from C1 to C7.

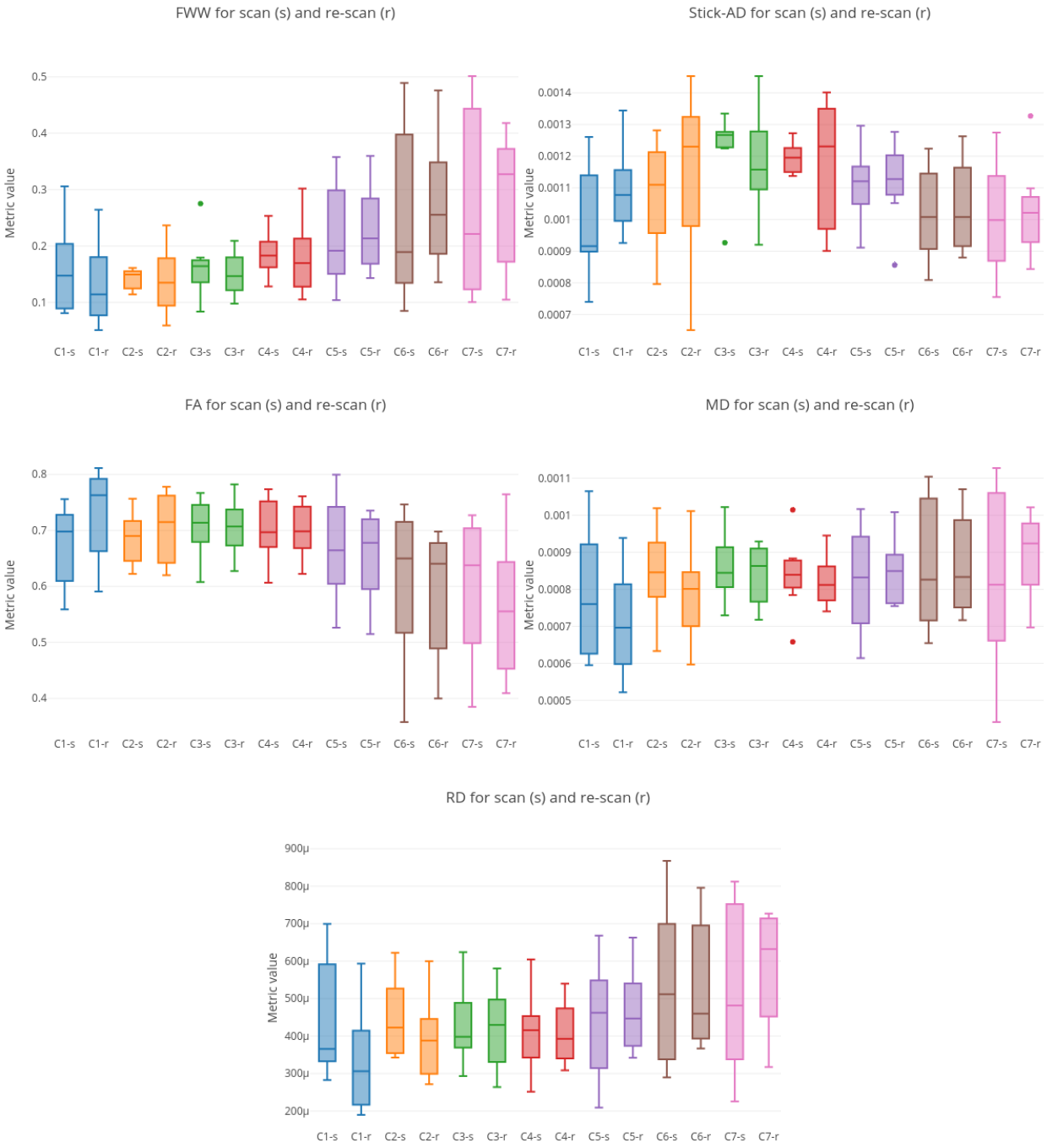

Figure 6.2: Distribution of FWW, Stick-AD, FA, MD and RD for healthy volunteers at scan (s) and re-scan.

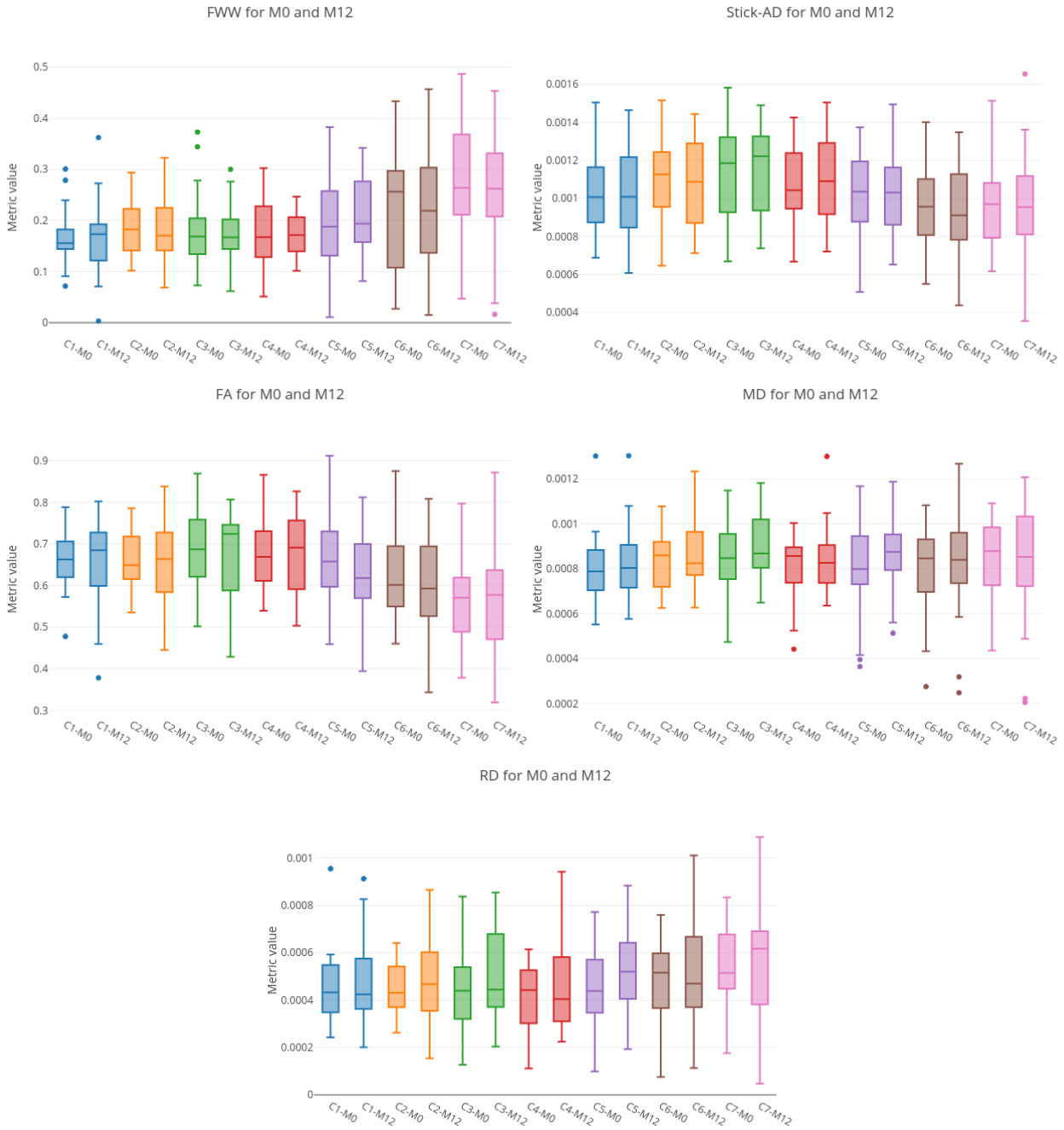

Figure 6.3: Distribution of FWW, Stick-AD, FA, MD and RD for MS patients at M0 and M12.

6.4.2 Bland-Altman analysis

The reproducibility of the DTI and Ball-and-Stick metrics for white matter on healthy volunteers were assessed and visualized using Bland-Altman (Bland and Altman, 1986). The Bland-Altman plots were computed on the 8 healthy volunteers $\times$ 7 levels for each metric. For this analysis, the computed average of each metric within each vertebral level gives a single data point for every metric, cervical level of every subject and scan. The solid blue line represents the average difference between re-scan (scan2) and scan (scan1) and the dashed blue lines indicate the 95% confidence interval (CI). These Bland-Altman plots, presented in Figure.6.4, defines confidence intervals for each metrics. We overlaid on these Bland-Altman plots in red color corresponding

values for MS patients, which allows identification of significant evolution of a given metric in a given vertebral level between scan and rescan for each MS patient. In Figure.6.4, we can therefore identify significant longitudinal evolution of diffusion-based measures between baseline (M0) and 12 months follow-up (M12).

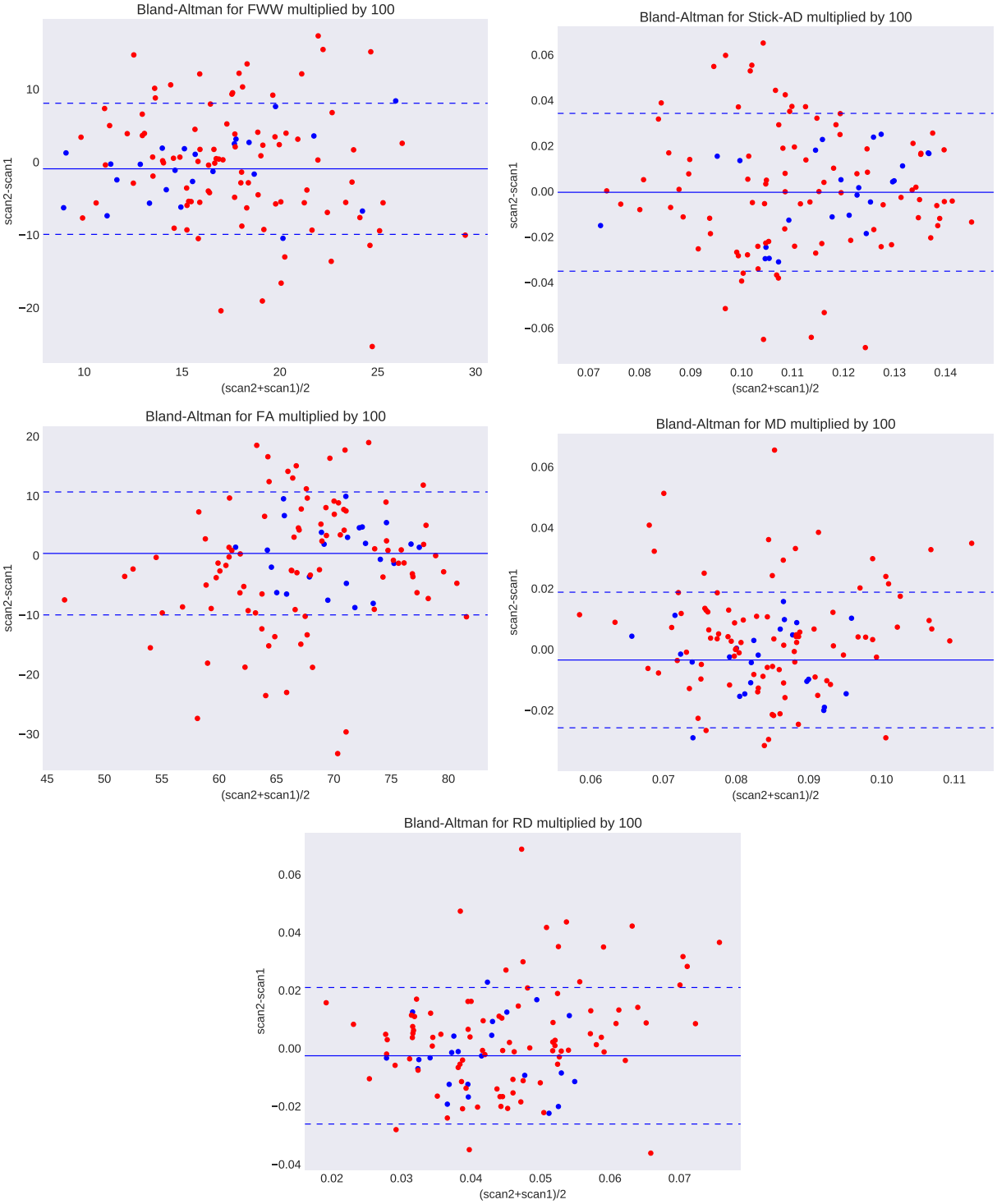

Figure 6.4: Blue: Bland-Altman plot for healthy volunteers (scan and re-scan) for chosen metrics. Associated confidence interval is represented by the dashed lines. Red: overlaid metrics difference Scan(M12)-Scan(M0) for MS patients; data points falling outside the 95% confidence interval correspond to significant evolution between M0 and M12.

6.4.3 Patient-based longitudinal evolution

Detailed results of the significant longitudinal evolution (SLE) are reported on Table 6.3 for specific patients, for which several metrics show significant evolution between M0 and M12. In Table 6.3, we reported patients for which at least three diffusion metrics evolved significantly between M0 and M12, with respect to the confidence intervals reported in Figure.6.4.

Note that we consider SLE in M12 compared to M0, when FWW, MD and RD increase, Stick-AD and FA decreases. In Chapter. 5, we deduced that from all combinations, the combinations [RD,MD,FA] and [FWW,Stick-AD,MD,RD] give the best score of prediction between healthy volunteers and MS patients with lesion. Thus, in Table 6.3, we present all MS patients by each vertebral level that have SLE for [RD,MD,FA] and [FWW,Stick-AD,MD,RD], for 4 and 3 from the computed five metrics.

Out of the 8 MS patients presented in Table. 6.1, which having new lesion in spinal cord or increased EDSS score, 6 patients stand out in the Bland-Altman analysis:

Patient08-04 [C1-C5] levels have SLE on [RD,MD,FA], {C1,C4,C5} have SLE on 4 metrics and {C2,C3,C6} have SLE on 3 metrics. This patient has a lesion in C3. So, C3 which contains a lesion has SLE on [RD,MD,FA]

Patient08-10 [C3-C6] levels have SLE on [RD,MD,FA], {C3,C5} have SLE on 4 metrics and {C4,C6} have SLE on 3 metrics. This patient has two lesions in [C2-C3] and EDSS score which reach up from 0 to 3. So, C3 has SLE on [RD,MD,FA] and a another combination of 4 metrics.

Patient08-28 {C6} and {C7} have SLE on 4 and 3 metrics respectively. This patient has an EDSS score which reach up to 1 on M12.

Patient08-39 {C1,C3} have SLE on 3 metrics. This patient has a lesion in C1 and an EDSS score which reach up to 1 on M12. So

Patient08-61 {C7} have SLE on 3 metrics. This patient has an EDSS score which reach up from 1.5 to 2.5 on M12.

Patient08-79 [C5-C7] levels have SLE on [RD,MD,FA], [C5-C7] have SLE on 4 metrics. This patient has an EDSS score which reach up from 0 to 2 on M12.

We note the absence in Bland-Altman analysis of two patients: **Patient08-06** which has a lesion shared in [C4-C5] and **Patient08-62** which has an EDSS score reach up slightly from 2 to 2.5 on M12 but with two lesions in brain in M0. The sensitivity of this technique is therefore relatively good.

In the other hand, we also note several that MS patients, with neither increase in EDSS score nor new appearance of lesion in spinal cord, appear to have SLE in the diffusion metrics. Out of the 30 vertebral levels of MS patients that have SLE, this is the case for 12 vertebral levels of 7 subjects. This is a relatively good specificity, though, and to find a possible explanation of these false positive, we present in Table. 6.4 additional data about these patients.

Patient08-01 {C7} have SLE on [RD,MD,FA] with a constant EDSS score at 1 and without lesion in brain.

Patient08-03 and Patient08-67 have SLE on [FA,MD,RD] in {C2} and {C4} respectively. These two patients have 0 as EDSS score in M0 and M12 and without any lesion in brain in M0.

Patient08-16 {C6} have SLE on 4 metrics, **Patient08-71**: {C6,C7} have SLE on 4 metrics, **Patient08-74**: {C7} have SLE on [RD,MD,FA]. These three patients have a constant EDSS score, 1, 1.5 and 0 respectively. However, all of them possess 4, 6 and 1 lesions in brain at M0 respectively.

Patient08-35 {C1,C2} have SLE on 3 metrics and {C5,C6,C7} have SLE on [FA,MD,RD]. This patient has a special case with a decrease EDSS score

Subjects have SLE on [FA,MD,RD]				
Patient08-01-C7	Patient08-03-C2	Patient08-04-C1	Patient08-04-C2	Patient08-04-C3
Patient08-04-C4	Patient08-04-C5	Patient08-16-C6	Patient08-10-C3	Patient08-10-C4
Patient08-10-C5	Patient08-10-C6	Patient08-35-C5	Patient08-35-C6	Patient08-35-C7
Patient08-71-C7	Patient08-71-C6	Patient08-74-C7	Patient08-79-C5	Patient08-79-C6
Patient08-79-C7				

Subjects have SLE on [FWW, Stick-AD, MD,RD]
Any Patient

Subjects have SLE on 4 metrics from FWW, Stick-AD, FA, MD,RD				
Patient08-01-C7	Patient08-04-C1	Patient08-04-C5	Patient08-04-C4	Patient08-10-C5
Patient08-10-C3	Patient08-16-C6	Patient08-28-C6	Patient08-35-C5	Patient08-35-C6
Patient08-35-C7	Patient08-71-C7	Patient08-71-C6	Patient08-74-C7	Patient08-79-C5
Patient08-79-C6	Patient08-79-C7			

Subjects have SLE on 3 metrics from FWW, Stick-AD, FA, MD,RD				
Patient08-03-C2	Patient08-04-C2	Patient08-04-C3	Patient08-04-C6	Patient08-39-C3
Patient08-39-C1	Patient08-67-C4	Patient08-35-C2	Patient08-35-C1	Patient08-10-C6
Patient08-10-C4	Patient08-28-C7	Paient08-61-C7		

Table 6.3: MS patients with significant longitudinal evolution (SLE) for several metrics conjointly. Boxcolors means MS patients with EDSS increase, with New lesion in M12 and with EDSS increase + New lesion in M12

Patient	EDSS M0	EDSS M12	Nb new lesion in SC	Nb lesion in brain M0
MS Patient08-01	1	1	0	0
MS Patient08-03	0	0	0	0
MS Patient08-16	1	1	0	4
MS Patient08-35	1	0	0	0
MS Patient08-67	0	0	0	0
MS Patient08-71	1.5	1.5	0	6
MS Patient08-74	0	0	0	1

Table 6.4: Evolution of EDSS score between baseline M0 and 12-months M12 follow-up. The 4th column presents the number of new lesions in spinal cord at M12. The 5th column presents the number of lesions in brain at baseline M0.

6.5 Discussion and conclusion

In this work, we proposed a framework for studying the evolution of microstructure-related parameters measured with diffusion MRI in the spinal cord white matter of MS patients. Based on a group of 8 healthy controls, we were able to define confidence intervals for diffusion-based metrics for vertebral levels in the cervical spine. Our work includes a definition of confidence intervals for cervical vertebral levels. Using these confidence intervals, we can follow the longitudinal evolution of the same metrics for each patient, and identify abnormal trajectories associated with the pathology. In this Bland Altman analysis, we were strict in two ways: by merging all vertebral levels, we potentially increase the confidence intervals; second, we considered longitudinal evolution to be significant if at least 3 relevant diffusion metrics were affected in a vertebral level. These metrics, FWW, Stick-AD, FA, MD and RD showed a significant difference between vertebral levels of healthy controls and MS patients in Chapter 5.

In the Bland Atlman analysis done on 31 MS patients $\times$ 7 vertebral levels, there are 30 vertebral levels with significant longitudinal evolution, out of which 18 (60%) correspond to disability changes or the appearance of new lesion. For the rest, the 12 vertebral levels, 5 have a decreased EDSS score, 3 have a constant 0 or 1 EDSS score and 4 have already lesions in brain at baseline M0.

In terms of patient, our reproducibility test found 13 MS patients with significant longitudinal evolution in at least one vertebral level, only 5 (38%) have increased EDSS score, 3 (23%) have new lesion in spinal cord in M12, 3 (23%) have already a lesion in brain in M0. Bland Altman analysis succeeded in detecting 5 patients from 6 (83%) that have an increased EDSS score between M0 and M12. In addition, this analysis succeeded also in detecting 3 patients out of 4 (75%) that have the appearance of new lesion in the cervical part of spinal cord. Otherwise, one can explain the failed outputs of our reproducibility analysis by the fact that larger distortions are observed in images at the top and the bottom of the field of view.

Another important issue to be addressed is that the comparison metrics based on DTI and Ball-and-Stick suggests that both models provide complementary information. Some for MS patients, we validate the significant longitudinal evolution and its correlation by such changes over times only if we include and merge both of these metrics.

Recently, an increased studies that interested to apply advanced reconstruction models for diffusion MRI data in human spinal cord in vivo. This suggests that even for clinical data, multi-compartment models provide novel information about the evolution of tissue microstructure, and should be included in the processing workflow. To our knowledge, only neurite orientation dispersion and density imaging (NODDI) the multi-compartmental diffusion models have been used to measure and investigate microstructure and characterizing abnormalties on MS patients (By et al., 2017). However, in this study, only one slice of cervical spine was acquired in order to investigate the sensitivity and feasibility of NODDI in patients with MS.

To conclude, we showed a significant correlation of cord diffusion MRI measures with disability changes over time at the scale of 83%, and with the appearance of new lesion in spinal cord at 75% scale. Furthermore, we found other correspondence of these diffusion metrics with the presence of lesion in the brain at M0 even the EDSS score is constant over time. Further studies with more scan rescan data of healthy volunteers are required to investigate and validate more how the evolution of diffusion MRI indices correlate with clinical scores.

Chapter 7

Conclusion

Contents

7.1 Contributions summary

In the following, we summarize the major contributions of this thesis.

7.1.1 Distortion correction of diffusion MRI

We have proposed a new geometric based metrics and framework for studying the impact of distortion correction in diffusion MRI of the spinal cord. Based on the assumption that the distortion only affects the apparent shape of spine and not the direction of tensor, we proposed two novel statistics which take into account the alignment of the diffusion tensor with the apparent centerline of the spinal cord. This geometric evaluation was conducted on 95 scans to compare four distortion correction methods: Block-Matching (BM) (Hedouin et al., 2017), Hyper-elastic Susceptibility artefact correction (HySCO) (Ruthotto et al., 2012), TOPUP (Andersson et al., 2003) and Voss (Voss et al., 2006).

The fragmentation by levels of the spine shows the different impact of distortion between edges (C1, C2, T1, T2) and center (C3,C4) of the imaging window. This local evaluation provides a performance measure complementary to classical comparison with a reference anatomical image. This work led to several publications including in international peer-reviewed conferences:

Comparison of inhomogeneity distortion correction methods in diffusion MRI of the spinal cord.
Haykel Snoussi, Emmanuel Caruyer, Olivier Commowick, Elise Bannier, Anne Kerbrat, Christian Barillot.
In ESMRMB-34th Annual Scientific Meeting European Society for Magnetic Resonance in Medecine and Biology, Barcelona, Spain, 2017, October.

Geometric evaluation of distortion correction methods in diffusion MRI of the spinal cord.
Haykel Snoussi, Emmanuel Caruyer, Julien Cohen-Adad, Olivier Commowick, Benoit Combes, Elise Bannier, Anne Kerbrat, Christian Barillot.
In IEEE International Symposium on Biomedical Imaging (ISBI), Venice, Italy, 2019, April.

In addition, a journal version of this work is under preparation for submission.

Distortion correction in diffusion MRI of the spinal cord : Evaluation and impact.
Haykel Snoussi, Emmanuel Caruyer, Julien Cohen-Adad, Olivier Commowick, Benoit Combes, Elise Bannier, Anne Kerbrat, Christian Barillot.

7.1.2 Characterization of Multiple Sclerosis Abnormalities within the Cervical Spinal Cord

In this chapter.we have proposed a pipeline to extract average dMRI metrics per vertebral level in spinal cord and we performed a statistical analysis to show their sensitivity associated with the presence and evolution of MS lesions within the same vertebral level. Diffusion measures involved are extracted from the diffusion tensor and the ball-and-stick models.

We show that FWW, Stick-AD, FA, MD and RD have a significant difference between healthy volunteers and MS patients within [C2-C4] region in cervical spinal cord. In regards to FA, MD and RD, there are already showed in other studies involved in spinal cord (Valsasina et al., 2005; Agosta et al., 2007a; Agosta et al., 2007b; von Meyenburg et al., 2013).

Our workflow have many additions regarding other studies that involved in spinal cord; relatively large data, 9 raters including radiologists and experienced readers how are segment MS

lesions, quantification of diffusion measures using atlas approach which is free from manual delineation bias and during metric extraction partial volume effect is accounted for, and the quality check of each step of the pipeline in order to guarantee good quality of the analysis and the accuracy of the results. We show that the B&S multi-compartment model can provide novel information about the evolution of tissue microstructure within MS patients, and should be included in the processing workflow and clinical protocol.

Furthermore, another important contribution is the way that we proposed, multivariate learning, to use the diffusion MRI data to automatically detect the presence of a MS lesion. Based on a selection of metrics extracted from diffusion, we learned a linear classifier using linear discriminant analysis (LDA) and we reduced the dimension of the feature vector using two different strategies; (1) select manually a set of measures with limited cross-correlation, (2) perform a principal component analysis (PCA) and then learn a linear classifier on the reduced set of PCA, first two components which explain more than 65% of the variance. Throughout these strategies, we evaluated the classification results using the area under the curve (AUC) of the receiver operating characteristic curve (ROC). We found that combining some metrics reaches up the prediction score of such MS lesion and more performing than using each metric independently. We showed that a combination of 3 metrics [FA, MD, RD] and a combination of 4 metrics [FWW,MD,StickAD,RD] give the better ROC AUC score between healthy volunteers and MS patients with lesion. Thus, choosing a subset of metrics which bring complementary information has significantly increased the prediction score of the presence of this disease.

In this context, one publication is under preparation for submission to a peer-reviewed international journal:

Characterization of Multiple Sclerosis Abnormalities within the Cervical Spinal Cord
Haykel Snoussi, Emmanuel Caruyer, Julien Cohen-Adad, Olivier Commowick, Benoit Combes, Elise Bannier, Anne Kerbrat, Christian Barillot.

7.1.3 Reproducibility and Evolution of Diffusion MRI Measurements within the Cervical Spinal Cord in Multiple Sclerosis

In this chapter, we proposed a framework for studying the evolution of microstructure-related parameters measured with diffusion MRI in the spinal cord white matter of MS patients. Based on a group of 8 healthy controls, we were able to define confidence intervals for diffusion-based metrics for vertebral levels in the cervical spine using Bland Altman analysis. Our work include a definition of confidence intervals for cervical vertebral levels. Using these confidence intervals, we followed the longitudinal evolution of the same metrics for each patient, and identify abnormal trajectories associated with the pathology.

We showed a significant correlation of cord diffusion MRI measures with disability changes over time at the scale of 83%, and with the appearance of new lesion in spinal cord at 75% scale. Furthermore, we found other correlation of these diffusion metrics with the presence of lesion in the brain at M0 despite the EDSS score is constant over time. However, there is some incomprehensible correlations with such patients; one have only constant EDSS score at 1 and other her score reach down to 0 at M12. Further studies with more scan rescan data of healthy volunteers are required to investigate and validate more how the evolution of diffusion MRI indices correlate with clinical scores.

7.2 Perspectives

In Chapter.4, we have proposed novel geometric based metrics and framework for studying the impact of distortion correction in diffusion MRI of the spinal cord. One perspective can introduce these geometric metric to such method of distortion correction as a registration or converging criteria. We showed that 'classic' metrics such cross-correaltion and mutual information are not sufficient to evaluate the correction of distortions. In addition, using diffusion MRI acquired in sagittal way with Head-Feet (HF-FH) PED, we show that distortion is limited only for extremes of FOV, especially those in PED. The extremes of FOV in HF-FH contain brain stem, C1, C2 and C7, T1 and T2. However, acquisition in Anterior-Posterior (AP-PA) PED, the extremes of FOV will be empty but the acquisition will hampered by more distortion as result of perpendicular inhomogeneity field depending the size of matrix. One interest perpective of our work is to apply the current evaluation of distortion correction and compare between them.

In Chapter.5, we demonstrate the sensitivity of FWW and Stick-AD, as metrics from a two-components model, with the damage of MS lesion in spinal cord. Thus Ball-and-Stick multi-compartment model can provide novel information about the evolution of tissue microstructure, and should be included in the processing workflow and clinical protocol despite the technical challenge of acquiring scan in spinal cord. To do so, we have to propose and use other diffusion MRI protocol that permit the application of other complicated multi compartment models.

In Chapter.6, we showed a significant correlation of cord diffusion MRI measures with disability changes over time at the scale of 83%, and with the appearance of new lesion in spinal cord at 75% scale. However, we found various failed outputs of our reproducibility analysis. Further studies with more scan rescan data of healthy volunteers are required to investigate and validate more how the evolution of diffusion MRI indices correlate with clinical scores.

List of abbreviations

A.	
ACD	Angular concentration of directions
AD	Axial diffusivity
ADC	Apparent diffusion coefficient
AP	Anterior-Posterior
AUC	Area Under the Curve
B.	
BBB	Blood-Brain Barrier
B&S	Ball-and-Stick
BM	Block-Matching
BS	Brain Stem
C.	
CC	Cross-Correlation
CNS	Central Nervous System
CIS	Clinically Isolated Syndrome
CSF	Cerebral Spinal Fluid
CIS	Clinically Isolated Syndromes
CRP	Clinical-radiological paradox
CI	Confidence interval
D.	
dMRI	diffusion Magnetic Resonace Imaging
DWI	Diffusion Weighted Imaging
DTI	Diffusion Tensor Imaging
DSI	Diffusion Spectrum Imaging
E.	
EDSS	Expanded Disability Status Scale
EPI	Echo-Planar Imaging
ESP	Echo-spacing
EMMs	Estimated Marginal Means

F.	
FA	Fractional Anisotropy
FOV	Field of View
FH	Feet-Head
FPR	False-positive rate
FLAIR	Fluid-attenuated inversion recovery
FWW	Free Water Weight

G.	
GM	Gray Matter

H.	
HySCO	Hyper-elastic Susceptibility Artefact Correction
HF	Head-Feet

L.	
LDA	Linear discriminant analysis

M.	
MAD	Mean angle direction
MRI	Magnetic Resonace Imaging
MTR	Magnetization transfer ratio
MD	Mean Diffusivity
MI	Mutual Information

N.	
NAWM	Normal-appearing White Matter
NMR	Nuclear Magnetic Resonance
NODDI	Neurite Orientation Dispersion and Density Imaging

P.	
PNS	Peripheral Nervous System
PPMS	Primary progressive Multiple Sclerosis
PVE	Partial Volume Effect
PED	Phase-encoding Direction
PSF	Point Spread Function
PA	Posterior-Anterior
PCA	Principal component analysis

Q.	
qMRI	quantitative MRI
QBI	Q-Ball Imaging
QSI	Q-Space Imaging
QC	Quality Control

R.	
RRMS	Relapsing-remitting Multiple Sclerosis
ROI	Region Of Interest
RD	Radial diffusivity
RGP	Reversed Gradient Polarity
ROI	Region of Interest
ROC	Receiver Operating Characteristic

S.	
SPMS	Secondary Progressive Multiple Sclerosis
SPM	Statistical Parametric Mapping
SCT	Spinal Cord Toolbox
SNR	Signal-Noise Ratio
ss-EPI	single-shot Echo-Planar Imaging
Stick-AD	Stick Axial Diffusivity
SLE	Significant longitudinal evolution

T.	
TE	Echo Ttime
TPR	True-positive rate
TR	Repetition Time

W.	
WM	White Matter

List of Figures

List of Tables

List of Algorithms

Bibliography

Abdel-Aziz, K. and Ciccarelli, O. (2014). Rationale for quantitative mri of the human spinal cord and clinical applications. In *Quantitative MRI of the Spinal Cord*, pages 3–21. Elsevier.

Agosta, F., Absinta, M., Sormani, M., Ghezzi, A., Bertolotto, A., Montanari, E., Comi, G., and Filippi, M. (2007a). In vivo assessment of cervical cord damage in ms patients: a longitudinal diffusion tensor mri study. *Brain*, 130(8):2211–2219.

Agosta, F., Pagani, E., Caputo, D., and Filippi, M. (2007b). Associations between cervical cord gray matter damage and disability in patients with multiple sclerosis. *Archives of neurology*, 64(9):1302–1305.

Alexander, A. L., Hasan, K. M., Lazar, M., Tsuruda, J. S., and Parker, D. L. (2001). Analysis of partial volume effects in diffusion-tensor mri. *Magnetic Resonance in Medicine*, 45(5):770–780.

Alexander, D. C. (2005). Multiple-fiber reconstruction algorithms for diffusion mri. *Annals of the New York Academy of Sciences*, 1064(1):113–133.

Amélie, R., Anxionnat, R., Armspach, J.-P., Audoin, B., Barillot, C., Berry, I., Bonneville, F., Boutet, C., Castelnovo, G., Cervenansky, F., Cohen, M., Commowick, O., Cotton, F., De Seze, J., Dousset, V., Durand-Dubief, F., Edan, G., Ferre, J.-C., Galanaud, D., Glattard, T., Grand, S., Guillaumont, J., Guillevin, R., Guttmann, C., Hannoun, S., Heitz, F., Krainik, A., Kremer, S., Labauge, P., Menjot de Champfleur, N., Ranjeva, J.-P., Roch, J.-A., Sappey-Marinier, D., Savatovsky, J., Stankoff, B., Tourdias, T., Tourbah, A., and Vukusic, S. (2015). OFSEP, a nationwide cohort of people with multiple sclerosis: Consensus minimal MRI protocol. *Journal de Neuroradiologie / Journal of Neuroradiology*, 42(3):133 – 140.

Andersson, J. and Skare, S. (2010). Image distortion and its correction in diffusion mri. *Diffusion MRI: Theory, Methods, and Applications. Oxford University Press, Oxford*, pages 285–302.

Andersson, J. L., Skare, S., and Ashburner, J. (2003). How to correct susceptibility distortions in spin-echo echo-planar images: application to diffusion tensor imaging. *Neuroimage*, 20(2):870–888.

Ascherio, A. and Munger, K. L. (2007). Environmental risk factors for multiple sclerosis. part ii: Noninfectious factors. *Annals of Neurology: Official Journal of the American Neurological Association and the Child Neurology Society*, 61(6):504–513.

Avants, B. B., Epstein, C. L., Grossman, M., and Gee, J. C. (2008). Symmetric diffeomorphic image registration with cross-correlation: evaluating automated labeling of elderly and neurodegenerative brain. *Medical image analysis*, 12(1):26–41.

Bammer, R. (2003). Basic principles of diffusion-weighted imaging. *European journal of radiology*, 45(3):169–184.

Bammer, R., Augustin, M., Prokesch, R. W., Stollberger, R., and Fazekas, F. (2002). Diffusion-weighted imaging of the spinal cord: interleaved echo-planar imaging is superior to fast spin-echo. *Journal of Magnetic Resonance Imaging: An Official Journal of the International Society for Magnetic Resonance in Medicine*, 15(4):364–373.

Barker, G. (2001). Diffusion-weighted imaging of the spinal cord and optic nerve. *Journal of the neurological sciences*, 186:S45–S49.

Barkhof, F. (2002). The clinico-radiological paradox in multiple sclerosis revisited. *Current opinion in neurology*, 15(3):239–245.

Basser, P. J., Mattiello, J., and Le Bihan, D. (1994a). Estimation of the effective self-diffusion tensor from the nmr spin echo. *Journal of Magnetic Resonance*, B(103):247–254.

Basser, P. J., Mattiello, J., and Lebihan, D. (1994b). MR Diffusion Tensor Spectroscopy and Imaging. *Biophysical Journal*, 66:259–267.

Behrens, T., Berg, H. J., Jbabdi, S., Rushworth, M., and Woolrich, M. (2007). Probabilistic diffusion tractography with multiple fibre orientations: What can we gain? *Neuroimage*, 34(1):144–155.

Behrens, T. E., Woolrich, M. W., Jenkinson, M., Johansen-Berg, H., Nunes, R. G., Clare, S., Matthews, P. M., Brady, J. M., and Smith, S. M. (2003). Characterization and propagation of uncertainty in diffusion-weighted mr imaging. *Magnetic Resonance in Medicine: An Official Journal of the International Society for Magnetic Resonance in Medicine*, 50(5):1077–1088.

Bland, J. M. and Altman, D. (1986). Statistical methods for assessing agreement between two methods of clinical measurement. *The lancet*, 327(8476):307–310.

Bloch, F. (1946). Nuclear induction. *Physical Review*, 70:460–474.

Brown, R. (1828). Xxvii. a brief account of microscopical observations made in the months of june, july and august 1827, on the particles contained in the pollen of plants; and on the general existence of active molecules in organic and inorganic bodies. *The Philosophical Magazine, or Annals of Chemistry, Mathematics, Astronomy, Natural History and General Science*, 4(21):161–173.

By, S., Xu, J., Box, B. A., Bagnato, F. R., and Smith, S. A. (2017). Application and evaluation of noddi in the cervical spinal cord of multiple sclerosis patients. *NeuroImage: Clinical*, 15:333–342.

Caan, M. W. (2016). Dti analysis methods: fibre tracking and connectivity. In *Diffusion Tensor Imaging*, pages 205–228. Springer.

Caramia, F., Pantano, P., Di Legge, S., Piattella, M. C., Lenzi, D., Paolillo, A., Nucciarelli, W., Lenzi, G. L., Bozzao, L., and Pozzilli, C. (2002). A longitudinal study of mr diffusion changes in normal appearing white matter of patients with early multiple sclerosis. *Magnetic resonance imaging*, 20(5):383–388.

Carr, H. Y. and Purcell, E. M. (1954). Effects of diffusion on free precession in nuclear magnetic resonance experiments. *Physical review*, 94(3):630.

Cercignani, M. and Horsfield, M. A. (2001). The physical basis of diffusion-weighted mri. *Journal of the neurological sciences*, 186:S11–S14.

Chang, H. and Fitzpatrick, J. M. (1992). A technique for accurate magnetic resonance imaging in the presence of field inhomogeneities. *IEEE Transactions on medical imaging*, 11(3):319–329.

Chenevert, T. L., Brunberg, J. A., and Pipe, J. G. (1990). Anisotropic diffusion in human white matter: demonstration with mr techniques in vivo. *Radiology*, 177(2):401–405.

Ciccarelli, O., Wheeler-Kingshott, C., McLean, M., Cercignani, M., Wimpey, K., Miller, D., and Thompson, A. (2007). Spinal cord spectroscopy and diffusion-based tractography to assess acute disability in multiple sclerosis. *Brain*, 130(8):2220–2231.

Clark, C. A., Werring, D. J., and Miller, D. H. (2000). Diffusion imaging of the spinal cord in vivo: estimation of the principal diffusivities and application to multiple sclerosis. *Magnetic resonance in medicine*, 43(1):133–138.

Cohen-Adad, J., Benali, H., Hoge, R. D., and Rossignol, S. (2008a). In vivo dti of the healthy and injured cat spinal cord at high spatial and angular resolution. *Neuroimage*, 40(2):685–697.

Cohen-Adad, J., Descoteaux, M., Rossignol, S., Hoge, R. D., Deriche, R., and Benali, H. (2008b). Detection of multiple pathways in the spinal cord using q-ball imaging. *Neuroimage*, 42(2):739–749.

Cohen-Adad, J., Lundell, H., and Rossignol, S. (2009). Distortion correction in spinal cord dti: what's the best approach. In *Proceedings of the 17th Annual Meeting of ISMRM, Honolulu, USA*, volume 3178.

Cohen-Adad, J. and Wheeler-Kingshott, C. (2014). *Quantitative MRI of the spinal cord*. Academic Press.

Commowick, O., Wiest-Daesslé, N., and Prima, S. (2012). Automated diffeomorphic registration of anatomical structures with rigid parts: Application to dynamic cervical mri. In *International Conference on Medical Image Computing and Computer-Assisted Intervention*, pages 163–170. Springer.

Compston, A. and Coles, A. (2008). Multiple sclerosis. *The Lancet*, 372:1502–1517.

Cook, P., Bai, Y., Nedjati-Gilani, S., Seunarine, K., Hall, M., Parker, G., and Alexander, D. C. (2006). Camino: open-source diffusion-mri reconstruction and processing. In *14th scientific meeting of the international society for magnetic resonance in medicine*, volume 2759, page 2759. Seattle WA, USA.

De Leener, B., Cohen-Adad, J., and Kadoury, S. (2015). Automatic segmentation of the spinal cord and spinal canal coupled with vertebral labeling. *IEEE transactions on medical imaging*, 34(8):1705–1718.

De Leener, B., Fonov, V. S., Collins, D. L., Callot, V., Stikov, N., and Cohen-Adad, J. (2018). Pam50: Unbiased multimodal template of the brainstem and spinal cord aligned with the icbm152 space. *NeuroImage*, 165:170–179.

De Leener, B., Kadoury, S., and Cohen-Adad, J. (2014). Robust, accurate and fast automatic segmentation of the spinal cord. *Neuroimage*, 98:528–536.

De Leener, B., Lévy, S., Dupont, S. M., Fonov, V. S., Stikov, N., Collins, D. L., Callot, V., and Cohen-Adad, J. (2017). Sct: Spinal cord toolbox, an open-source software for processing spinal cord mri data. *Neuroimage*, 145:24–43.

Eden, D., Gros, C., Badji, A., Dupont, S. M., De Leener, B., Maranzano, J., Zhuoquiong, R., Liu, Y., Granberg, T., Ouellette, R., et al. (2019). Spatial distribution of multiple sclerosis lesions in the cervical spinal cord. *Brain*.

Einstein, A. (1956). *Investigations on the Theory of the Brownian Movement*. Courier Corporation.

Ellingson, B. M., Ulmer, J. L., and Schmit, B. D. (2007a). Gray and white matter delineation in the human spinal cord using diffusion tensor imaging and fuzzy logic. *Academic radiology*, 14(7):847–858.

Ellingson, B. M., Ulmer, J. L., and Schmit, B. D. (2007b). Optimal diffusion tensor indices for imaging the human spinal cord. *Biomedical sciences instrumentation*, 43:128–133.

Fawcett, T. (2006). An introduction to roc analysis. *Pattern recognition letters*, 27(8):861–874.

Fick, A. (1855). V. on liquid diffusion. *The London, Edinburgh, and Dublin Philosophical Magazine and Journal of Science*, 10(63):30–39.

Filippi, M. and Grossman, R. I. (2002). Mri techniques to monitor ms evolution: the present and the future. *Neurology*, 58(8):1147–1153.

Fisher, R. A. (1936). The use of multiple measurements in taxonomic problems. *Annals of eugenics*, 7(2):179–188.

Fonov, V., Troter, A. L., Taso, M., Leener, B. D., Lévêque, G., Benhamou, M., Sdika, M., Benali, H., Pradat, P.-F., Collins, D., Callot, V., and Cohen-Adad, J. (2014). Framework for integrated mri average of the spinal cord white and gray matter: The mni–poly–amu template. *NeuroImage*, 102:817 – 827.

Goto, N. and Otsuka, N. (1997). Development and anatomy of the spinal cord. *Neuropathology*, 17(1):25–31.

Hachinski, V., Iadecola, C., Petersen, R. C., Breteler, M. M., Nyenhuis, D. L., Black, S. E., Powers, W. J., DeCarli, C., Merino, J. G., Kalaria, R. N., et al. (2006). National institute of neurological disorders and stroke–canadian stroke network vascular cognitive impairment harmonization standards. *Stroke*, 37(9):2220–2241.

Hagmann, P., Jonasson, L., Maeder, P., Thiran, J.-P., Wedeen, V. J., and Meuli, R. (2006). Understanding diffusion mr imaging techniques: from scalar diffusion-weighted imaging to diffusion tensor imaging and beyond. *Radiographics*, 26(suppl_1):S205–S223.

Hedouin, R., Commowick, O., Bannier, E., Scherrer, B., Taquet, M., Warfield, S. K., and Barillot, C. (2017). Block-matching distortion correction of echo-planar images with opposite phase encoding directions. *IEEE Trans. Med. Imaging*, 36(5):1106–1115.

Hesseltine, S., Law, M., Babb, J., Rad, M., Lopez, S., Ge, Y., Johnson, G., and Grossman, R. (2006). Diffusion tensor imaging in multiple sclerosis: assessment of regional differences in the axial plane within normal-appearing cervical spinal cord. *American Journal of Neuroradiology*, 27(6):1189–1193.

Holland, D., Kuperman, J. M., and Dale, A. M. (2010). Efficient correction of inhomogeneous static magnetic field-induced distortion in echo planar imaging. *Neuroimage*, 50(1):175–183.

Huang, H., Ceritoglu, C., Li, X., Qiu, A., Miller, M. I., van Zijl, P. C., and Mori, S. (2008). Correction of b0 susceptibility induced distortion in diffusion-weighted images using large-deformation diffeomorphic metric mapping. *Magnetic resonance imaging*, 26(9):1294–1302.

Inglese, M. and Bester, M. (2010). Diffusion imaging in multiple sclerosis: research and clinical implications. *NMR in Biomedicine*, 23(7):865–872.

Jezzard, P. and Balaban, R. S. (1995). Correction for geometric distortion in echo planar images from b0 field variations. *Magnetic resonance in medicine*, 34(1):65–73.

Koch, M. W., Metz, L. M., Agrawal, S. M., and Yong, V. W. (2013). Environmental factors and their regulation of immunity in multiple sclerosis. *Journal of the neurological sciences*, 324(1-2):10–16.

Koriem, K. M. M. (2016). Multiple sclerosis: New insights and trends. *Asian Pacific Journal of Tropical Biomedicine*, 6(5):429–440.

Kulie, T., Groff, A., Redmer, J., Hounshell, J., and Schrager, S. (2009). Vitamin d: an evidence-based review. *J Am Board Fam Med*, 22(6):698–706.

Kurtzke, J. F. (1983). Rating neurologic impairment in multiple sclerosis: an expanded disability status scale (edss). *Neurology*, 33(11):1444–1444.

Le Bihan, D. and Breton, E. (1985). Imagerie de diffusion it in vivo par résonnance magnétique nucléaire. *CR Académie des Sciences*, (301):1109–1112.

Le Bihan, D., Breton, E., Lallemand, D., Grenier, P., Cabanis, E., and Laval-Jeantet, M. (1986). Mr imaging of intravoxel incoherent motions: Application to diffusion and perfusion in neurologic disorders. *Radiology*, 161(2):401–407.

Leener, B. D., Fonov, V. S., Collins, D. L., Callot, V., Stikov, N., and Cohen-Adad, J. (2018). Pam50: Unbiased multimodal template of the brainstem and spinal cord aligned with the icbm152 space. *NeuroImage*, 165:170 – 179.

Lévy, S., Benhamou, M., Naaman, C., Rainville, P., Callot, V., and Cohen-Adad, J. (2015). White matter atlas of the human spinal cord with estimation of partial volume effect. *Neuroimage*, 119:262–271.

Lin, X., Tench, C. R., Evangelou, N., Jaspan, T., and Constantinescu, C. S. (2004). Measurement of spinal cord atrophy in multiple sclerosis. *Journal of Neuroimaging*, 14:20S–26S.

Lundell, H., Barthelemy, D., Biering-Sørensen, F., Cohen-Adad, J., Nielsen, J. B., and Dyrby, T. B. (2013). Fast diffusion tensor imaging and tractography of the whole cervical spinal cord using point spread function corrected echo planar imaging. *Magnetic resonance in medicine*, 69(1):144–149.

Lycklama, G., Thompson, A., Filippi, M., Miller, D., Polman, C., Fazekas, F., and Barkhof, F. (2003). Spinal-cord mri in multiple sclerosis. *The Lancet Neurology*, 2(9):555–562.

Macdonald, J. and Ruthotto, L. (2016). Efficient numerical optimization for susceptibility artifact correction of epi-mri. *arXiv preprint arXiv:1607.00531*.

Marrie, R. A. (2004). Environmental risk factors in multiple sclerosis aetiology. *The Lancet Neurology*, 3(12):709–718.

McClish, D. K. (1989). Analyzing a portion of the roc curve. *Medical Decision Making*, 9(3):190–195.

McRobbie, D. W., Moore, E. A., Graves, M. J., and Prince, M. R. (2017). *MRI from Picture to Proton*. Cambridge university press.

Miller, D., Grossman, R., Reingold, S., and McFarland, H. (1998). The role of magnetic resonance techniques in understanding and managing multiple sclerosis. *Brain: a journal of neurology*, 121(1):3–24.

Miraldi, F., Lopes, F. C. R., Costa, J. V. A., Alves-Leon, S. V., and Gasparetto, E. L. (2013). Diffusion tensor magnetic resonance imaging may show abnormalities in the normal-appearing cervical spinal cord from patients with multiple sclerosis. *Arquivos de neuro-psiquiatria*, 71(9A):580–583.

Modersitzki, J. (2009). *FAIR: flexible algorithms for image registration*, volume 6. SIAM.

Mohammadi, S., Freund, P., Feiweier, T., Curt, A., and Weiskopf, N. (2013). The impact of post-processing on spinal cord diffusion tensor imaging. *Neuroimage*, 70:377–385.

Mori, S. and Van Zijl, P. C. (2002). Fiber tracking: principles and strategies–a technical review. *NMR in Biomedicine: An International Journal Devoted to the Development and Application of Magnetic Resonance In Vivo*, 15(7-8):468–480.

Moseley, M. E., Cohen, Y., Kucharczyk, J., Mintorovitch, J., Asgari, H., Wendland, M., Tsuruda, J., and Norman, D. (1990). Diffusion-weighted mr imaging of anisotropic water diffusion in cat central nervous system. *Radiology*, 176(2):439–445.

Muñoz-Culla, M., Irizar, H., and Otaegui, D. (2013). The genetics of multiple sclerosis: review of current and emerging candidates. *The application of clinical genetics*, 6:63.

Onu, M., Gervai, P., Cohen-Adad, J., Lawrence, J., Kornelsen, J., Tomanek, B., and Sboto-Frankenstein, U. N. (2010). Human cervical spinal cord funiculi: investigation with magnetic resonance diffusion tensor imaging. *Journal of Magnetic Resonance Imaging: An Official Journal of the International Society for Magnetic Resonance in Medicine*, 31(4):829–837.

Oreja-Guevara, C., Rovaris, M., Iannucci, G., Valsasina, P., Caputo, D., Cavarretta, R., Sormani, M. P., Ferrante, P., Comi, G., and Filippi, M. (2005). Progressive gray matter damage in patients with relapsing-remitting multiple sclerosis: a longitudinal diffusion tensor magnetic resonance imaging study. *Archives of Neurology*, 62(4):578–584.

Organization, W. H. et al. (2008). Atlas: multiple sclerosis resources in the world 2008.

Ourselin, S., Roche, A., Prima, S., and Ayache, N. (2000). Block matching: A general framework to improve robustness of rigid registration of medical images. In *International Conference on Medical Image Computing And Computer-Assisted Intervention*, pages 557–566. Springer.

Purcell, E., Torrey, H., and Pound, R. (1946). Resonance absorption by nuclear magnetic moments in a solid. *Physical Review*, 69:37–38.

Reber, P. J., Wong, E. C., Buxton, R. B., and Frank, L. R. (1998). Correction of off resonance-related distortion in echo-planar imaging using epi-based field maps. *Magnetic Resonance in Medicine*, 39(2):328–330.

Ripley, B. (2002). Modern applied statistics with s.

Rovaris, M., Judica, E., Gallo, A., Benedetti, B., Sormani, M., Caputo, D., Ghezzi, A., Montanari, E., Bertolotto, A., Mancardi, G., et al. (2006). Grey matter damage predicts the evolution of primary progressive multiple sclerosis at 5 years. *Brain*, 129(10):2628–2634.

Ruthotto, L., Kugel, H., Olesch, J., Fischer, B., Modersitzki, J., Burger, M., and Wolters, C. (2012). Diffeomorphic susceptibility artifact correction of diffusion-weighted magnetic resonance images. *Physics in Medicine & Biology*, 57(18):5715.

Scherrer, B. and Warfield, S. K. (2012). Parametric representation of multiple white matter fascicles from cube and sphere diffusion mri. *PLoS one*, 7(11):e48232.

Schneider, T. and Wheeler-Kingshott, C. A. (2014). Q-space imaging: A model-free approach. In *Quantitative MRI of the Spinal Cord*, pages 146–155. Elsevier.

Snoussi, H., Caruyer, E., Cohen-Adad, J., Commowick, O., Combes, B., Bannier, E., Kerbrat, A., and Barillot, C. (2019). Geometric evaluation of distortion correction methods in diffusion mri of the spinal cord. In *IEEE International Symposium on Biomedical Imaging (ISBI)*.

Snoussi, H., Caruyer, E., Commowick, O., Bannier, E., and Barillot, C. (2017). Comparison of inhomogeneity distortion correction methods in diffusion mri of the spinal cord. In *ESMRMB-34th Annual Scientific Meeting*.

Song, S.-K., Yoshino, J., Le, T. Q., Lin, S.-J., Sun, S.-W., Cross, A. H., and Armstrong, R. C. (2005). Demyelination increases radial diffusivity in corpus callosum of mouse brain. *Neuroimage*, 26(1):132–140.

Speck, O., Stadler, J., and Zaitsev, M. (2008). High resolution single-shot epi at 7t. *Magnetic Resonance Materials in Physics, Biology and Medicine*, 21(1-2):73.

Stehling, M. K., Turner, R., and Mansfield, P. (1991). Echo-planar imaging: magnetic resonance imaging in a fraction of a second. *Science*, 254(5028):43–50.

Stejskal, E. O. and Tanner, J. E. (1965). Spin diffusion measurements: spin echoes in the presence of a time-dependent field gradient. *The journal of chemical physics*, 42(1):288–292.

Stroman, P. W., Wheeler-Kingshott, C., Bacon, M., Schwab, J., Bosma, R., Brooks, J., Cadotte, D., Carlstedt, T., Ciccarelli, O., Cohen-Adad, J., et al. (2014). The current state-of-the-art of spinal cord imaging: methods. *Neuroimage*, 84:1070–1081.

Tang, H., Zhang, D., Guo, S., and Qu, H. (2018). A novel model to simulate flexural complements in compliant sensor systems. *Sensors*, 18(4):1029.

Taso, M., Le Troter, A., Sdika, M., Ranjeva, J.-P., Guye, M., Bernard, M., and Callot, V. (2014). Construction of an in vivo human spinal cord atlas based on high-resolution mr images at cervical and thoracic levels: preliminary results. *Magnetic Resonance Materials in Physics, Biology and Medicine*, 27(3):257–267.

Tharwat, A. (2018). Classification assessment methods. *Applied Computing and Informatics*.

Théaudin, M., Saliou, G., Ducot, B., Deiva, K., Denier, C., Adams, D., and Ducreux, D. (2012). Short-term evolution of spinal cord damage in multiple sclerosis: a diffusion tensor mri study. *Neuroradiology*, 54(10):1171–1178.

Thorpe, J., Kidd, D., Moseley, I., Thompson, A., MacManus, D., Compston, D., McDonald, W., and Miller, D. (1996). Spinal mri in patients with suspected multiple sclerosis and negative brain mri. *Brain*, 119(3):709–714.

Tuch, D. S., Reese, T. G., Wiegell, M. R., Makris, N., Belliveau, J. W., and Wedeen, V. J. (2002). High angular resolution diffusion imaging reveals intravoxel white matter fiber heterogeneity. *Magnetic Resonance in Medicine*, 48(4):577–582.

Tuch, D. S., Reese, T. G., Wiegell, M. R., and Wedeen, V. J. (2003). Diffusion mri of complex neural architecture. *Neuron*, 40(5):885–895.

Valsasina, P., Rocca, M. A., Agosta, F., Benedetti, B., Horsfield, M. A., Gallo, A., Rovaris, M., Comi, G., and Filippi, M. (2005). Mean diffusivity and fractional anisotropy histogram analysis of the cervical cord in ms patients. *Neuroimage*, 26(3):822–828.

Van Hecke, W., Leemans, A., Sijbers, J., Vandervliet, E., Van Goethem, J., and Parizel, P. M. (2008). A tracking-based diffusion tensor imaging segmentation method for the detection of diffusion-related changes of the cervical spinal cord with aging. *Journal of Magnetic Resonance Imaging: An Official Journal of the International Society for Magnetic Resonance in Medicine*, 27(5):978–991.

von Meyenburg, J., Wilm, B. J., Weck, A., Petersen, J., Gallus, E., Mathys, J., Schaetzle, E., Schubert, M., Boesiger, P., von Meyenburg, K., et al. (2013). Spinal cord diffusion-tensor imaging and motor-evoked potentials in multiple sclerosis patients: microstructural and functional asymmetry. *Radiology*, 267(3):869–879.

Vos, T., Allen, C., Arora, M., Barber, R. M., Bhutta, Z. A., Brown, A., Carter, A., Casey, D. C., Charlson, F. J., Chen, A. Z., et al. (2016). Global, regional, and national incidence, prevalence, and years lived with disability for 310 diseases and injuries, 1990–2015: a systematic analysis for the global burden of disease study 2015. *The Lancet*, 388(10053):1545–1602.

Voss, H. U., Watts, R., Uluğ, A. M., and Ballon, D. (2006). Fiber tracking in the cervical spine and inferior brain regions with reversed gradient diffusion tensor imaging. *Magnetic resonance imaging*, 24(3):231–239.

Wang, Y., Wang, Q., Haldar, J. P., Yeh, F.-C., Xie, M., Sun, P., Tu, T.-W., Trinkaus, K., Klein, R. S., Cross, A. H., et al. (2011). Quantification of increased cellularity during inflammatory demyelination. *Brain*, 134(12):3590–3601.

Westin, C.-F., Maier, S. E., Mamata, H., Nabavi, A., Jolesz, F. A., and Kikinis, R. (2002). Processing and visualization for diffusion tensor mri. *Medical image analysis*, 6(2):93–108.

Wheeler-Kingshott, C., Stroman, P. W., Schwab, J., Bacon, M., Bosma, R., Brooks, J., Cadotte, D., Carlstedt, T., Ciccarelli, O., Cohen-Adad, J., et al. (2014). The current state-of-the-art of spinal cord imaging: applications. *Neuroimage*, 84:1082–1093.

Wheeler-Kingshott, C. A. and Cercignani, M. (2009). About "axial" and "radial" diffusivities. *Magnetic Resonance in Medicine*, 61(5):1255–1260.

Wheeler-Kingshott, C. A., Hickman, S. J., Parker, G. J., Ciccarelli, O., Symms, M. R., Miller, D. H., and Barker, G. J. (2002). Investigating cervical spinal cord structure using axial diffusion tensor imaging. *Neuroimage*, 16(1):93–102.

Xu, J., Shimony, J. S., Klawiter, E. C., Snyder, A. Z., Trinkaus, K., Naismith, R. T., Benzinger, T. L., Cross, A. H., and Song, S. (2013). Improved in vivo diffusion tensor imaging of human cervical spinal cord. *Neuroimage*, 67:64–76.

Zaitsev, M., Hennig, J., and Speck, O. (2004). Point spread function mapping with parallel imaging techniques and high acceleration factors: fast, robust, and flexible method for echo-planar imaging distortion correction. *Magnetic Resonance in Medicine: An Official Journal of the International Society for Magnetic Resonance in Medicine*, 52(5):1156–1166.

Zhang, J., Aggarwal, M., and Mori, S. (2012). Structural insights into the rodent cns via diffusion tensor imaging. *Trends in neurosciences*, 35(7):412–421.

Curriculum vitae

Haykel Snoussi was born in Tunisia in 1990. He got his baccalaureate degree from Abou El-Kacem Chebbi school in Sfax in 2009, his engineering degree from École nationale d'ingénieurs de Sfax and École Centrale de Nantes in 2014 and his master degree from Pierre and Marie Curie University in co-habilitation with Télécom ParisTech in 2015. Since November 2015, he joined Inria Rennes - Bretagne Atlantique research center as a PhD student, collaborating with Empenn (ex. VisAGeS) research Unit. This manuscript describes several research works done during this PhD thesis.

Titre : **Population imaging and diffusion MRI for characterizing multiple sclerosis in the human spinal cord**

Mots clés : IRM de diffusion, moelle épinière, sclérose en plaques

Résumé : L'IRM quantitative a un potentiel énorme pour fournir une valeur intrinsèque et indirecte aux propriétés des tissus utiles au diagnostic, au pronostic et aux essais cliniques de la sclérose en plaques (SEP), qui est une maladie inflammatoire du système nerveux central. Complémentaire à l'imagerie cérébrale, étudier l'impact de la maladie sur la moelle épinière grâce à l'imagerie quantitative, en particulier l'IRM de diffusion, devient un véritable défi. L'acquisition et le traitement de ce type de données posent des problèmes inhérents en raison de la distorsion de susceptibilité, de la petite section transversale de la moelle et l'absence de repères anatomiques visibles qui permettant d'identifier des voies ou du niveau vertébral. Dans ce contexte, nous proposons plusieurs contributions pour le traitement et l'analyse statistique de ces données.

Tout d'abord, nous proposons de nouvelles métriques géométriques pour évaluer et comparer différentes méthodes de correction de distorsion en mesurant l'alignement du modèle de diffusion reconstruit avec l'axe central apparent de la moelle épinière. Deuxièmement, en utilisant une cohorte de patients atteints de SEP et de témoins sains, nous étudions le lien entre les mesures de diffusion et la présence ou l'absence de lésion dans un niveau vertébral donné et nous montrons que nous pouvons prédire ce dernier avec une bonne précision en utilisant un apprentissage linéaire multivarié. Enfin, nous montrons la faisabilité d'une étude longitudinale de l'évolution des métriques d'IRM de diffusion en réalisant une étude de reproductibilité à l'aide d'un ensemble de données test-retest, et l'appliquons aux 2 premières acquisitions (M0 et M12) de notre cohorte de patients.

Title : **Population imaging and diffusion MRI for characterizing multiple sclerosis in the human spinal cord**

Keywords : Diffusion MRI, Spinal Cord, Multiple sclerosis

Abstract : Quantitative MRI has huge potential to provide intrinsic and normative value to tissue properties useful for diagnosis, prognosis and ultimately clinical trials in multiple sclerosis (MS) which is an inflammatory disorder of the central nervous system. Complementary to brain imaging, investigating how the spinal cord is damaged using quantitative imaging, and in particular diffusion MRI, becomes an acute challenge. Acquiring and processing this type of data present inherent challenges due to the susceptibility distortion, the small cross-sectional area of the spine and the lack of visible anatomical landmarks to help identification of tracts or vertebral level. In this context, we propose several contributions for the processing and statistical analysis of this data.

First, we propose novel geometric metrics to evaluate and compare different distortion correction methods by measuring the alignment of the reconstructed diffusion model with the apparent centerline of the spine. Second, using a cohort of MS patients and healthy controls, we study the link between diffusion measures and the presence or absence of lesion in a given vertebral level and we show that we can predict the latter with good accuracy by learning a multivariate linear classifier. Last, we show the feasibility of longitudinal study of the evolution of diffusion MRI metrics by performing a reproducibility study using a test-retest dataset and apply it to the 2 first timepoints (M0 and M12) of our cohort of MS patients.